AN ABSTRACT OF THE DISSERTATION OF

Adam Q. Lam for the degree of Doctor of Philosophy in Nuclear Engineering presented on November 22, 2021.

Title: Diffusion Accelerated Implicit Monte Carlo via Nonlinear Elimination for Thermal Radiative Transfer

Abstract approved: _____

Todd S. Palmer

In this dissertation, we derive and implement a new transport-diffusion hybrid algorithm for solving thermal radiative transfer (TRT) problems. Using the method of nonlinear elimination (NLEM), the TRT system of equations can be written in terms of a transport equation with the absence of scattering and a diffusion equation. The transport solution is obtained using a Monte Carlo (MC) method with implicit capture and the diffusion solution is used to accelerate the transport convergence. We name this method Diffusion Accelerated Implicit Monte Carlo (DAIMC).

A series of tests are used to verify the proposed algorithm and its associated solvers. After the verification of DAIMC, we investigate its performance by comparing DAIMC results to those obtained from the traditional Implicit Monte Carlo (IMC) method. In 1D slab geometry calculations, we show that DAIMC yields a

more accurate solution than IMC when compared to the analytic solution. The increased accuracy of the DAIMC solution comes at the cost of an increased computational time when compared to IMC. We have also employed Quasi-Monte Carlo (QMC) in the DAIMC algorithm for 1D calculations. QMC retains the same accuracy as the MC implementation of DAIMC while decreasing the required computing time.

We also implemented DAIMC in 2D-XY geometry using a piecewise constant representation of temperatures for the Monte Carlo transport solver and a linear-continuous discretization for the diffusion equation. For problems in which the opacity is constant or has a T^{-1} temperature dependence, the implementation choice for DAIMC converges to the correct equilibrium solution and provides more accurate results than the IMC method. We observed that small time steps are required for DAIMC to produce the analytic equilibrium solution when the opacity has a temperature dependence of T^{-2}.

DAIMC results for a crooked pipe problem are compared with results obtained from the IMC method. We observed nonphysical overheating at the interface of the thick and thin material region for both our DAIMC method and the IMC method. The nonphysical overheating of the interface improves with refinement of the mesh for both methods.

Diffusion Accelerated Implicit Monte Carlo via Nonlinear Elimination for Thermal Radiative Transfer

by

Adam Q. Lam

A DISSERTATION

submitted to

Oregon State University

in partial fulfillment of
the requirements for the
degree of

Doctor of Philosophy

Presented November 22, 2021
Commencement June 2022

Doctor of Philosophy dissertation of Adam Q. Lam presented on November 22, 2021.

APPROVED:

Major Professor, representing Nuclear Engineering

Head of the School of Nuclear Science and Engineering

Dean of the Graduate School

I understand that my dissertation will become part of the permanent collection of Oregon State University libraries. My signature below authorizes release of my dissertation to any reader upon request.

Adam Q. Lam, Author

ACKNOWLEDGEMENTS

I would first like to express my gratitude to Dr. Todd Palmer. Thank you for opening the doors and imparting your knowledge and wisdom to me over the course of my graduate school career. Your guidance and patience made this all possible. There is a saying,"Once my teacher, always my teacher" and I find it to be particularly true in this case.

I would also like to thank my mentors at LLNL for their continual help and support. Tom Brunner, thank you for your guidance and advice when I needed it. Rick Vega, thank you for imparting your computer knowledge and taking the time to help whenever I have questions. Nick Gentile, thank you for your discussions on Monte Carlo methods which proved to be invaluable.

I thank the group of friends I have made throughout the course of graduate school and particularly the Reactor Physics and Radiation Transport group. Nick Whitman and Aaron Reynolds, I look forward to our continual friendship and professional development together.

Lastly, I would like to thank my family. Grandmother and Grandfather, this one's for you. Mom and Dad, thank you for leaving everything you knew in moving to a new country and providing me with this opportunity. Lauren, my wife, thank you for being there every step of the way. Without any of you, this would never have been possible.

TABLE OF CONTENTS

TABLE OF CONTENTS (Continued)

LIST OF FIGURES

LIST OF FIGURES (Continued)

LIST OF FIGURES (Continued)

LIST OF FIGURES (Continued)

LIST OF FIGURES (Continued)

LIST OF TABLES

LIST OF APPENDIX FIGURES

LIST OF APPENDIX FIGURES (Continued)

Figure Page

Chapter 1: Introduction

Conduction, convection, and radiation are the three known mechanisms for heat transfer. Radiation heat transfer, or thermal radiative transfer (TRT), describes the process in which matter exchanges energy with its environment by emitting or absorbing radiation via photons. That is, all objects (matter) above absolute zero (0 K) emit thermal photons. Thermal photons are photons whose frequencies fall within a specific range of the electromagnetic spectrum [1], [2].

The TRT process is known to be the dominant mode of heat transfer in relatively-high to high-temperature (thousands to millions of degrees) physics regimes. The thermal energy emitted by matter is proportional to the matter's temperature raised to the fourth power [1]. This is often thought of as a material cooling off by emitting energy in the form of photons. These emitted photons then contribute to the overall energy of the radiation field. Photons from the radiation field can conversely be absorbed by the matter. When a material absorbs as much energy as it emits, the system is in equilibrium.

TRT is an important process in many engineering and astrophysics applications, particularly in high-energy density physics regimes. In the climate science community, TRT is used to model atmospheric heating and cooling [3]. Thermonuclear fusion is one of the many examples where TRT is a dominant process, such as those which take place in star formations or laboratory-controlled inertial

confinement fusion (ICF) [2].

Regardless of the application, it remains that solutions to the TRT equations are of particular interest. The TRT process is modeled by sets of nonlinear, coupled integro-differential equations. The complexity of the TRT equations often require numerical approximations to obtain solutions, as analytical solutions apply to only a small number of isolated cases. Methods for obtaining the numerical solutions to the TRT equations can be categorized into the following: deterministic, Monte Carlo, or hybrid (a combination of both deterministic and Monte Carlo).

Monte Carlo (MC) methods simulate a photon's life history by sampling pseudo-random numbers from the probability distribution functions which govern the interactions of the photon. Quantities of interest are then tallied based on these histories. The accuracy of the tallied quantities increases as more histories are simulated. The exact solution to the system can, in theory, be obtained if an infinite number of histories are used. Since photon histories are independent of one another, these can be computed in parallel (i.e., simulating multiple photons at once) [4]. The Implicit Monte Carlo method (IMC) is commonly used as the standard for solving the TRT equations [5], [6]. A major advantage of using the IMC method is due it being massively parallelizable. Many particles can be simultaneously simulated to yield accurate results. However, due to the effective-scattering term in the IMC equations, particles may experience a prohibitively large number of scattering events. While accurate results may be generated using IMC, this comes with the trade-off of being computationally expensive, as effective-scattering prolongs a particle's history [5], [7], [8].

Deterministic methods seek solutions by directly solving the TRT equations. To be more precise, these methods solve the approximate forms of the TRT equations. In the discrete ordinates (S_N) method, the angular variable is approximated with quadrature sets to describe the direction of travel by photons [9]. The S_N method reduces the angular variable to a finite set of directions. This reduction leads to systems that are easy and efficient to solve. A well-known numerical artifact of the S_N approximation is the so-called ray effects [10], [11]. Ray effects are due to the angular variable being reduced from an infinite set to a discrete set.

Another deterministic method is known as the diffusion approximation [12]–[16]. In the diffusion approximation, the angular variable is removed by an integration over all angles. This leads to a system of equations that is easy and efficient to compute numerically. Though the system of equations is easy to solve, the solutions may be inaccurate [7], [12], [15]. These inaccuracies are most prominent in optically thin regions and instances when there are large gradients in the radiation energy density [7].

Along with these approximations to the angular variable, the multigroup method can be used to approximate the energy dependency with a discrete number of energy groups [7], [17]. When only one group is used, this is often referred to as a 'gray problem' within the TRT community. The multigroup method can be used in conjunction with the discrete ordinates S_N method, the diffusion approximation, and the IMC method. These are only three examples of the several deterministic methods used in the TRT community.

We attempt to overcome the expensive cost of effective-scattering and the de-

ficiencies of the deterministic methods with a novel, hybrid transport-diffusion method for solving the TRT equations. The objectives for this research can be summarized as follows:

1. Derive and implement the NLEM method to the solution of the 1D (slab geometry) TRT equations in conjunction with Monte Carlo particle transport as the high-order solve, and diffusion as the low-order solver. Then, compare the computational accuracy and performance of this new method with the standard IMC method.

2. Derive and implement the NLEM approach to the solution of the 2D (XY geometry) TRT equations in conjunction with Monte Carlo particle transport as the high-order solve, and diffusion as the low-order solver. Then, compare the computational accuracy and performance with the standard IMC method.

3. Assess the effects of statistical noise on the accuracy and efficiency of the Monte Carlo/diffusion algorithm with the implementation of Quasi-Monte Carlo.

1.1 Dissertation Overview

The remainder of this dissertation is organized in the following manner:

II. Chapter 2 begins by formally introducing the mathematical description of TRT equations. This chapter then provides a literature review on the different

methods used in solving the TRT equations.

III. In Chapter 3, the mathematical framework for a novel hybrid Monte Carlo transport-diffusion method is presented. We name this method Diffusion Accelerated Implicit Monte Carlo (DAIMC).

IV. Chapter 4 provides numerical results using DAIMC and provides comparisons with the Implicit Monte Carlo method and a Quasi-Monte Carlo implementation of DAIMC.

V. Chapter 5 provides a discussion of the results from Chapter 4.

VI. Finally, Chapter 6 concludes this work and highlights future work.

Chapter 2: Thermal Radiative Transfer

2.1 Introduction

The physical process that describes how radiation interacts with matter is known as thermal radiative transfer (TRT). The radiation can be viewed as packets of quantized light which can be treated as particles, called photons. As photons traverse, they can interact with the material via scattering and/or absorption. As photons are absorbed by the material, the internal energy of the material increases. As the internal energy of the material increases so does the temperature of the material, since temperature is a measure of internal energy. The heated material cools off by emitting photons in accordance with Planck's frequency spectrum [1], [2], [18]–[20] .

The quantity of interest is the specific intensity $\mathcal{I}$ and can be defined as

$$\mathcal{I}(\mathbf{r}, \mathbf{\Omega}, \nu, t) = c\, h\, \nu\, n(\mathbf{r}, \mathbf{\Omega}, \nu, t), \tag{2.1}$$

where

Symbol	**Description**
$\mathcal{I}$ [GJ/ns-cm^2-keV-sr]	specific intensity,
$n(\mathbf{r}, \mathbf{\Omega}, \nu, t)$ [photons/cm^3-sr-Hz]	mean number of photons per differential volume,
c [cm/sh]	speed of light in vacuum,
$\mathbf{r}$ [cm]	position vector $(\mathbf{x}, \mathbf{y}, \mathbf{x})$,
$\mathbf{\Omega}$ [sr]	unit angle vector,
t [sh]	time,
h [keV/Hz]	Planck's constant,
ν [Hz]	photon frequency.

With the specific intensity defined, we introduce the conservation equation for photons. For systems without the presence of scattering or external sources of radiation, the TRT equations are written as

$$\frac{1}{c}\frac{\partial \mathcal{I}(\mathbf{r}, \mathbf{\Omega}, \nu, t)}{\partial t} + \mathbf{\Omega} \cdot \nabla \mathcal{I}(\mathbf{r}, \mathbf{\Omega}, \nu, t) + \sigma(\mathbf{r}, \nu, T)\mathcal{I}(\mathbf{r}, \mathbf{\Omega}, \nu, t) = \sigma(\mathbf{r}, \nu, T)B(\nu, T). \tag{2.2}$$

and

$$\rho(\mathbf{r})c_v(\mathbf{r})\frac{\partial T(\mathbf{r}, t)}{\partial t} = \int_0^\infty \int_{4\pi} \sigma(\mathbf{r}, \nu, T)\left[\mathcal{I}(\mathbf{r}, \mathbf{\Omega}, \nu, t) - B(\nu, T)\right] \mathrm{d}\mathbf{\Omega}' \, \mathrm{d}\nu', \tag{2.3}$$

where

Symbol	**Description**
σ [cm^{-1}]	material opacity,
T [keV]	material temperature,
$B(\nu, T)$	Planck's function for radiation,
ρ [g/cm^3]	material mass density,
c_v [GJ/keV-cm^3]	heat capacity of the material.

The assumption of local thermodynamic equilibrium (LTE) was used in writing Eq. (2.2) and Eq. (2.3). LTE states that the energy of the material can be well-defined by its temperature and follows Planck's function relating the temperature to the frequency [8], [19].

The quantities of interest are then $\mathcal{I}$ and T, which are the unknowns we seek in Eq. (2.2) and Eq. (2.3). Temperature T is given in units of kilo-electron-volts [keV] in the description as opposed to the familiar units of kelvins [K]. The simple conversion from [K] to [keV] can be expressed as

$$T \text{ [keV]} = k_B T \text{ [K]}, \tag{2.4}$$

where $k_B = 8.617343 \cdot 10^{-8}$ [keV/K] is known as the Boltzmann constant.

The nonlinear coupling of Eq. (2.2) and Eq. (2.3) arises from the black-body Planckian term,

$$B(\nu, T) = \frac{2h\nu^3}{c^2} \frac{1}{e^{(\frac{h\nu}{T})} - 1}, \tag{2.5}$$

which appears in both equations. A source of difficulty in solving the TRT equations arises from this strongly nonlinear Planckian term, which tightly couples

both equations.

2.2 The Implicit Monte Carlo (IMC) Method

Fleck and Cummings developed an 'implicit' approximation to Eq. (2.2) and Eq. (2.3) in which a Monte Carlo method can be applied, referred to as Implicit Monte Carlo (IMC) [6]. The IMC method introduces three approximations to Eq. (2.2) and Eq. (2.3):

1. Temperature-dependent data are evaluated using the beginning of the time step temperature.

2. A parameter α is introduced, which serves to approximate $\bar{U}_r$ by taking a linear combination of its value at the beginning and end of the time step.

3. Time-averaged quantities are substituted with their time-continuous values.

The IMC method begins by rewriting Eq. (2.3) in terms of the material energy density

$$\frac{\partial U_m}{\partial t} = \int_0^\infty \int_{4\pi} \sigma \left(\mathcal{I} - B\right) \mathrm{d}\mathbf{\Omega}' \, \mathrm{d}\nu', \tag{2.6}$$

and defining the equilibrium radiation energy density as

$$U_r = aT^4, \tag{2.7}$$

where

$$a = 0.01372 \left[\frac{\mathrm{GJ}}{\mathrm{cm}^3\mathrm{keV}^4}\right] = \text{ radiation constant}, \tag{2.8}$$

and

$$\frac{\partial U_m}{\partial T} = c_v. \tag{2.9}$$

The relationship between the material energy density and the equilibrium radiation energy density can then be defined as

$$\beta = \frac{\partial U_r}{\partial U_m} = \frac{4aT^3}{c_v}. \tag{2.10}$$

Planck's radiation function is given as

$$B(\nu, T) = \frac{2h\nu^3}{c^2} \frac{1}{e^{(\frac{h\nu}{T})} - 1}, \tag{2.11}$$

where

$$h = 4.135667516 \times 10^{-9}\,[\text{keV-ns}] = \text{Planck's constant}, \tag{2.12}$$

and the frequency-normalized Planckian is defined as

$$b \equiv \frac{B}{\int_0^\infty B \, \mathrm{d}\nu}, \tag{2.13}$$

where the frequency integrated Planckian is given as

$$\int_0^\infty B \, \mathrm{d}\nu = \frac{caT^4}{4\pi}. \tag{2.14}$$

The Planck opacity can then written as

$$\sigma_p \equiv \int_0^\infty \sigma \; b \; \mathrm{d}\nu. \tag{2.15}$$

Next, define the time-average operator to be

$$\bar{(\cdot)} \equiv \frac{1}{\Delta t} \int_{t_n}^{t_{n+1}} (\cdot) \mathrm{d}t. \tag{2.16}$$

Using the definitions above, Eq. (2.2) and Eq. (2.3) may now be written as

$$\frac{1}{c}\frac{\partial \mathcal{I}}{\partial t} + \mathbf{\Omega} \cdot \nabla \mathcal{I} + \sigma \mathcal{I} = \sigma b \frac{cU_r}{4\pi} \tag{2.17}$$

$$\frac{\partial U_m}{\partial t} + \sigma_p c U_r = \int_0^\infty \int_{4\pi} \sigma \mathcal{I} \mathrm{d}\mathbf{\Omega}' \; \mathrm{d}\nu'. \tag{2.18}$$

Applying approximation (1) to Eq. (2.17) and Eq. (2.18) yields

$$\frac{1}{c}\frac{\partial \mathcal{I}}{\partial t} + \mathbf{\Omega} \cdot \nabla \mathcal{I} + \sigma_n \mathcal{I} = \sigma_n b_n \frac{cU_r}{4\pi} \tag{2.19}$$

$$\frac{\partial U_m}{\partial t} + \sigma_{p,n} c U_r = \int_0^\infty \int_{4\pi} \sigma_n \mathcal{I} \mathrm{d}\mathbf{\Omega}' \; \mathrm{d}\nu'. \tag{2.20}$$

It is useful to write Eq. (2.20) as

$$\frac{1}{\beta_n}\frac{\partial U_r}{\partial t} + \sigma_{p,n} c U_r = \int_0^\infty \int_{4\pi} \sigma_n \mathcal{I} \mathrm{d}\mathbf{\Omega}' \; \mathrm{d}\nu', \tag{2.21}$$

in order to apply the second approximation. Using the time-average operator, and discretizing in time, Eq. (2.21) becomes

$$\frac{1}{\beta_n}\frac{U_r^{n+1}-U_r^n}{\Delta t}+\sigma_{p,n}c\bar{U_r}=\int_0^\infty\int_{4\pi}\sigma_n\bar{\mathcal{I}}\mathrm{d}\mathbf{\Omega}'\,\mathrm{d}\nu', \tag{2.22}$$

with

$$\bar{U_r}\approx(1-\alpha)U_r^n+\alpha U_r^{n+1}. \tag{2.23}$$

Substituting Eq. (2.23) back into Eq. (2.22) yields

$$\bar{U_r}=f_nU_r^n+\frac{(1-f_n)}{c\sigma_{p,n}}\int_0^\infty\int_{4\pi}\sigma_n\bar{\mathcal{I}}\mathrm{d}\mathbf{\Omega}'\,\mathrm{d}\nu'. \tag{2.24}$$

The third and final approximation replaces the time-averaged quantities in Eq. (2.24) with their continuous values to get

$$U_r(t)\approx f_nU_r^n+\frac{(1-f_n)}{c\sigma_{p,n}}\int_0^\infty\int_{4\pi}\sigma_n\mathcal{I}(t)\mathrm{d}\mathbf{\Omega}'\,\mathrm{d}\nu' \tag{2.25}$$

where

$$f_n=\frac{1}{1+\alpha\beta_n\sigma_{p,n}c\Delta t} \tag{2.26}$$

is known as the Fleck factor. The term α can be thought of as a control on the implicitness of the approximation. The most common, and most implicit, value is $\alpha=1.0$.

These three approximations, applied to Eq. (2.2) and Eq. (2.3), produce

$$\frac{1}{c}\frac{\partial \mathcal{I}}{\partial t} + \mathbf{\Omega}\cdot\nabla\mathcal{I} + \sigma_n\mathcal{I} = \frac{\sigma_n b_n}{\sigma_{p,n}}\frac{1}{4\pi}\int_0^\infty\int_{4\pi}(1-f_n)\sigma_n\mathcal{I}\mathrm{d}\mathbf{\Omega}'\,\mathrm{d}\nu' + f_n\sigma_{p,n}\frac{\sigma_n b_n}{\sigma_{p,n}}\frac{cU_r^n}{4\pi}, \quad (2.27)$$

and

$$\frac{\partial U_m}{\partial t} + f_n\sigma_{p,n}cU_r^n = \int_0^\infty\int_{4\pi} f_n\sigma_n\mathcal{I}\mathrm{d}\mathbf{\Omega}'\,\mathrm{d}\nu', \quad (2.28)$$

which are known as the IMC equations. Temperature at the next time step can then be computed using

$$\int_{T^n}^{T^{n+1}} c_v\mathrm{d}T' = U_m^{n+1} - U_m^n. \quad (2.29)$$

Symbol	**Description**
σ_n [cm^{-1}]	material opacity,
$\sigma_{p,n}$ [cm^{-1}]	Planck opacity,
b_n	frequency normalized Planck spectrum,
U_m	material energy density,
U_r^n	equilibrium radiation energy density,
f_n	Fleck factor.

For a detailed description of a Monte Carlo implementation using Eq.(2.27) and Eq. (2.28), the reader can refer to [5]. While the IMC method provides a widely adopted Monte Carlo interpretation to the TRT equations, there are still several

deficiencies to the method. Approximation 2 introduces a variable $\alpha \in [0, 1]$ which directly controls the implicitness of the IMC method. As previously mentioned, $\alpha = 1$ is the most commonly used, as well as the most implicit choice for α. Still, temporal oscillations may occur even with the most implicit choice of α. For example, temporal oscillations may appear when large time steps are chosen for a given transient problem. The lower limit of this 'large' time step is difficult to determine *a priori*. [5]

Notice the first term on the right hand side of Eq. (2.27) appears to be an isotropic scattering term. Recall, the derivations began with Eq. (2.2) having no isotropic scattering. The IMC approximations introduce an effective scattering term to the radiation transport equation. This effective scattering term simulates the absorption-reemission process through a scattering event. When the Fleck factor is small (i.e., $f << 1.0$) or the material is optically thick, effective-scattering events will be the dominant mode of interaction for photons. This requires longer particle histories and, consequently, increased computation time.

Several methods have been developed to improve the computational efficiency of effective scattering. The first of these methods introduced a random walk treatment where effective scattering events are replaced by a single advancement of a photon in phase space [21]. Gentile also proposed a method called IMCD [22], [23] to decrease computational cost. IMCD utilizes the diffusion approximation in regions where IMC is prohibitively slow (i.e., optically thick regions) and reverts back to IMC in optically thinner regions. Another method which combines transport-diffusion is called Discrete Diffusion Monte Carlo (DDMC) [24].

As mentioned previously, IMC should be thought of as 'semi-implicit' rather than truly implicit [5], [25], [26]. Several different methods have been developed as a remedy to this semi-implicit behavior, which involves an iterative process. One such method is called Iterative Implicit Monte Carlo (IIMC), which is fully implicit, but comes with the trade-off of being computationally expensive in cold, opaque regions [27]. Another iterative method which attempts to be more implicit is the iterative thermal emission IMC (ITE IMC), which can take larger time steps than traditional IMC [28].

2.2.1 IMC as a Newton iteration

The 'semi-implicit' nature of Fleck and Cummings's IMC may lead to a direct violation of the maximum principle, causing overheating [26], [29], [30]. Vega and Brunner have shown that the IMC equations can be obtained by casting the TRT equations as a Newton iteration [30]. The reader may refer to Appendix A for an overview of a Newton iteration and the notations used in this section. The time-continuous form of the TRT equations used are

$$\frac{1}{\beta}\frac{\partial U_r}{\partial t} + \sigma_p c U_r = \int_0^\infty \int_{4\pi} \sigma \mathcal{I} \mathrm{d}\mathbf{\Omega}' \, \mathrm{d}\nu', \tag{2.30}$$

and

$$\frac{1}{c}\frac{\partial \mathcal{I}}{\partial t} + \mathbf{\Omega} \cdot \nabla \mathcal{I} + \sigma \mathcal{I} = \sigma \frac{c U_r}{4\pi}. \tag{2.31}$$

Now, discretize Eq. (2.30) and Eq. (2.31) implicitly in time and define the residuals as

$$m(U_r^{n+1}, \mathcal{I}^{n+1}) = \frac{1}{\beta \Delta t}(U_r^{n+1} - U_r^n) + \sigma_p c U_r^{n+1} - \int_0^\infty \int_{4\pi} \sigma \mathcal{I}^{n+1} \mathrm{d}\mathbf{\Omega}' \, \mathrm{d}\nu', \quad (2.32)$$

and

$$r(U_r^{n+1}, \mathcal{I}^{n+1}) = \frac{1}{c\Delta t}(\mathcal{I}^{n+1} - \mathcal{I}^n) + \mathbf{\Omega} \cdot \nabla \mathcal{I}^{n+1} + \sigma \mathcal{I}^{n+1} - \frac{c\sigma}{4\pi} U_r^{n+1}, \quad (2.33)$$

where $m(U_r^{n+1}, \mathcal{I}^{n+1})$ is the residual of the material energy equation and $r(U_r^{n+1}, \mathcal{I}^{n+1})$ is the residual of the radiation transport equation. The system of equations of interest has two equations and two unknowns. The two equations are the residual of the material energy equation and the residual of the radiation transport equation. The two unknowns are U_r^{n+1} and I^{n+1}. The Newton formulation can then be written as a 2x2 system, given as

$$\mathbf{f}(\mathbf{x}) = \begin{bmatrix} m(U_r^{n+1}, \mathcal{I}^{n+1}) \\ r(U_r^{n+1}, \mathcal{I}^{n+1}) \end{bmatrix} = \begin{bmatrix} 0 \\ 0 \end{bmatrix}. \quad (2.34)$$

The entries of the Jacobian are

$$J_{m,U_r} = \frac{1}{\beta \Delta t} + \sigma_p c = \mathbf{A}, \qquad J_{m,\mathcal{I}} = -\int \int_{4\pi} \sigma(\cdot) \mathrm{d}\Omega = \mathbf{B} \quad (2.35)$$

$$J_{r,U_r} = -\frac{c\sigma}{4\pi} = \mathbf{C}, \qquad J_{r,\mathcal{I}} = \frac{1}{c} + \mathbf{\Omega} \cdot \nabla(\cdot) + \sigma = \mathbf{D}. \quad (2.36)$$

For the system defined above, a Newton step then takes the form

$$\begin{bmatrix} \mathbf{A} & \mathbf{B} \\ \mathbf{C} & \mathbf{D} \end{bmatrix} \begin{bmatrix} \delta U_r \\ \delta \mathcal{I} \end{bmatrix} = - \begin{bmatrix} m(U_r^n, \mathcal{I}^n) \\ r(U_r^n, \mathcal{I}^n) \end{bmatrix}. \tag{2.37}$$

Using the Schur complement, $\delta\mathcal{I}$ can be obtained via

$$(\mathbf{D} - \mathbf{C}\mathbf{A}^{-1}\mathbf{B})\delta\mathcal{I} = -r(U_r^n, \mathcal{I}^n) + \mathbf{C}\mathbf{A}^{-1}\left(m(U_r^n, \mathcal{I}^n)\right). \tag{2.38}$$

Expand Eq. (2.38) with the definitions of **A,B,C** and **D** we find that the IMC radiation transport equation is obtained.

$$\begin{aligned} &\frac{1}{c}\frac{\partial \mathcal{I}}{\partial t} + \mathbf{\Omega}\cdot\nabla\mathcal{I} + \sigma_n\mathcal{I} \\ &\qquad = \frac{\sigma_n b_n}{\sigma_{p,n}}\frac{1}{4\pi}\int_0^\infty\int_{4\pi}(1-f_n)\sigma_n\mathcal{I}\mathrm{d}\mathbf{\Omega}'\,\mathrm{d}\nu' + f_n\sigma_{p,n}\frac{\sigma_n b_n}{\sigma_{p,n}}\frac{cU_r^n}{4\pi}, \end{aligned} \tag{2.39}$$

where

$$\mathbf{C}\mathbf{A}^{-1} = -\frac{1}{4\pi}(1-f_n). \tag{2.40}$$

It can be shown that the term $\mathbf{C}\mathbf{A}^{-1}\mathbf{B}$ is the effective scattering term of Eq. (2.27). This confirms that IMC is a single Newton step with the material residual and the radiation residual defined as Eq. (2.32) and Eq. (2.33), respectively.

2.2.2 Towards a More Implicit Monte Carlo

As previously mentioned, IMC can be viewed as a single Newton iteration, but more than one Newton step can be taken. The system in Eq. (2.37) can be modified to look like

$$\begin{bmatrix} \mathbf{A}^* & \mathbf{B}^* \\ \mathbf{C}^* & \mathbf{D}^* \end{bmatrix} \begin{bmatrix} \delta U_r \\ \delta \mathcal{I} \end{bmatrix} = - \begin{bmatrix} m(U_r^*, \mathcal{I}^*) \\ r(U_r^*, \mathcal{I}^*) \end{bmatrix}, \tag{2.41}$$

where

$$\delta U_r = U_r^{n+1} - U_r^*; \quad \delta \mathcal{I} = \mathcal{I}^{n+1} - \mathcal{I}^*.$$

The superscript $(\cdot)^*$ represents the most recent evaluation of the quantities. The system can then be rewritten as

$$(\mathbf{D}^* - \mathbf{C}^*(\mathbf{A}^*)^{-\mathbf{1}}\mathbf{B}^*)\delta\mathcal{I} = -r(U_r^*, \mathcal{I}^*) + \mathbf{C}^*\mathbf{A}^{*-1}\left(m(U_r^*, \mathcal{I}^*)\right). \tag{2.42}$$

Once expanded, Eq. (2.42) becomes

$$\begin{aligned} \frac{1}{c}\frac{\mathcal{I}^{n+1} - \mathcal{I}^n}{\Delta t} + \mathbf{\Omega}\cdot\nabla\mathcal{I}^{n+1} + \sigma^*\mathcal{I}^{n+1} & \\ = \frac{1}{4\pi}\int_{4\pi}(1-f^*)\sigma^*\mathcal{I}^{n+1}\mathrm{d}\mathbf{\Omega}' & \\ + \left(\frac{c\sigma^* f^*}{4\pi}U_r^* - \frac{1}{4\pi\beta^*\Delta t}(1-f^*)(U_r^* - U_r^n)\right). & \end{aligned} \tag{2.43}$$

When the initial guess is $U_r^* = U_r^n$, as it is when a single Newton step is taken, we recover the grey IMC radiation transport equation [30].

2.3 The Diffusion Approximation

The diffusion approximation is applied by first integrating Eq. (2.2) over all angles and energies, i.e.,

$$\int_{4\pi}\int_{0}^{\infty}(\cdot)\mathrm{d}\mathbf{\Omega}\mathrm{d}\nu, \tag{2.44}$$

to obtain

$$\frac{1}{c}\frac{\partial E}{\partial t}+\nabla\cdot\vec{F}+\sigma_a E=4\pi\sigma_a B(T_m)+Q_r, \tag{2.45}$$

with

$$E=\frac{1}{c}\int_{4\pi}\int_{0}^{\infty}\mathcal{I}\,\mathrm{d}\mathbf{\Omega}\,\mathrm{d}\nu \tag{2.46}$$

and

$$\mathbf{F}=\int_{4\pi}\int_{0}^{\infty}\mathbf{\Omega}\mathcal{I}\mathrm{d}\mathbf{\Omega}\,\mathrm{d}\nu. \tag{2.47}$$

Then, approximate

$$\mathbf{F}=-\frac{1}{3\sigma_t}\nabla E \tag{2.48}$$

to arrive at the thermal radiation diffusion equation [7], [12]

$$\frac{1}{c}\frac{\partial E}{\partial t}-\nabla\cdot\frac{1}{3\sigma_t}\nabla E+\sigma_t E=4\pi\sigma_t B(T_m)+Q_r, \tag{2.49}$$

coupled with the material energy density equation

$$\frac{\partial U_m}{\partial t} = \int_0^\infty c\sigma_a(E - 4\pi B(T_m))\mathrm{d}\nu + Q_m. \tag{2.50}$$

In the approximation required to arrive at the diffusion Eq. (2.49) from the transport Eq. (2.2), there has been a fundamental change in the behavior of the equation. The transport equation, Eq. (2.2) is classified as hyperbolic, which requires a finite propagation speed. The diffusion equation Eq. (2.49) is classified as parabolic, implying that a change in any particular region is immediately propagated through all other regions. This results in speeds that are faster than light, which is nonphysical, and a correction must be made. A flux-limiting method is usually applied to the diffusion equation in order to correct this deficiency [7], [19].

A variety of flux limiting methods exist, many of which can be cast in the form

$$\frac{1}{c}\frac{\partial E}{\partial t} - \nabla \cdot \frac{\chi}{\sigma_t}\nabla E = \sigma_a(4\pi B(T_m) - E) + Q_r, \tag{2.51}$$

where χ is the Eddington factor. Different flux-limiting schemes vary in the expressions for χ [7], [15], [16], [31]–[33], a common expression being the Levermore-Pomraning flux limiter, where the approximation is

$$\chi = \frac{1}{R}\left[\coth R - \frac{1}{R}\right] \tag{2.52}$$

with

$$R = \frac{\nabla E}{\sigma_t E}. \tag{2.53}$$

2.4 Nonlinear Elimination (NLEM) Applied to Radiation Diffusion

The diffusion approximation to Eq. (2.2) and Eq. (2.3) can written as

$$\rho\frac{\partial e}{\partial t} = -c\sigma_a B + c\sigma_a\phi + Q, \tag{2.54}$$

and

$$\frac{\partial \phi}{\partial t} = \nabla\cdot\frac{c}{3\sigma_t}\nabla\phi + c\sigma_a B - c\sigma_a\phi + S. \tag{2.55}$$

The material residuals and the radiation residuals of Eq. (2.54) and Eq. (2.55) are then defined as

$$m(e,\phi) = \rho\frac{(e-e^{n-1})}{\Delta t} + c\sigma_a B - c\sigma_a\phi - Q \tag{2.56}$$

and

$$r(e,\phi) = \frac{(\phi-\phi^{n-1})}{\Delta t} - \nabla\cdot\frac{c}{3\sigma_t}\nabla\phi - c\sigma_a B + c\sigma_a\phi - S. \tag{2.57}$$

Recall the definitions of the Jacobian matrix and apply them to Eq. (2.56) and Eq. (2.57) to obtain the following entries [34],

$$J_{e,e} = \frac{\rho}{\Delta t} + \frac{c}{c_v}\sigma_a\frac{\partial B}{\partial T} = \mathbf{A} \tag{2.58a}$$

$$J_{e,\phi} = -c\sigma_a = \mathbf{B} \tag{2.58b}$$

$$J_{\phi,e} = -\frac{c}{c_v}\sigma_a\frac{\partial B}{\partial T} = \mathbf{C} \tag{2.58c}$$

$$J_{\phi,\phi} = \frac{1}{\Delta t} - \nabla\cdot\frac{c}{3\sigma_t}\nabla + c\sigma_a = \mathbf{D}. \tag{2.58d}$$

The Schur complement for this system is then

$$(\mathbf{D} - \mathbf{CA^{-1}B})\delta\phi = -r(e^l, \phi^l) + \mathbf{CA}^{-1}(m(e^l, \phi^l)). \tag{2.59}$$

The nonlinear elimination method (NLEM) [34], [35] is applied by solving for an $\hat{e}(\phi)$ that is a solution to

$$r(\hat{e}(\phi), \phi) = 0, \tag{2.60}$$

which is also a solution of

$$m(\hat{e}, \phi) = 0 \tag{2.61}$$

while maintaining

$$r(\hat{e}(\phi), \phi) = f(e, \phi) = 0. \tag{2.62}$$

This method effectively removes the material residual equation from the Schur complement and reduces Eq. (2.59) to

$$(\mathbf{D} - \mathbf{CA^{-1}B})\delta\phi = -r(e^l, \phi^l). \tag{2.63}$$

Though the new system has effectively eliminated the material energy residual equation, it must still be solved via Eq. (2.56).

The expanded Eq. (2.63) has the form

$$\frac{1}{\Delta t}\phi^{l+1} - \nabla \cdot \frac{c}{3\sigma_t}\nabla\phi^{l+1} + c\sigma_a\phi^{l+1} + \mathbf{CA}^{-1}c\sigma_a\phi^{l+1} = \frac{1}{\Delta t}\phi^{n-1} + c\sigma_a B + S + \mathbf{CA}^{-1}c\sigma_a\phi^l. \tag{2.64}$$

The solution can be obtained by splitting Eq. (2.64) into two parts, namely

$$\frac{1}{\Delta t}\phi^{l+1,k+1/2} - \nabla \cdot \frac{c}{3\sigma_t}\nabla\phi^{l+1,k+1/2} + c\sigma_a\phi^{l+1,k+1/2} = \frac{1}{\Delta t}\phi^{n-1} + c\sigma_a B + S + \mathbf{C}\mathbf{A}^{-1}c\sigma_a(\phi^l - \phi^{l+1,k}), \quad (2.65)$$

and

$$(\mathbf{D} - \mathbf{C}\mathbf{A}^{-\mathbf{1}}\mathbf{B})\phi^\dagger = \mathbf{C}\mathbf{A}^{-\mathbf{1}}\mathbf{B}\left(\phi^{l+1,k+1/2} - \phi^{l+1,k}\right). \quad (2.66)$$

Once these two solutions are computed, the next iteration's estimate is then

$$\phi^{l+1,k+1} = \phi^{l+1,k+1/2} + \phi^\dagger. \quad (2.67)$$

For a detailed description, please refer to [34].

This nonlinear elimination method applied to radiation diffusion allows for larger time steps and improved accuracy for certain test problems. Though this method requires an extra iteration loop for the material energy residual equation, this additional loop does not increase the computational cost when compared to traditional methods [34]. We extend this work by applying NLEM to the full TRT rather than thermal radiation diffusion.

2.5 Summary

In this section, the equations which model the TRT process were introduced and discussed. Several different methods which are commonly used to solve the TRT

equations, or its approximate forms, were detailed. The IMC method, and several of its variations, were discussed. It was shown that the IMC method can be viewed as a single Newton step. The next chapter extends the method of nonlinear elimination to thermal radiation transport.

Chapter 3: Methodology

3.1 Introduction

In this chapter, a detailed description for Diffusion Accelerated Implicit Monte Carlo (DAIMC) is given. The derivation for DAIMC begins with the grey TRT equations. The TRT equations are then rewritten to take form of a Newton iteration. Nonlinear elimination is applied to the Newton system, which results in a transport equation similar to Eq. (2.64).

3.2 The Grey TRT Equations

Assuming no volumetric sources of heat or particles, and no scattering, the grey TRT equations are

$$\frac{\partial U_m}{\partial t} = \int_{4\pi} \sigma \left(\mathcal{I} - B\right) \mathrm{d}\mathbf{\Omega}, \tag{3.1}$$

and

$$\frac{1}{c}\frac{\partial \mathcal{I}}{\partial t} + \mathbf{\Omega} \cdot \nabla \mathcal{I} + \sigma \mathcal{I} = \sigma B. \tag{3.2}$$

Recall that under local thermodynamic equilibrium [36], the frequency integrated Planckian can be written as

$$B(T) = \int_0^\infty B(\nu, T)\, \mathrm{d}\nu = \frac{caT^4}{4\pi} = c\frac{U_r}{4\pi}. \tag{3.3}$$

Eq. (3.1) and Eq. (3.2) can be written in terms of the equilibrium radiation energy density, Eq. (2.7), and the frequency integrated Planckian as

$$\frac{\partial U_m}{\partial t} = \int_{4\pi} \sigma\mathcal{I}\mathrm{d}\mathbf{\Omega} - \sigma c U_r, \tag{3.4}$$

and

$$\frac{1}{c}\frac{\partial \mathcal{I}}{\partial t} + \mathbf{\Omega}\cdot\nabla\mathcal{I} + \sigma\mathcal{I} = \sigma c\frac{U_r}{4\pi}. \tag{3.5}$$

Next, define the residuals of Eq. (3.4) and Eq. (3.5) as the time-integrated functions given by

$$m(U_m, \mathcal{I}) = \int_{\Delta t} \frac{\partial U_m}{\partial t}\, \mathrm{d}t + \int_{\Delta t} \sigma c U_r\, \mathrm{d}t - \int_{\Delta t}\int_{4\pi} \sigma\mathcal{I}\mathrm{d}\mathbf{\Omega}'\, \mathrm{d}t, \tag{3.6}$$

and

$$r(U_m, \mathcal{I}) = \int_{\Delta t} \frac{1}{c}\frac{\partial \mathcal{I}}{\partial t}\, \mathrm{d}t + \int_{\Delta t} \mathbf{\Omega}\cdot\nabla\mathcal{I}\, \mathrm{d}t + \int_{\Delta t} \sigma\mathcal{I}\, \mathrm{d}t - \int_{\Delta t} \sigma c\frac{U_r}{4\pi}\, \mathrm{d}t. \tag{3.7}$$

The evaluation of these residuals can be written as

$$m(U_m, \mathcal{I}) = [U_m - U_m^n] + [\Delta t \sigma c U_r] - \left\{\int_{\Delta t}\int_{4\pi} \sigma\mathcal{I}\mathrm{d}\mathbf{\Omega}\, \mathrm{d}t\right\}, \tag{3.8}$$

and

$$r(U_m, \mathcal{I}) = \frac{1}{c}[\mathcal{I} - \mathcal{I}^n] + \left\{ \int_{\Delta t} \mathbf{\Omega} \cdot \nabla \mathcal{I} \, \mathrm{d}t + \int_{\Delta t} \sigma \mathcal{I} \, \mathrm{d}t \right\} - \left[\Delta t \sigma c \frac{U_r}{4\pi} \right], \tag{3.9}$$

where the terms in $\{\cdot\}$ represents the time-averaged quantities and the superscript n represents the beginning of time step quantities.

The Newton iteration for this system is written as

$$\begin{bmatrix} \mathbf{A} & \mathbf{B} \\ \mathbf{C} & \mathbf{D} \end{bmatrix} \begin{bmatrix} \delta^\ell_{U_m} \\ \delta^\ell_{\mathcal{I}} \end{bmatrix} = - \begin{bmatrix} m(U^\ell_m, \mathcal{I}^\ell) \\ r(U^\ell_m, \mathcal{I}^\ell) \end{bmatrix}, \tag{3.10}$$

with

$$\delta^\ell_{U_m} = U^{\ell+1}_m - U^\ell_m \quad \text{and} \quad \delta^\ell_{\mathcal{I}} = \mathcal{I}^{\ell+1} - \mathcal{I}^\ell, \tag{3.11}$$

where ℓ is the current Newton iteration's index. The entries of the Jacobian matrix are then

$$1 + \sigma c \beta \Delta t = \mathbf{A}, \tag{3.12a}$$

$$- \int_{\Delta t} \int_{4\pi} \sigma(\cdot) \mathrm{d}\mathbf{\Omega} \, \mathrm{d}t = \mathbf{B}, \tag{3.12b}$$

$$-(\frac{c\sigma\beta\Delta t}{4\pi}) = \mathbf{C}, \tag{3.12c}$$

$$\frac{1}{c} + \int_{\Delta t} \mathbf{\Omega} \cdot \nabla (\cdot) \, \mathrm{d}t + \int_{\Delta t} \sigma (\cdot) \, \mathrm{d}t = \mathbf{D}. \tag{3.12d}$$

The Schur complement for the system given as

$$(\mathbf{D}-\mathbf{C}\mathbf{A}^{-1}\mathbf{B})(\mathcal{I}^{\ell+1}-\mathcal{I}^{\ell})=-r(U_m^{\ell},\mathcal{I}^{\ell})+\mathbf{C}\mathbf{A}^{-1}(m(U_m^{\ell},\mathcal{I}^{\ell})). \tag{3.13}$$

NLEM is applied by solving the material residual equation

$$m(U_m^{\ell},\mathcal{I}^{\ell})=U_m^{\ell}-U_m^{n}+\Delta t\sigma cU_r^{\ell}-\left\{\int_{\Delta t}\int_{4\pi}\sigma\mathcal{I}^{\ell}\mathrm{d}\mathbf{\Omega}\ \mathrm{d}t\right\}=0. \tag{3.14}$$

This material residual will be discussed in subsequent sections. Once the material residual is eliminated from the system,

$$(\mathbf{D}-\mathbf{C}\mathbf{A}^{-1}\mathbf{B})(\mathcal{I}^{\ell+1}-\mathcal{I}^{\ell})=-r(U_m^{\ell},\mathcal{I}^{\ell}), \tag{3.15}$$

or

$$(\mathbf{D}-\mathbf{C}\mathbf{A}^{-1}\mathbf{B})\mathcal{I}^{\ell+1}=(\mathbf{D}-\mathbf{C}\mathbf{A}^{-1}\mathbf{B})\mathcal{I}^{\ell}-r(U_m^{\ell},\mathcal{I}^{\ell}). \tag{3.16}$$

As previously mentioned, the $\mathbf{C}\mathbf{A}^{-1}\mathbf{B}$ on the left hand side of Eq. (3.16) is responsible for effective scattering.

The effective scattering can be treated by first introducing an iteration index k to the solution, i.e.,

$$\mathcal{I}^{\ell+1}=\mathcal{I}^{\ell+1,k+1} \tag{3.17}$$

Then, split the solution into two components [34], [37], [38], namely

$$\mathcal{I}^{\ell+1}=\mathcal{I}^{\ell+1,k+1}=\mathcal{I}^{\ell+1,k+1/2}+\mathcal{I}^{\dagger}. \tag{3.18}$$

A substitution of Eq. (3.18) into Eq. (3.16) will yield

$$(\mathbf{D}-\mathbf{C}\mathbf{A}^{-1}\mathbf{B})(\mathcal{I}^{\ell+1,k+1/2}+\mathcal{I}^{\dagger})=(\mathbf{D}-\mathbf{C}\mathbf{A}^{-1}\mathbf{B})\mathcal{I}^{\ell}-r(U_m^{\ell},\mathcal{I}^{\ell}). \tag{3.19}$$

3.3 The Transport Solution

The solution to Eq. (3.19) requires the solution to

$$(\mathbf{D}-\mathbf{C}\mathbf{A}^{-1}\mathbf{B})\mathcal{I}^{\ell+1,k+1/2}, \tag{3.20}$$

or, by distributing the operators,

$$(\mathbf{D})\mathcal{I}^{\ell+1,k+1/2}-(\mathbf{C}\mathbf{A}^{-1}\mathbf{B})\mathcal{I}^{\ell+1,k+1/2}. \tag{3.21}$$

Recall, the operator given by Eq. (3.12d),

$$\mathbf{D}=\frac{1}{c}+\int_{\Delta t}\mathbf{\Omega}\cdot\nabla\left(\cdot\right)\mathrm{d}t+\int_{\Delta t}\sigma\left(\cdot\right)\ \mathrm{d}t, \tag{3.22}$$

is simply a transport operator. Define $\mathcal{I}^{\ell+1,k+1/2}$ as the solution to the following transport equation,

$$(\mathbf{D})\mathcal{I}^{\ell+1,k+1/2}=(\mathbf{D}-\mathbf{C}\mathbf{A}^{-1}\mathbf{B})\mathcal{I}^{\ell}-r(U_m^{\ell},\mathcal{I}^{\ell})+(\mathbf{C}\mathbf{A}^{-1}\mathbf{B})\mathcal{I}^{\ell+1,k}. \tag{3.23}$$

All the terms on the right hand side of Eq. (3.23) are known and evaluated at a previous iteration. This amounts to solving a transport equation for $\mathcal{I}^{\ell+1,k+1/2}$

with the right side of Eq. (3.23). Importantly, the term responsible for effective-scattering has been approximated with a known scattering term,

$$(\mathbf{C}\mathbf{A}^{-1}\mathbf{B})\mathcal{I}^{\ell+1,k}. \tag{3.24}$$

The right hand side of the transport operator in Eq. (3.23) can be further simplified. Recall the definition of radiation residual,

$$r(U_m,\mathcal{I}) = \frac{1}{c}[\mathcal{I}-\mathcal{I}^n] + \left\{\int_{\Delta t}\mathbf{\Omega}\cdot\nabla\mathcal{I}\;\mathrm{d}t + \int_{\Delta t}\sigma\mathcal{I}\;\mathrm{d}t\right\} - \left[\Delta t\sigma c\frac{U_r}{4\pi}\right], \tag{3.25}$$

or, evaluated at a specific Newton index ℓ,

$$r(U_m^\ell,\mathcal{I}^\ell) = \frac{1}{c}[\mathcal{I}^\ell-\mathcal{I}^n] + \left\{\int_{\Delta t}\mathbf{\Omega}\cdot\nabla\mathcal{I}^\ell\;\mathrm{d}t + \int_{\Delta t}\sigma\mathcal{I}^\ell\;\mathrm{d}t\right\} - \left[\Delta t\sigma c\frac{U_r^\ell}{4\pi}\right]. \tag{3.26}$$

With some rearrangement, Eq.(3.26) can be written as

$$r(U_m^\ell,\mathcal{I}^\ell) = -\frac{\mathcal{I}^n}{c} + \left(\frac{\mathcal{I}^\ell}{c} + \left\{\int_{\Delta t}\mathbf{\Omega}\cdot\nabla\mathcal{I}^\ell\;\mathrm{d}t + \int_{\Delta t}\sigma\mathcal{I}^\ell\;\mathrm{d}t\right\}\right) - \left[\Delta t\sigma c\frac{U_r^\ell}{4\pi}\right]. \tag{3.27}$$

The terms in $(\cdot)$ are simply the transport operator

$$(\mathbf{D})\mathcal{I}^\ell = \frac{\mathcal{I}^\ell}{c} + \left\{\int_{\Delta t}\mathbf{\Omega}\cdot\nabla\mathcal{I}^\ell\;\mathrm{d}t + \int_{\Delta t}\sigma\mathcal{I}^\ell\;\mathrm{d}t\right\}, \tag{3.28}$$

and the radiation residual can be expressed as

$$r(U_m^\ell,\mathcal{I}^\ell) = -\frac{\mathcal{I}^n}{c} + (\mathbf{D})I^\ell - \left[\Delta t\sigma c\frac{U_r^\ell}{4\pi}\right]. \tag{3.29}$$

Next, substitute Eq. (3.29) back into Eq. (3.23) to obtain

$$(\mathbf{D})\mathcal{I}^{\ell+1,k+1/2} = (\mathbf{D}-\mathbf{C}\mathbf{A}^{-1}\mathbf{B})\mathcal{I}^{\ell} + \frac{\mathcal{I}^{n}}{c} - (\mathbf{D})I^{\ell} + \left[\Delta t\sigma c\frac{U_r^{\ell}}{4\pi}\right] + (\mathbf{C}\mathbf{A}^{-1}\mathbf{B})\mathcal{I}^{\ell+1,k}. \tag{3.30}$$

The right hand side can be further reduced to

$$(\mathbf{D})\mathcal{I}^{\ell+1,k+1/2} = \frac{\mathcal{I}^{n}}{c} + \left[\Delta t\sigma c\frac{U_r^{\ell}}{4\pi}\right] + (\mathbf{C}\mathbf{A}^{-1}\mathbf{B})(\mathcal{I}^{\ell+1,k} - \mathcal{I}^{\ell}). \tag{3.31}$$

The transport equation in Eq. (3.31) amounts to solving the time-continuous transport equation

$$\frac{1}{c}\frac{\partial}{\partial t}\mathcal{I}^{\ell+1,k+1/2} + \mathbf{\Omega}\cdot\nabla\mathcal{I}^{\ell+1,k+1/2} + \sigma\mathcal{I}^{\ell+1,k+1/2} = \sigma c\frac{U_r^{\ell}}{4\pi} + \xi\sigma c\left(E^{\ell+1,k} - E^{\ell}\right), \tag{3.32}$$

where

$$E^{(\cdot)} = \frac{1}{c}\int_{4\pi}\mathcal{I}^{(\cdot)}\mathrm{d}\mathbf{\Omega}, \tag{3.33}$$

and the term ξ will be discussed in the Diffusion Solution section.

3.3.1 Monte Carlo Implementation

A Monte Carlo algorithm, using implicit capture, is used to model the transport equation, Eq (3.32). The 1D Monte Carlo implementation can be summarized as follows. Each Monte Carlo particle is generated in a zone with an energy-weight

that is

$$w_0 = \frac{\text{total energy of the zone}}{\text{total number of particles per zone}}. \tag{3.34}$$

The weight change of a particle due to implicit capture along a path s can be written as

$$w = \int_0^s ds'\, w_0 \exp\{(-\sigma s')\} = \frac{1}{\sigma} w_0 \left[1 - \exp\{(-\sigma s)\}\right]. \tag{3.35}$$

The location at which a particle is created can be sampled by

$$x = x_{j,left} + \eta_1 (x_{j,right} - x_{j,left}) = x_{j,left} + \eta_1 \Delta x_j, \tag{3.36}$$

where $\eta_1 \in [0, 1]$ and is sampled using a pseudo-random number generator. The figure below illustrates the position sampling of a particle.

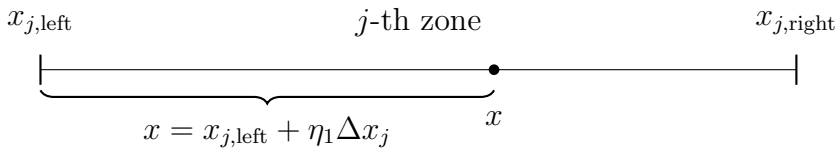

Figure 3.1: Position sampling using a pseudo-random number in 1D.

The direction of travel can be sampled with

$$\mu = 2\eta_2 - 1, \quad \eta_2 \in [0, 1], \tag{3.37}$$

where

$$\mu = \cos(\theta), \quad \mu \in [-1, 1], \tag{3.38}$$

and θ is the angle between the direction of travel and the x-axis.

As the governing transport equation has no scattering, only three interactions are possible. The particle either reaches census, reaches a boundary, or the particle's weight is below a cutoff threshold. When the particle's energy-weight falls below 1% of its original energy-weight, the particle is killed and the energy is deposited into the current zone. The distance to census can be sampled through

$$d_{census} = \eta_2 c \Delta t_n. \tag{3.39}$$

The distance to boundary can be obtained through

$$d_{boundary} = \frac{(x_{boundary} - x_0)}{\mu}, \tag{3.40}$$

where μ is the direction of travel, $x_{boundary}$ is the boundary in the direction of travel, and x_0 is the current location of a particle. The particle's birth location, distance to census, and distance to boundary are now prescribed by a set of pseudo-random numbers. The reflecting boundary conditions are treated by changing the sign for the direction of travel once a particle is at the boundaries of the problem.

3.4 The Diffusion Solution

In the previous section, the transport equation was defined as

$$(\mathbf{D})\mathcal{I}^{\ell+1,k+1/2} = (\mathbf{D} - \mathbf{C}\mathbf{A}^{-1}\mathbf{B})\mathcal{I}^{\ell} - r(U_m^{\ell}, \mathcal{I}^{\ell}) + (\mathbf{C}\mathbf{A}^{-1}\mathbf{B})\mathcal{I}^{\ell+1,k}. \tag{3.41}$$

Now, subtract $(\mathbf{CA}^{-1}\mathbf{B})\mathcal{I}^{\ell+1,k+1/2}$ from both sides

$$(\mathbf{D}-\mathbf{CA}^{-1}\mathbf{B})\mathcal{I}^{\ell+1,k+1/2} = (\mathbf{D}-\mathbf{CA}^{-1}\mathbf{B})\mathcal{I}^{\ell} - r(U_m^{\ell},\mathcal{I}^{\ell}) + (\mathbf{CA}^{-1}\mathbf{B})\mathcal{I}^{\ell+1,k} - (\mathbf{CA}^{-1}\mathbf{B})\mathcal{I}^{\ell+1,k+1/2}. \quad (3.42)$$

Recall Eq. (3.16),

$$(\mathbf{D}-\mathbf{CA}^{-1}\mathbf{B})(\mathcal{I}^{\ell+1,k+1/2}+\mathcal{I}^{\dagger}) = (\mathbf{D}-\mathbf{CA}^{-1}\mathbf{B})\mathcal{I}^{\ell} - r(U_m^{\ell},\mathcal{I}^{\ell}), \quad (3.43)$$

and subtract by Eq. (3.42) to obtain

$$(\mathbf{D}-\mathbf{CA}^{-1}\mathbf{B})\mathcal{I}^{\dagger} = \mathbf{CA}^{-1}\mathbf{B}(\mathcal{I}^{\ell+1,k+1/2}-\mathcal{I}^{\ell+1,k}). \quad (3.44)$$

Next, we expand Eq. (3.44)

$$\frac{1}{c}\frac{1}{\Delta t}I^{\dagger} + \mathbf{\Omega}\cdot\nabla I^{\dagger} + \sigma I^{\dagger} - \left(\frac{c\sigma\beta\Delta t}{4\pi}\right)\left(\frac{1}{1+\sigma_p c\beta\Delta t}\right)\left(\int_{4\pi}\sigma I^{\dagger}\mathrm{d}\mathbf{\Omega}\right) = \left(\frac{c\sigma\beta\Delta t}{4\pi}\right)\left(\frac{1}{1+\sigma_p c\beta\Delta t}\right)\left(\int_{4\pi}\sigma(I^{\ell+1,k+1/2}-I^{\ell+1,k})\mathrm{d}\mathbf{\Omega}\right). \quad (3.45)$$

Then, use the first and second angular moments,

$$I_0^{\dagger} = \int_{4\pi} I^{\dagger}\mathrm{d}\mathbf{\Omega}, \quad (3.46)$$

$$I_1^{\dagger} = \int_{4\pi} \mathbf{\Omega} I^{\dagger}\mathrm{d}\mathbf{\Omega}, \quad (3.47)$$

to write Eq. (3.45) as

$$\frac{1}{c}\frac{1}{\Delta t}I_0^\dagger + \nabla\cdot I_1^\dagger + \sigma I_0^\dagger - (c\sigma\beta\Delta t)\left(\frac{1}{1+\sigma_p c\beta\Delta t}\right)(\sigma I_0^\dagger) \\ = (c\sigma\beta\Delta t)\left(\frac{1}{1+\sigma_p c\beta\Delta t}\right)\Big(\sigma(I_0^{\ell+1,k+1/2} - I_0^{\ell+1,k})\Big). \quad (3.48)$$

Now, the diffusion approximation can be applied by using

$$I_1^\dagger = -D\nabla I_0^\dagger, \quad (3.49)$$

where

$$D = \frac{1}{3\sigma}, \quad (3.50)$$

and

$$I_1^\dagger = -\frac{1}{3\sigma}\nabla I_0^\dagger. \quad (3.51)$$

Eq. (3.48) can now be written as

$$\frac{1}{\Delta t}E^\dagger - \nabla\cdot cD\nabla E^\dagger + c\sigma E^\dagger - (c\sigma\beta\Delta t)\left(\frac{1}{1+\sigma c\beta\Delta t}\right)\big(c\sigma E^\dagger\big) \\ = (c\sigma\beta\Delta t)\left(\frac{1}{1+\sigma c\beta\Delta t}\right)\big(c\sigma(E^{\ell+1,k+1/2} - E^{\ell+1,k})\big), \quad (3.52)$$

where the radiation energy density is defined as

$$E^{(\cdot)} = \frac{1}{c}I_0^{(\cdot)} = \frac{1}{c}\int_{4\pi} I^{(\cdot)}\mathrm{d}\mathbf{\Omega}. \quad (3.53)$$

The final form of Eq. (3.52) can then be expressed as

$$-\nabla \cdot D\nabla E^{\dagger} + \tilde{\sigma_a} E^{\dagger} = \xi\sigma \left(E^{\ell+1,k+1/2} - E^{\ell+1,k} \right), \tag{3.54}$$

where

$$\tilde{\sigma_a} = \frac{1}{c\Delta t} + (1-\xi)\sigma, \tag{3.55}$$

and

$$\xi = (c\sigma\beta\Delta t)(\frac{1}{1+\sigma c\beta\Delta t}). \tag{3.56}$$

Once the transport and diffusion solutions have been obtained from Eq. (3.32) and Eq. (3.54), the next estimate of the radiation energy density is then

$$E^{\ell+1,k+1} = E^{\ell+1,k+1/2} + E^{\dagger}. \tag{3.57}$$

Eq. (3.57) will either be used for another transport-diffusion calculation and, upon convergence of the Newton iteration, it will be used in solving the material energy residual equation.

3.5 The Material Energy Residual

The material energy residual for our system is defined as

$$m(U_m^{\ell}, \mathcal{I}^{\ell}) = U_m^{\ell} - U_m^{n} + \Delta t\sigma c U_r^{\ell} - \left\{ \int_{\Delta t} \int_{4\pi} \sigma \mathcal{I}^{\ell} \mathrm{d}\mathbf{\Omega}\ \mathrm{d}t \right\} = 0, \tag{3.58}$$

or, in terms of the radiation energy density,

$$m(U_m^\ell, \mathcal{I}^\ell) = U_m^\ell - U_m^n + \Delta t \sigma c U_r^\ell - c\left\{\int_{\Delta t} \sigma E^\ell \, \mathrm{d}t\right\} = 0. \tag{3.59}$$

Next, we define

$$U_m^\ell = \rho c_v T_{\ell,i} \, , \tag{3.60}$$

$$U_r^\ell = a T_{\ell,i}^4 \, , \tag{3.61}$$

and insert into Eq. (3.59) to find

$$m(U_m^\ell, \mathcal{I}^\ell) = \rho c_v T_{\ell,i} - \rho c_v T_n + \Delta t \sigma_n c a T_{\ell,i}^4 - c\left\{\int_{\Delta t} \sigma E^\ell \, \mathrm{d}t\right\} = 0. \tag{3.62}$$

Eq. (3.62) is solved using a local Newton solver with an iteration index i. This is the final equation required for DAIMC.

3.6 Summary

In this chapter, the mathematical framework for Diffusion Accelerated Implicit Monte Carlo (DAIMC) was derived. Nonlinear elimination and solution splitting were applied to the TRT equations. This resulted in a transport equation with the absence of scattering. DAIMC can be summarized by solving three equations, namely Eq. (3.62), Eq. (3.32), and Eq. (3.54). An algorithm outline for DAIMC is given below.

Algorithm 1: Diffusion Accelerated Implicit Monte Carlo

while $t_n < t_{max}$ **do**
  Set $\ell = 0$
  Guess $E^{\ell} = E^0 = E^n$
  while $T_{\ell,i+1}$ *not converged* **do**
    Solve Eq. (3.62)
  end
  Set $U_r^{\ell} =$ Eq. (3.61)
  while $T_{\ell+1}$ *not converged* **do**
    $k = 0$, $E^{\ell+1,k} = E^{\ell}$
    while $E^{\ell+1,k+1}$ *not converged* **do**
      Solve Eq. (3.32) for $E^{\ell+1,k+1/2}$
      Use $E^{\ell+1,k+1/2}$ to solve Eq. (3.54) for $E^{\dagger}$
      $E^{\ell+1,k+1} = E^{\ell+1,k+1/2} + E^{\dagger}$
    end
    Set $E^{\ell+1} = E^{\ell+1,k+1}$
    while $T_{\ell+1,i+1}$ *not converged* **do**
      Solve Eq. (3.62)
    end
    Set $U_r^{\ell+1} =$ Eq. (3.61)
    $\ell = \ell + 1$
  end
  $t_n = t_n + \Delta t$
end

Chapter 4: Results

4.1 Introduction

In this chapter, we begin by performing verification tests of the DAIMC method. As detailed in the previous chapter, DAIMC requires three different solvers: a diffusion solver, a Monte Carlo transport solver, and a Newton solver for the material residual equation. The verification of these solvers can be found in Appendix B. In section 4.2, DAIMC results for several 1D grey TRT test cases are generated and compared with IMC. In section 4.3, DAIMC results for several 2D-XY test problems are presented. Note, all test problems involve reflecting boundary conditions in the transport and diffusion solvers. This is not a limitation of the methodology, but it is currently a limitation of the software implementation.

4.2 1D Slab Geometry

The purpose of the following series of test problems is to verify the behavior of DAIMC in 1D. We begin with the 1D grey TRT equations in the absence of external sources and scattering,

$$\frac{1}{c}\frac{\partial \mathcal{I}}{\partial t} + \mu\frac{\partial \mathcal{I}}{\partial x} + \sigma\mathcal{I} = \frac{1}{2}\sigma B, \tag{4.1}$$

and

$$\frac{\partial U_m}{\partial t} = \int_{-1}^{1} \sigma(\mathcal{I} - 2B)\mathrm{d}\mu'. \tag{4.2}$$

Impose the following initial and boundary conditions:

$$T^i(x) = T_0, \tag{4.3a}$$

$$I^i(x,\mu) = \frac{1}{2}B(T_0), \tag{4.3b}$$

$$I^l(\mu) = \frac{1}{2}B(T_0). \tag{4.3c}$$

Using the definition of Planck's function, Eq. (4.1) and Eq. (4.2) can be written as

$$\frac{1}{c}\frac{\partial I}{\partial t} + \mu\frac{\partial I}{\partial x} + \sigma I = \frac{1}{2}\sigma c U_r, \tag{4.4}$$

$$\frac{\partial U_m}{\partial t} + \sigma c U_r = \int_0^{\infty}\int_{-1}^{1} \sigma I \mathrm{d}\mu'. \tag{4.5}$$

The exact solution for a grey, purely-absorbing, homogenous, and infinite medium problem is

$$\frac{\mathrm{d}E}{\mathrm{d}t} = c\sigma(aT^4 - E), \tag{4.6}$$

and

$$\frac{\mathrm{d}U_m}{\mathrm{d}t} = -c\sigma(aT^4 - E), \tag{4.7}$$

or,

$$\frac{\mathrm{d}T_m}{\mathrm{d}t} = \frac{-c\sigma}{\rho c_v}(aT^4 - E), \tag{4.8}$$

where E is the radiation energy density [39]. The coupled set of equations, Eq. (4.6) and Eq. (4.8), are solved using the SciPy Python package and are considered the analytic solutions for the radiation field temperature and material temperature, respectively. Note, the radiation energy density is the quantity of interest, but, for verification purposes, it is often expressed as the radiation temperature. A derived quantity, the effective radiation "temperature", T_r, is computed by equating the local radiation energy density to $a(T_r)^4$ because $E_r \equiv \int_{4\pi} d\Omega \int_o^\infty d\nu I$, and if $I = B(\nu, T)$, as it does at equilibrium, then $E_r = aT^4$. This quantity will be distinct from the material temperature when the radiation and the matter are out of equilibrium. T_r has no physical meaning, but mathematically it provides a way to observe the evolution to equilibrium through two distinct temperatures. The following results in 1D slab geometry has a tolerance of $\epsilon = 1.0 \cdot 10^{-3}$ for all three convergence criterion.

4.2.1 Equilibrium

A simple test problem is used to verify the equilibrium behavior of DAIMC. The problem starts with the material and the radiation field in equilibrium. The problem simulates a slab of length 1.0 cm with 20 equally spaced zones and 100k particles per zone. The opacity is assumed to be uniform throughout the slab and has a value of $\sigma = 29.0$ cm^{-1}. The time step size is $\Delta = 1.0 \cdot 10^{-8}$ sh and a total of 10 steps were simulated. The results are given below.

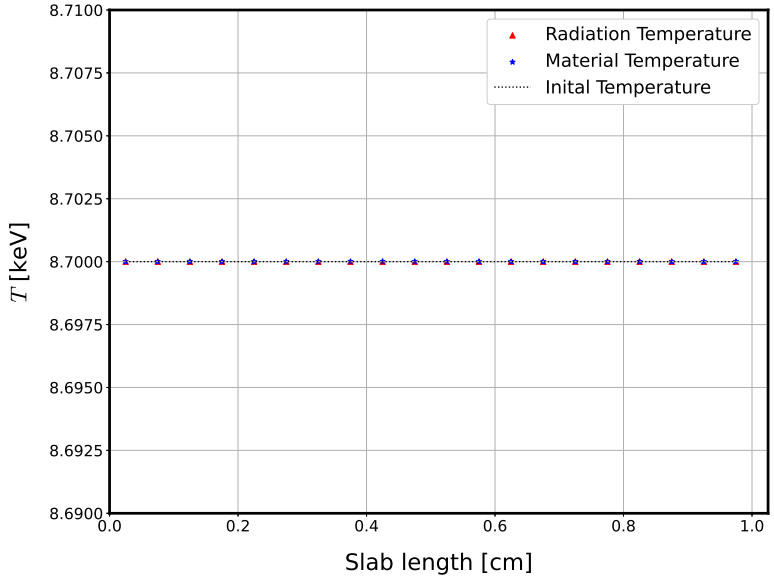

Figure 4.1: Initial temperatures for the 1D equilibrium test.

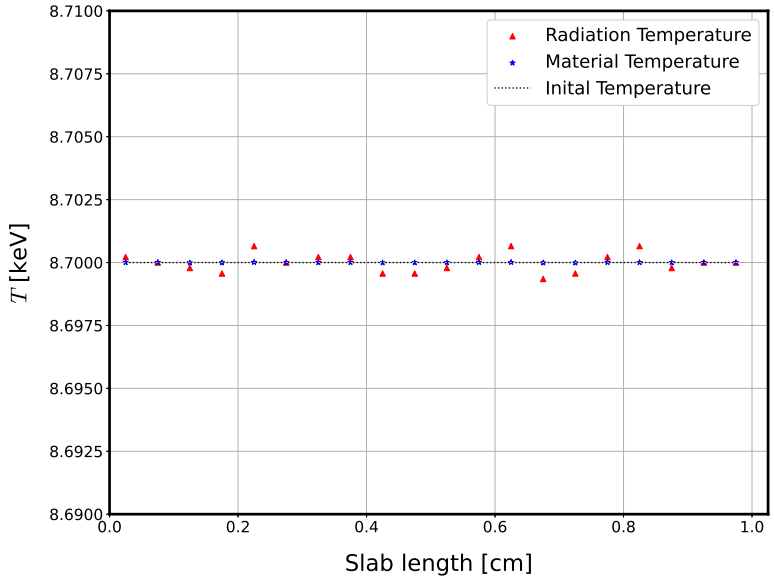

Figure 4.2: The final temperatures for the 1D equilibrium test.

The purpose of this problem is to verify the behavior of DAIMC when beginning in equilibrium. It is expected that the material temperature and radiation temperature are the same for the beginning and end of the simulation. This can be observed in Figure 4.1 and Figure 4.2.

4.2.2 Equilibration

The next test problem simulates the equilibration of the material and radiation field when starting out of equilibrium. The problem simulates a slab with a length of 1.0 cm, 10 equally spaced zones, and 100k particles per zone. The opacity is assumed to be uniform throughout the slab and has a value of $\sigma = 13.0$ cm^{-1}. The time step size is $\Delta t = 1.0 \cdot 10^{-5}$ sh, where a total of 100 steps are simulated. The material has an initial temperature of $T_m = 8.0$ and the radiation field has an initial temperature of $T_r = 0.01$. The results are given below.

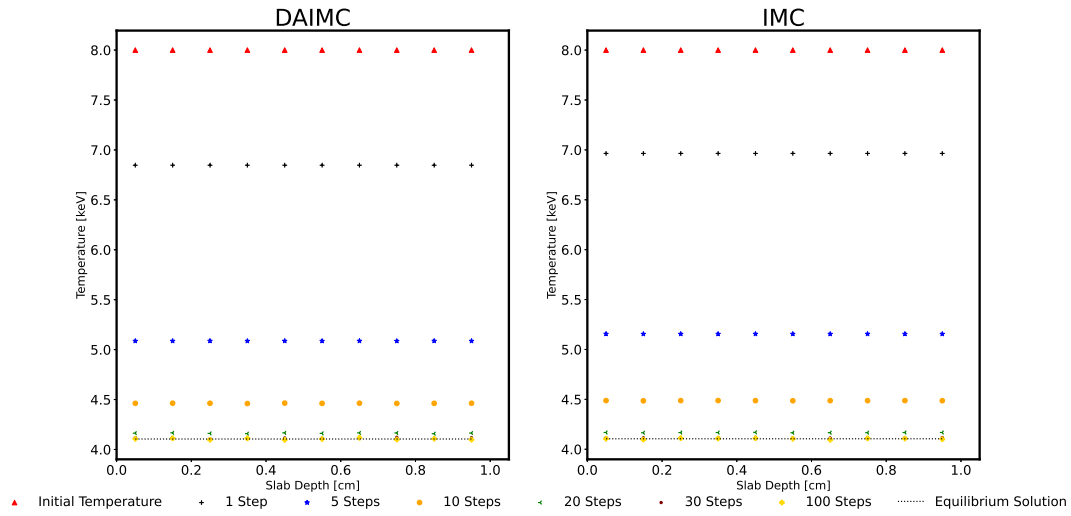

Figure 4.3: The material temperatures of DAIMC and IMC for the 1D equilibration test.

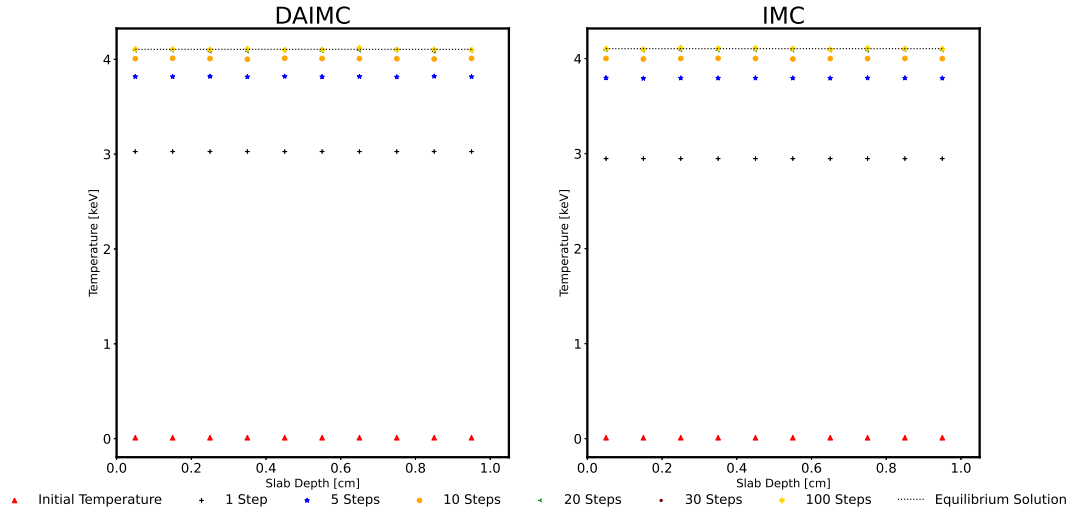

Figure 4.4: The radiation temperatures of DAIMC and IMC for the 1D equilibration test.

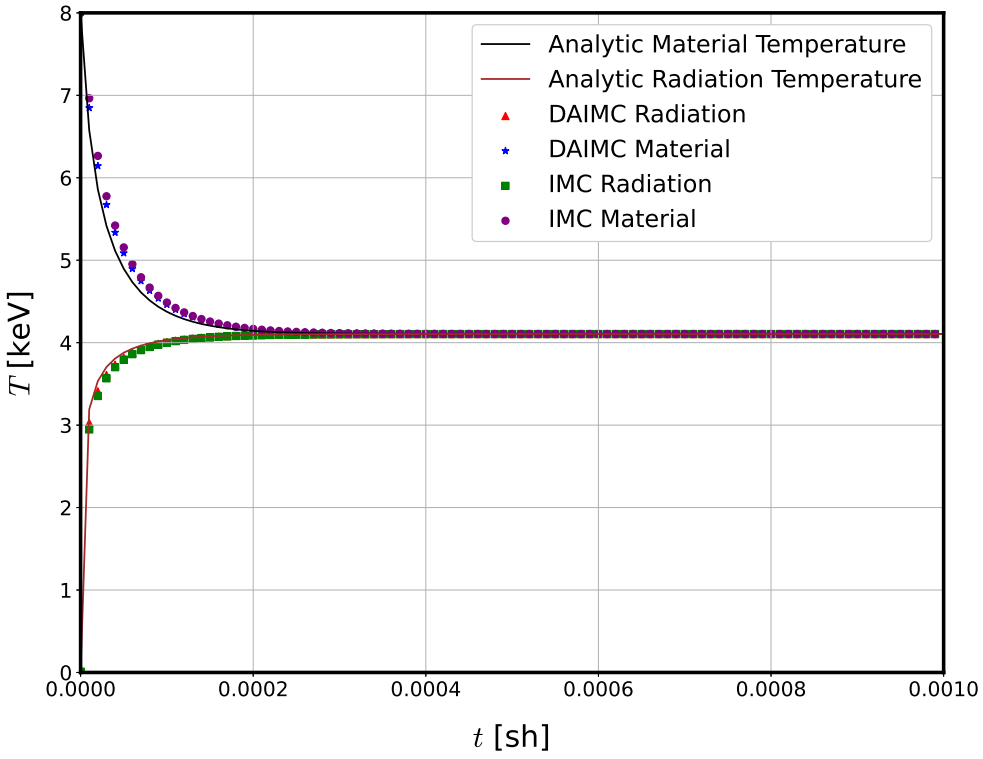

Figure 4.5: Time evolution of the analytic solutions for the 1D equilibration test.

Method	Variable	l_2-norm	inf-norm
DAIMC	Material temp.	0.00637	0.28501
	Radiation temp.	0.00263	0.16429
IMC	Material temp.	0.00881	0.40640
	Radiation temp.	0.00379	0.24425

Table 4.1: The norms of IMC and DAIMC for the 1D equilibration test.

The DAIMC results in Figure 4.3 and Figure 4.4 illustrate the expected behavior for this test problem. The material and radiation field comes to an equilibrium with a temperature given by Eq. (4.6) and Eq. (4.8). This can be confirmed in Figure 4.5. Two different norms for the DAIMC and IMC method are given in Table 4.1. The results indicate DAIMC gives a closer estimate to the analytic solution when compared with IMC.

4.2.3 Hot and Cold Zones

The next test case involves a material having a 'hot zone' and a 'cold zone' in order to simulate a wave. A slab with length 4.0 cm is modeled by 10 uniform cells (Δx = 0.4 cm), $\sigma = 13.0$ cm^{-1}, and $\Delta t = 1.0 \cdot 10^{-4}$ sh. The first 4 cells from the left boundary start at an initial material temperature of 123.0 keV. The remaining 6 cells' initial material, and all initial radiation temperatures, have a value of 0.01 keV. We allow this problem to run until equilibrium.

The analytic equilibrium temperature is given by

$$(aT^4 + \rho c_v T)V_{total} = \sum_{i=1}^{Z}(T_{r,i}^4 + \rho c_v T_{m,i})V_i, \tag{4.9}$$

where Z is the total number of zones, i is a particular zone, and V_{total} is the total volume of the problem. Solving Eq.(4.9) yields four solutions for the final equilibrium temperature (T). Of these four solutions, three will involve a combination of negative and complex temperatures, and only one solution is physically meaningful. The physically meaningful solution yields a positive temperature and is plotted as the analytical solution.

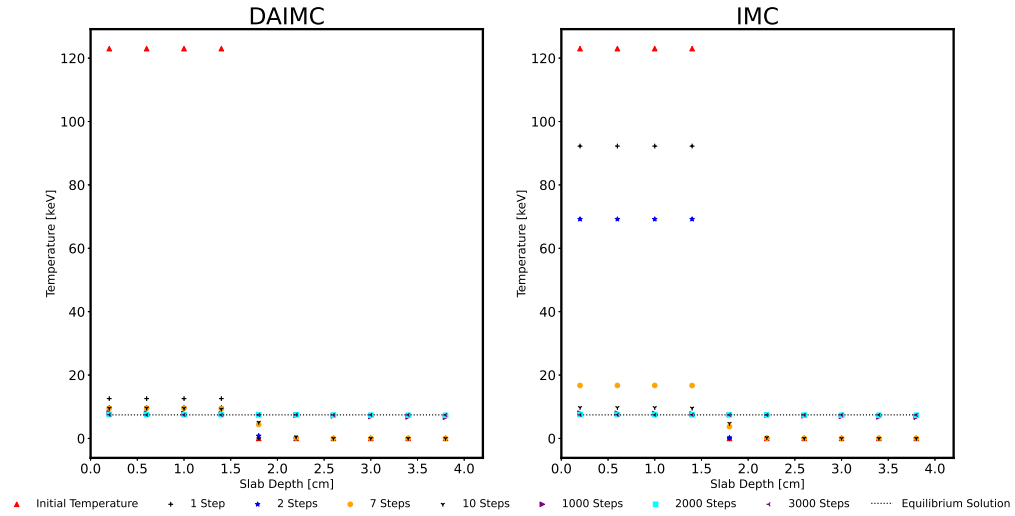

Figure 4.6: Time evolution of the material temperatures using DAIMC and IMC for the hot and cold zone test .

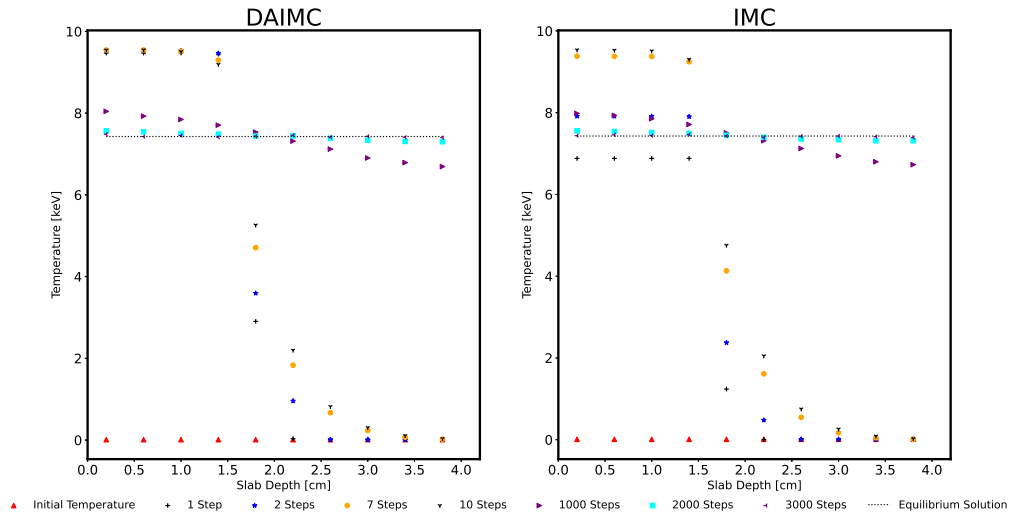

Figure 4.7: Time evolution of the radiation temperatures using DAIMC and IMC for the hot and cold zone test.

This test problem aims to verify DAIMC by introducing nonuniform initial conditions. Figure 4.6 and Figure 4.7 illustrate that DAIMC converges to the correct equilibrium temperature. For comparison, results obtained using IMC are also plotted in the same figures.

4.2.4 Quasi-Monte Carlo

Quasi-Monte Carlo (QMC) is a method in which the pseudo-random numbers of Monte Carlo are replaced with a deterministic sequence of numbers [40]–[43]. These sequences typically include the Halton sequence and the Sobol sequence [44], [45]. QMC is designed to have a more uniform distribution than traditional pseudo-

random numbers, thus resulting in faster convergence. QMC becomes less effective for problems in which the dimensions become extremely large [42]. For problems involving particle transport, the dimension increases as the particle interacts. More specifically, the dimension of QMC increases with more scattering or effective-scattering events. Since DAIMC does not have scattering as an interaction, QMC may prove to be effective at increasing the convergence rate.

The following results compare DAIMC using a pseudo-random number generator, DAIMC sampled from a Sobol sequence, as well as the traditional IMC method. The problem models a slab with a length of 1.0 cm using four equally spaced zones of size $\Delta = 0.25$ cm. The problem specifications are $\Delta t = 1.0 \cdot 10^{-5}$. The material has an initial temperature of 8.0 keV and the radiation has an initial temperature of 0.001 keV. The results below utilized three different values for the opacity, $\sigma = 13.0\ \text{cm}^{-1}, 1,300.0\ \text{cm}^{-1}$ and $13,000.0\ \text{cm}^{-1}$.

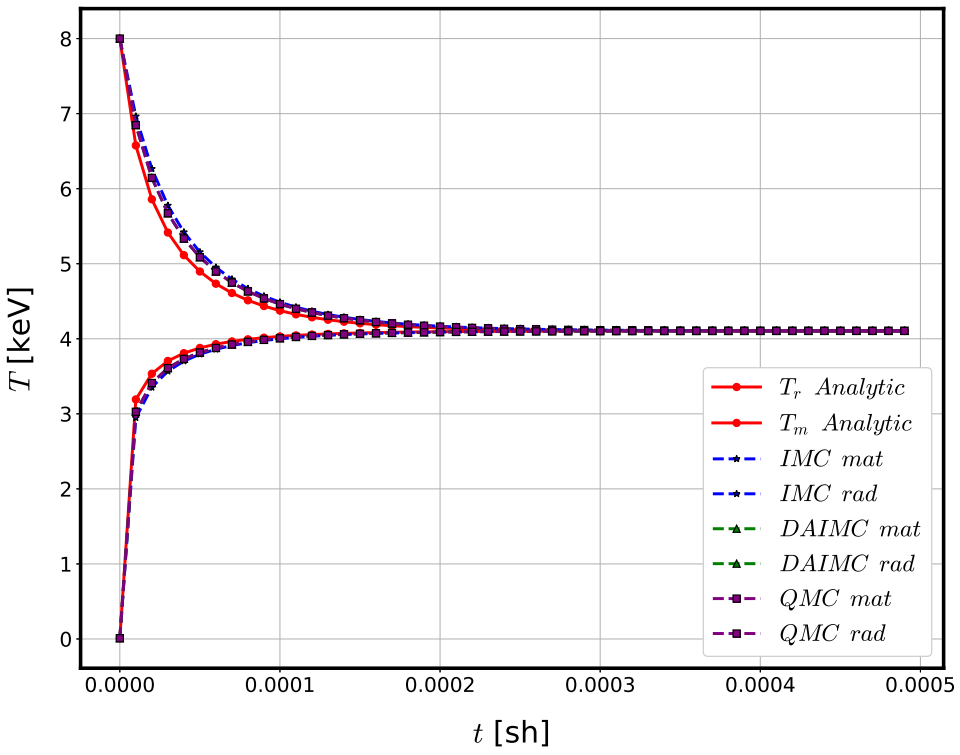

Figure 4.8: The temperatures from DAIMC, IMC, and QMC implementation of DAIMC using $\sigma = 13.0$.

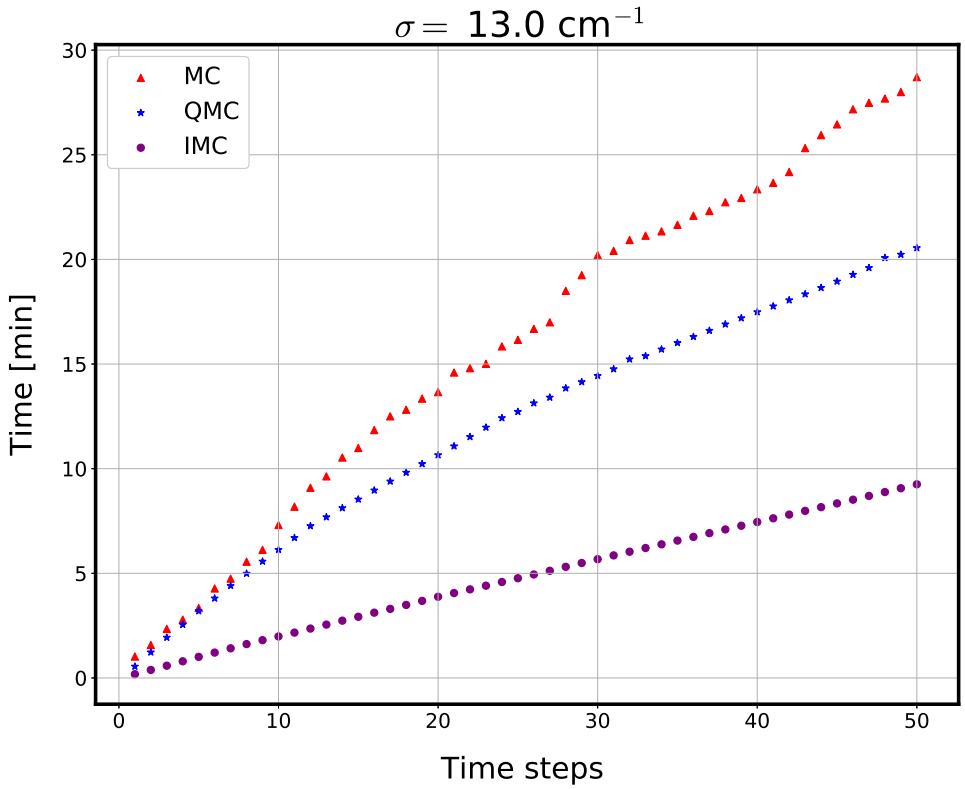

Figure 4.9: The run-time for the MC and QMC implementation of DAIMC, and IMC using $\sigma = 13.0$.

Method	Variable	ℓ_2-error	ℓ_∞-error
IMC	Material temp.	$1.762 \cdot 10^{-2}$	$4.064 \cdot 10^{-1}$
	Radiation temp.	$7.582 \cdot 10^{-3}$	$2.442 \cdot 10^{-1}$
MC	Material temp.	$1.273 \cdot 10^{-2}$	$2.850 \cdot 10^{-1}$
	Radiation temp.	$5.264 \cdot 10^{-3}$	$1.643 \cdot 10^{-1}$
QMC	Material temp.	$1.273 \cdot 10^{-2}$	$2.850 \cdot 10^{-1}$
	Radiation temp.	$5.264 \cdot 10^{-3}$	$1.643 \cdot 10^{-1}$

Table 4.2: The norms of the error for IMC, and the MC and QMC implementation of DAIMC in the 1D equilibration test using $\sigma = 13.0$ cm^{-1}.

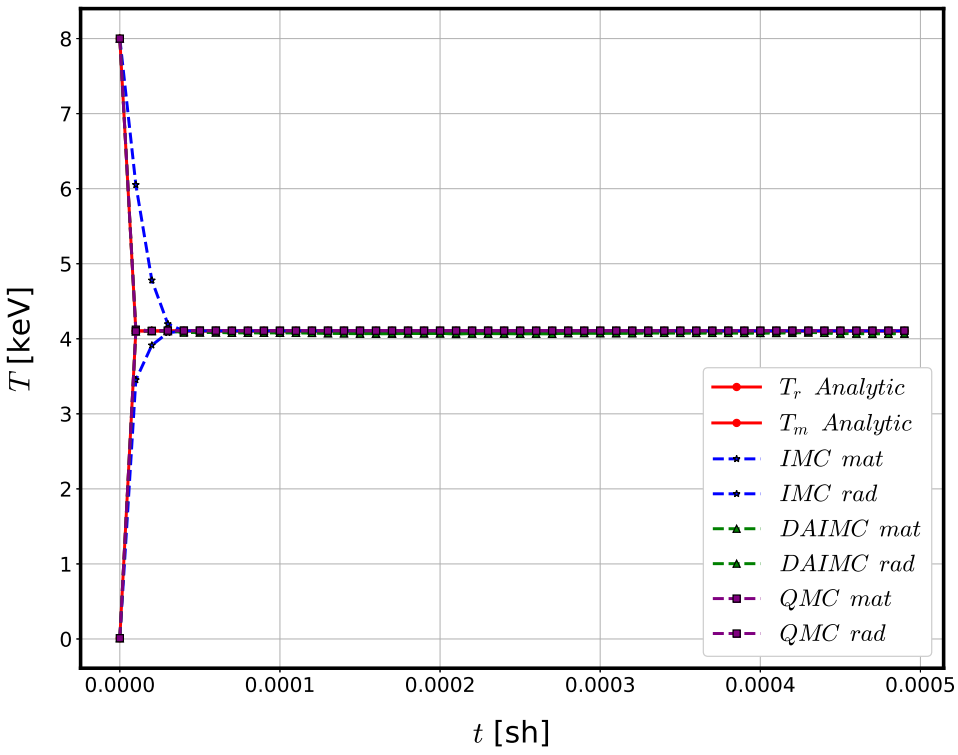

Figure 4.10: The temperatures from DAIMC, IMC, and QMC implementation of DAIMC using $\sigma = 1,300.0$.

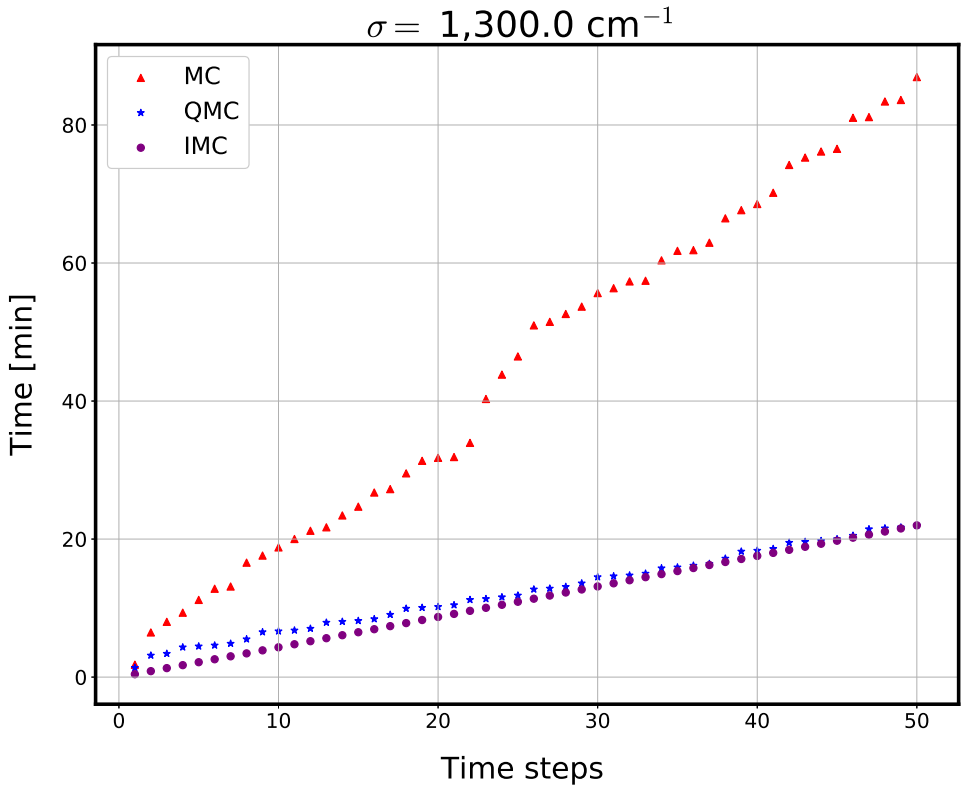

Figure 4.11: The run-time for the MC and QMC implementation of DAIMC, and IMC using $\sigma = 1,300.0$.

Method	Variable	ℓ_2-error	ℓ_∞-error
IMC	Material temp.	$4.127 \cdot 10^{-2}$	$1.948 \cdot 10^{0}$
	Radiation temp.	$1.362 \cdot 10^{-2}$	$6.532 \cdot 10^{-1}$
MC	Material temp.	$4.083 \cdot 10^{-3}$	$4.173 \cdot 10^{-2}$
	Radiation temp.	$4.079 \cdot 10^{-3}$	$3.955 \cdot 10^{-2}$
QMC	Material temp.	$4.542 \cdot 10^{-4}$	$1.674 \cdot 10^{-2}$
	Radiation temp.	$3.292 \cdot 10^{-4}$	$4.752 \cdot 10^{-3}$

Table 4.3: The norms of the error for IMC, and the MC and QMC implementation of DAIMC in the 1D equilibration test using $\sigma = 1,300.0$ cm^{-1}.

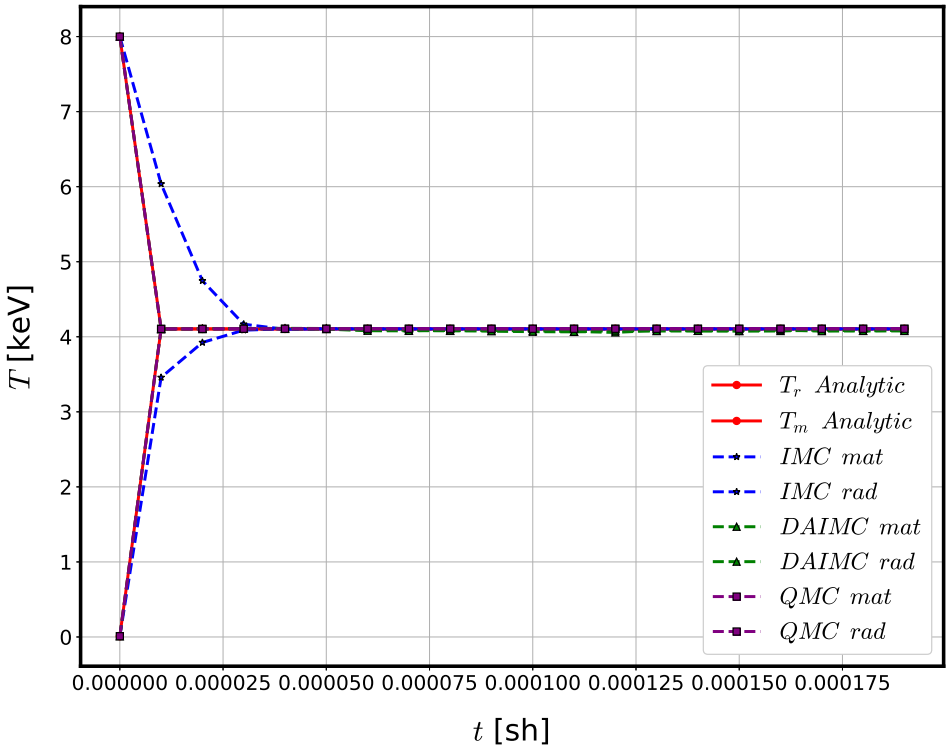

Figure 4.12: The temperatures from DAIMC, IMC, and QMC implementation of DAIMC using $\sigma = 13,000.0$.

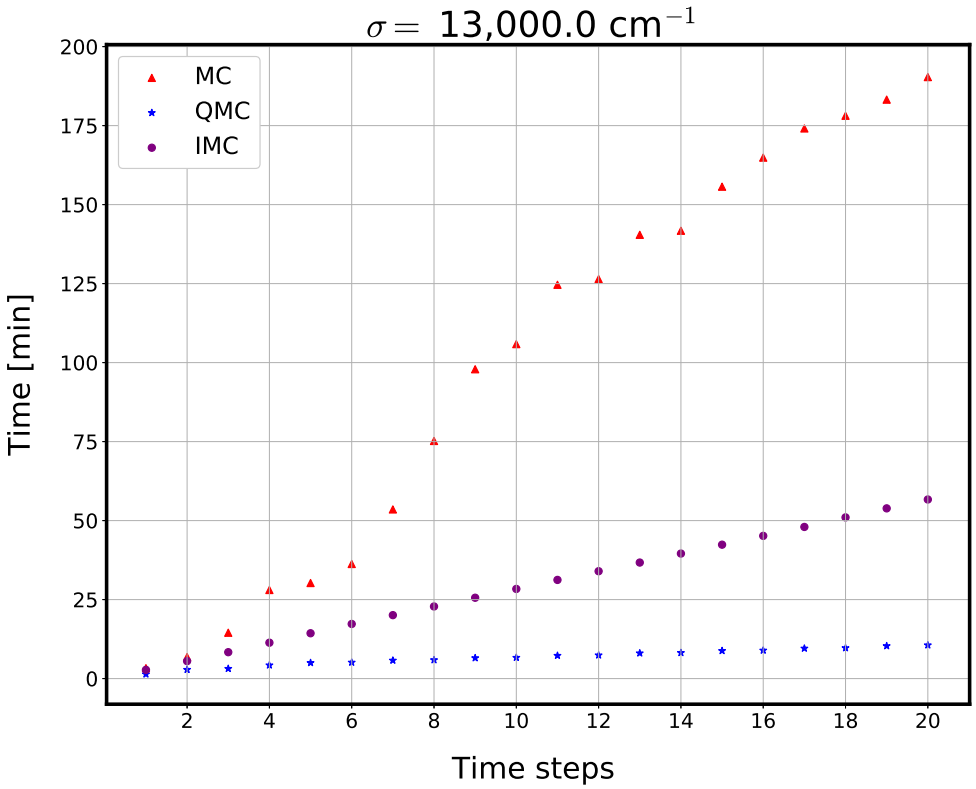

Figure 4.13: The run-time for the MC and QMC implementation of DAIMC, and IMC using $\sigma = 13,000.0$.

Method	Variable	ℓ_2-error	ℓ_∞-error
IMC	Material temp.	$1.018 \cdot 10^{-1}$	$1.932 \cdot 10^{0}$
	Radiation temp.	$3.356 \cdot 10^{-2}$	$6.462 \cdot 10^{-1}$
MC	Material temp.	$4.891 \cdot 10^{-3}$	$4.651 \cdot 10^{-2}$
	Radiation temp.	$5.136 \cdot 10^{-3}$	$3.919 \cdot 10^{-2}$
QMC	Material temp.	$2.936 \cdot 10^{-4}$	$1.575 \cdot 10^{-3}$
	Radiation temp.	$2.990 \cdot 10^{-4}$	$1.680 \cdot 10^{-3}$

Table 4.4: The norms of the error for IMC, and the MC and QMC implementation of DAIMC in the 1D equilibration test using $\sigma = 13,000$ cm^{-1}.

In Figures 4.9, 4.11, 4.13, the lines labeled 'MC' represent the Monte Carlo implementation of DAIMC and the lines labeled 'QMC' represent the QMC implementation of DAIMC. The IMC method has a shorter run-time than the MC implementation of DAIMC for all three test cases ($\sigma = 13.0$ cm^{-1}, $1,300.0$ cm^{-1} and $13,000.0$ cm^{-1}). However, the MC implementation has a smaller norm of the error when compared to the IMC method, as shown in Tables 4.2, 4.3, and 4.4. The QMC implementation has the smallest norm of the error of the three methods. For smaller opacities, such as $\sigma = 13.0$, the QMC implementation has a longer run-time than the IMC method, as shown in Figure 4.9. The QMC implementation starts to have comparable run-time to IMC for $\sigma = 1,300.0$ and is faster than the IMC method for $\sigma = 13,000.0$, as shown in Figures 4.11 and 4.13.

4.3 2D-XY Geometry

The 2D implementation of DAIMC used a Monte Carlo transport code called Hoth. Hoth is a research code developed at LLNL and was built on the framework of solving the TRT equations as a Newton system (as discussed in Chapter 2). Modifications were made to Hoth in order to implement DAIMC. The diffusion equation is solved using the finite element library developed at LLNL called MFEM [46], [47]. Unless stated otherwise, the opacity will be modeled by

$$\sigma = \rho\kappa, \tag{4.10}$$

where ρ $[\frac{\text{g}}{\text{cm}^3}]$ is the density and κ $[\frac{\text{cm}^2}{\text{g}}]$ is the cross section. Results for several test problems are provided in the subsequent sections.

4.3.1 Equilibrium

The first test case in 2D-XY geometry follows that of section 4.2.1, where the equilibrium behavior of DAIMC is verified. A square with a length of 2.0 cm is divided into 9 equally spaced zones, where the material and radiation field start in equilibrium. The following problem specifications are used: $T_m = T_r = 1.4$ keV, $\Delta t = 1.0 \cdot 10^{-3}$ sh and 10 total time steps, $c_v = 0.1$, $\rho = 0.005$ $[\frac{\text{g}}{\text{cm}^3}]$, and $\kappa = 10.0$ $[\frac{\text{cm}^2}{\text{g}}]$.

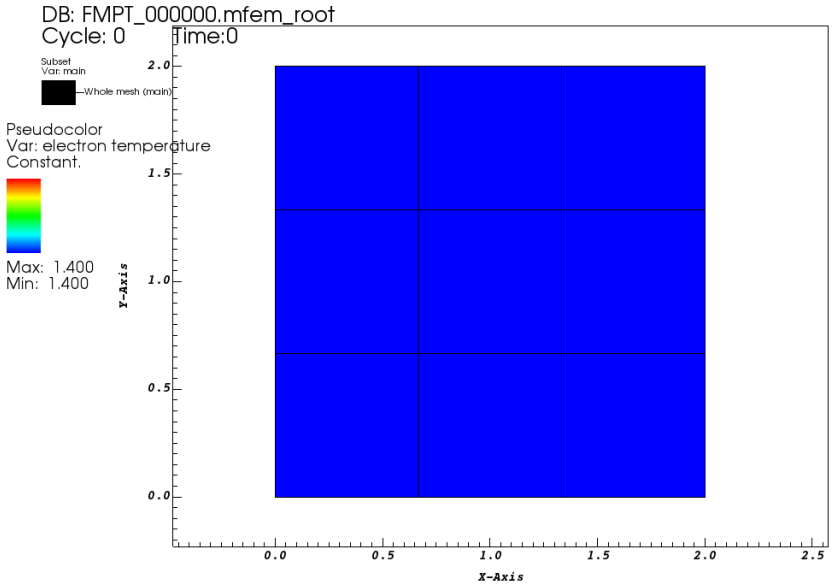

Figure 4.14: The initial material temperatures using DAIMC for the 2D equilibrium test.

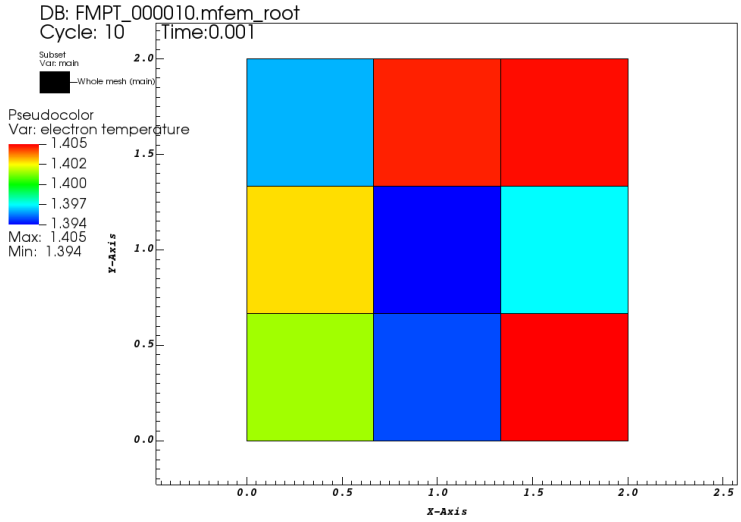

Figure 4.15: The final material temperatures using DAIMC for the 2D equilibrium test.

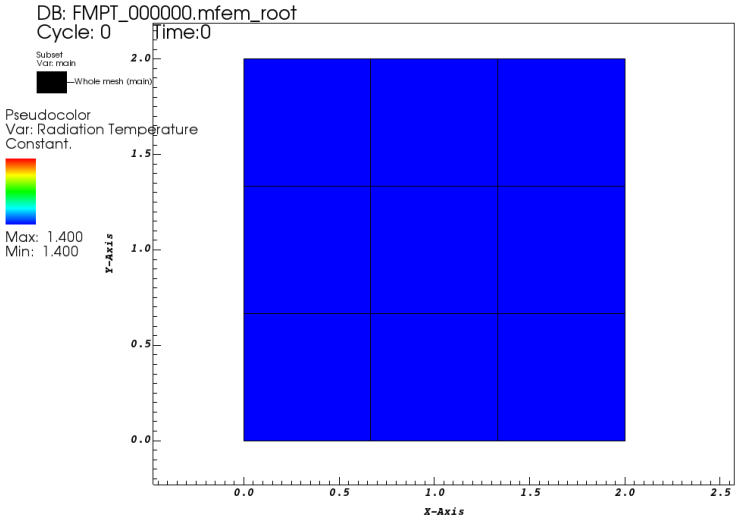

Figure 4.16: The initial radiation temperatures using DAIMC for the 2D equilibrium test.

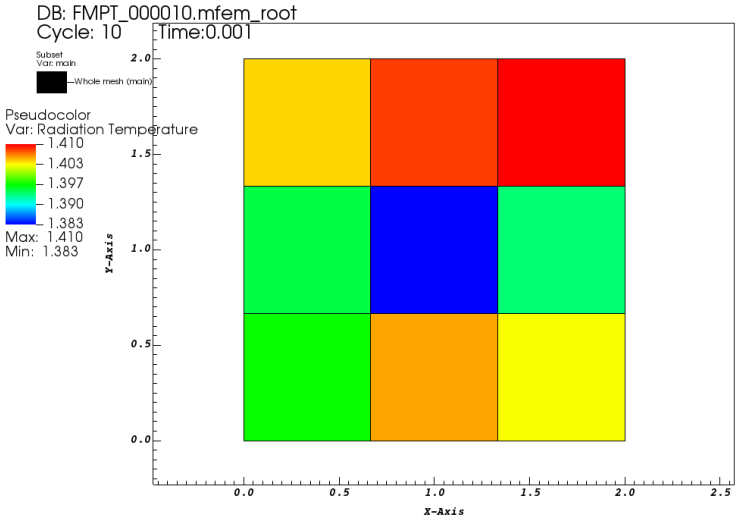

Figure 4.17: The final radiation temperatures using DAIMC for the 2D equilibrium test.

It is expected that the material temperature and radiation temperature remain constant for the duration of the simulation. This can be observed when comparing the initial material temperatures and the initial radiation temperatures in Figure 4.14 and Figure 4.16 to the final material and radiation temperatures in Figure 4.15 and Figure 4.17. This behavior indicates that DAIMC has been implemented correctly for cases where the material and radiation temperatures start at equilibrium in 2D-XY geometry.

4.3.2 Equilibration

The next test problem simulates the equilibration of the material and radiation field when starting out of equilibrium. A square with a length of 2.0 cm is divided into 9 equally spaced zones. Each zone has a radiation temperature of $T_r = 2.0$ keV and a material temperature of $T_m = 0.001$ keV. The time step size is $\Delta t = 1.0 \cdot 10^{-5}$ sh and a total of 100 time steps are simulated. The opacity is modeled with $\kappa = 50.0$, $c_v = 0.4382$, and $\rho = 1.0$.

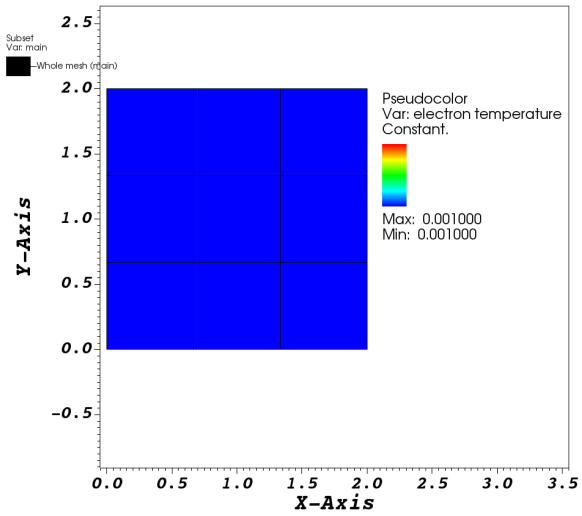

Figure 4.18: The initial material temperatures of DAIMC for the 2D equilibration test.

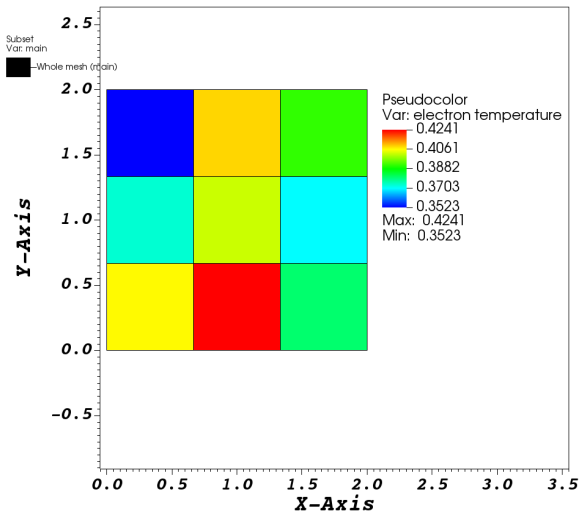

Figure 4.19: The material temperatures after 10 time steps of DAIMC for the 2D equilibration test using 1k particles per time step.

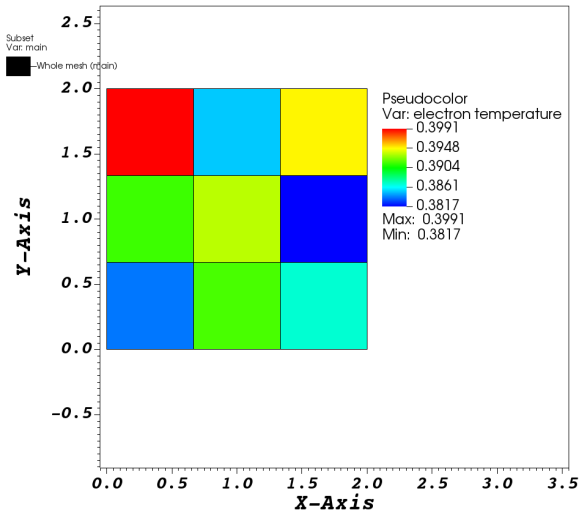

Figure 4.20: The material temperatures after 10 time steps of DAIMC for the 2D equilibration test using 10k particles per time step.

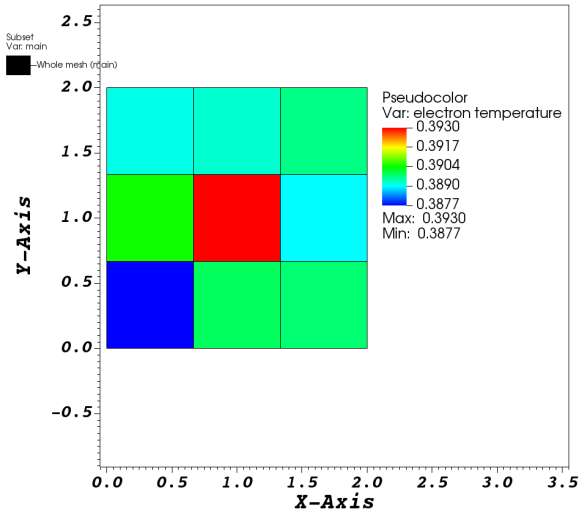

Figure 4.21: The material temperatures after 10 time steps of DAIMC for the 2D equilibration test using 100k particles per time step.

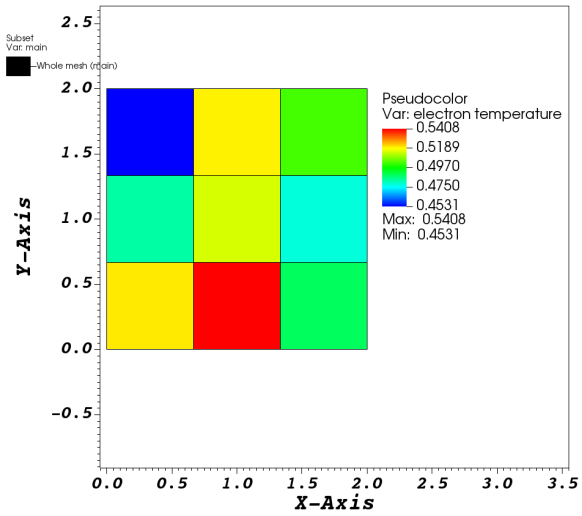

Figure 4.22: The final material temperatures of DAIMC for the 2D equilibration test using 1k particles per time step.

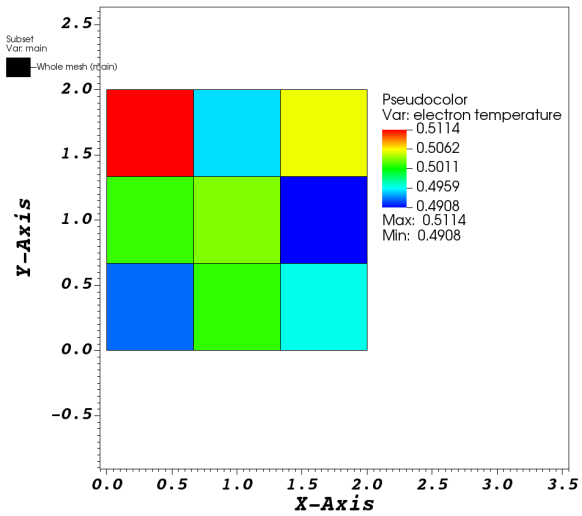

Figure 4.23: The final material temperatures of DAIMC for the 2D equilibration test using 10k particles per time step.

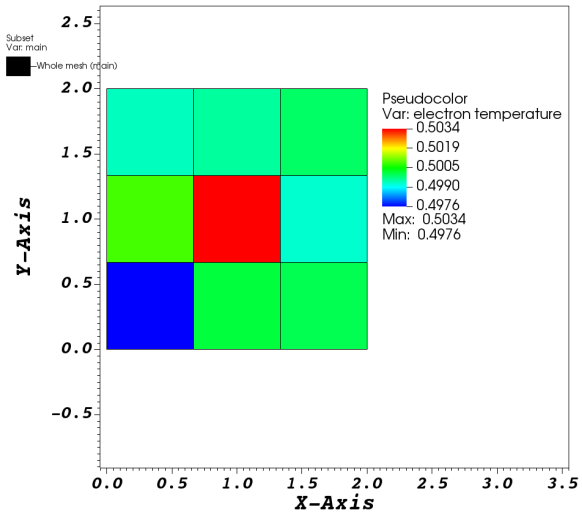

Figure 4.24: The final material temperatures of DAIMC for the 2D equilibration test using 100k particles per time step.

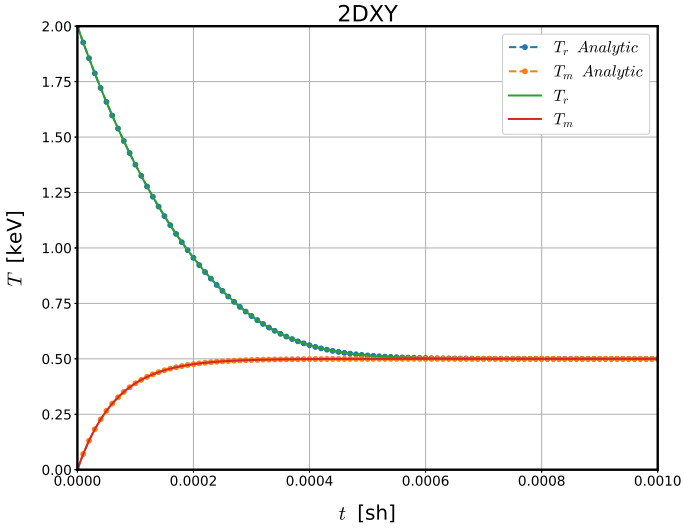

Figure 4.25: The time evolution of the temperatures for an equivalent single zone problem.

For verification purposes, the analytic solution can be obtained by running an equivalent 1 zone problem in 2D-XY geometry. The equilibrium solution is given in Figure 4.25. The equilibrium temperatures from Figures 4.22, 4.23 and 4.24 follow the equilibrium temperature given in Figure 4.25. This confirms the correct implementation of DAIMC for the constant opacity test problem when starting out of equilibrium.

4.3.3 Hot and Cold Zones

The next test case involves a material having a 'hot zone' and a 'cold zone' to simulate a wave. A square with a length of 2.0 cm is modeled with 20 zones. The 'hot' zones have an initial material temperature of 4.3 keV and the 'cold' zones have an initial material temperature of 0.001 keV. The radiation temperatures for all zones have an initial value of 0.001 keV. The material is uniform in each zone and has the following properties: $\rho = 0.4$, $\kappa = 5.0$, and $c_v = 1.0$. The time step is chosen as $\Delta t = 1.0 \cdot 10^{-4}$ sh and we allow this problem to run until equilibrium.

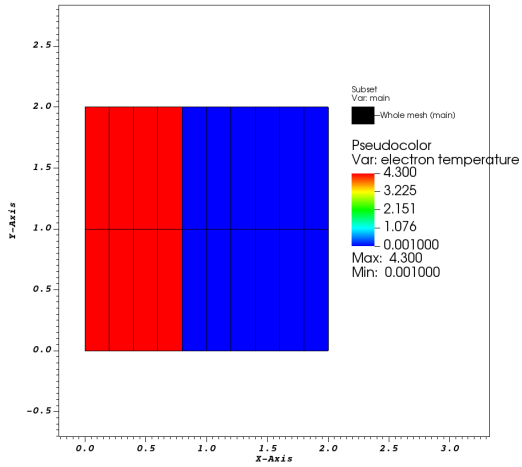

Figure 4.26: The initial DAIMC material temperatures for the 2D hot and cold zone problem.

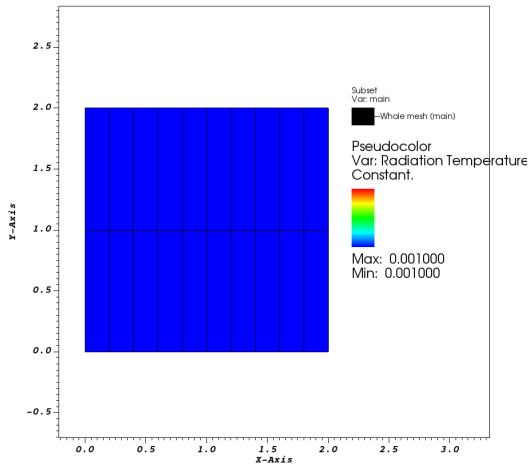

Figure 4.27: The initial DAIMC radiation temperatures for the 2D hot and cold zone problem

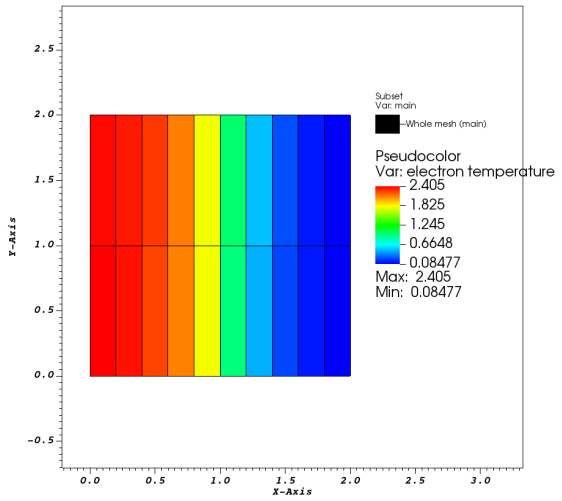

Figure 4.28: The DAIMC material temperatures after 100 time steps for the 2D hot and cold zone problem.

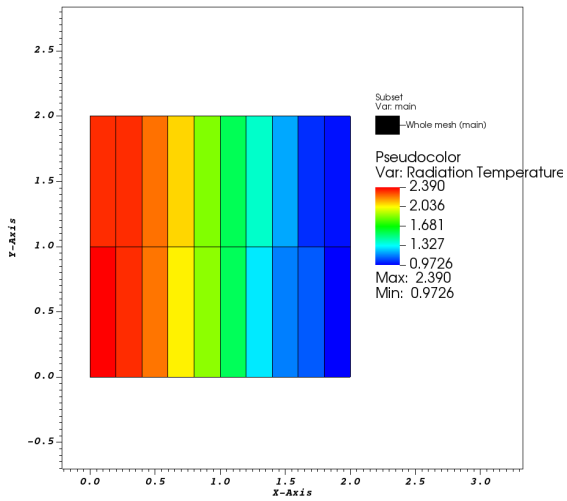

Figure 4.29: The DAIMC radiation temperatures after 100 time steps for the 2D hot and cold zone problem.

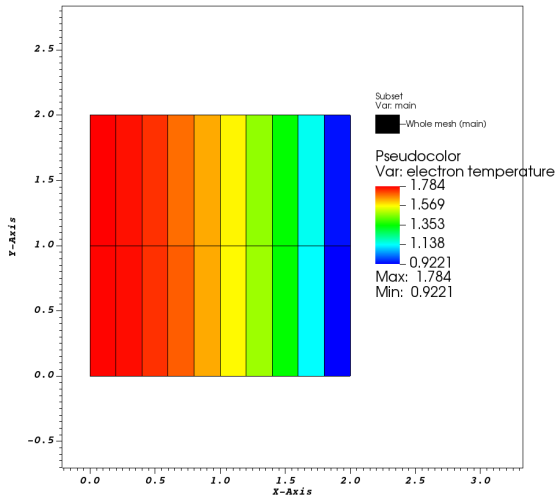

Figure 4.30: The DAIMC material temperatures after 500 time steps for the 2D hot and cold zone problem.

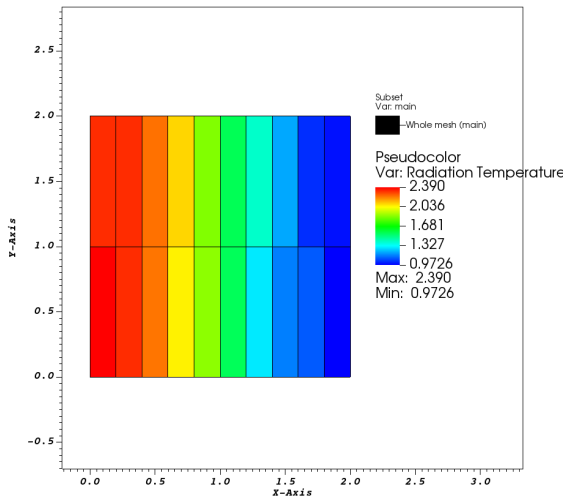

Figure 4.31: The IMC radiation temperatures after 500 time steps for the 2D hot and cold zone problem.

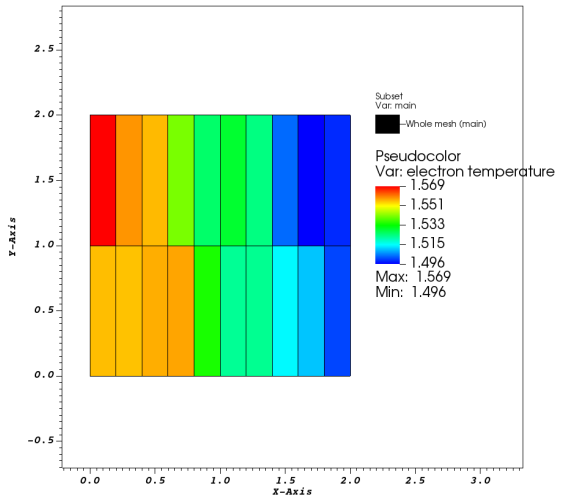

Figure 4.32: The DAIMC material temperatures at equilibrium.

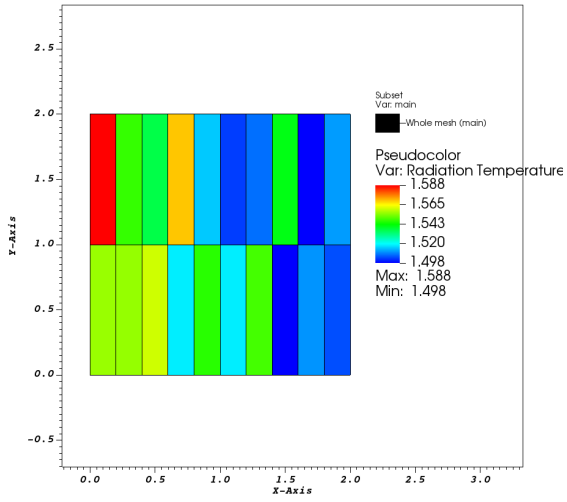

Figure 4.33: The DAIMC radiation temperatures at equilibrium.

The analytic temperature obtained from Eq. (4.9) is 1.531 keV. Figure 4.26 shows the initial material temperature and Figure 4.27 shows the initial radiation temperature. The hot material is expected to emit radiation and heat up the cold zones, which is observed in Figures 4.28 - 4.33. Once in equilibrium, the DAIMC results oscillate around the analytic value of 1.531 keV, as shown in Figure 4.32 and Figure 4.33.

4.3.4 Hot Corner

This test problem illustrates a material with an initial hot corner. A square of length 1.0 cm is divided into 100 equally spaced zones with 16 zones starting at an initial 'hot' temperature of 4.3 keV and the 'cold' zones have an initial temperature of 0.001 keV. The problem specifications used $\sigma = 2.0$ cm^{-1}, $\rho = 0.4$, $\kappa = 5.0$, $c_v = 0.1$, 10k particles per time step, $\Delta t = 1 \cdot 10^{-4}$ sh, 4000 total steps were simulated. A total of 5 outer (material temperature solve) and inner (radiation solve) iterations were used with DAIMC. The results from DAIMC and IMC are given below. The analytic equilibrium temperature is calculated to be $T = 0.633$ KeV.

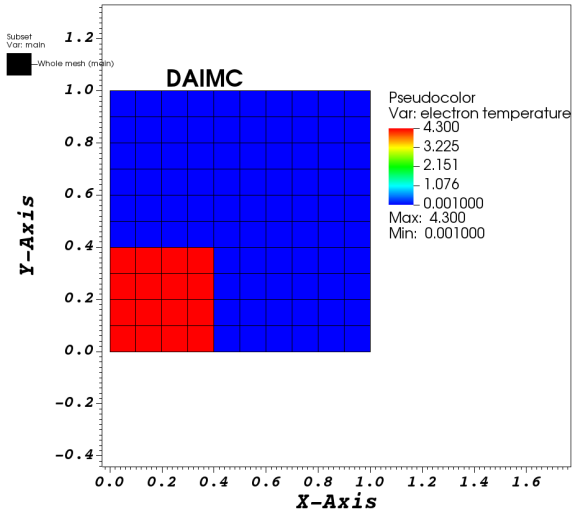

Figure 4.34: The initial DAIMC material temperatures.

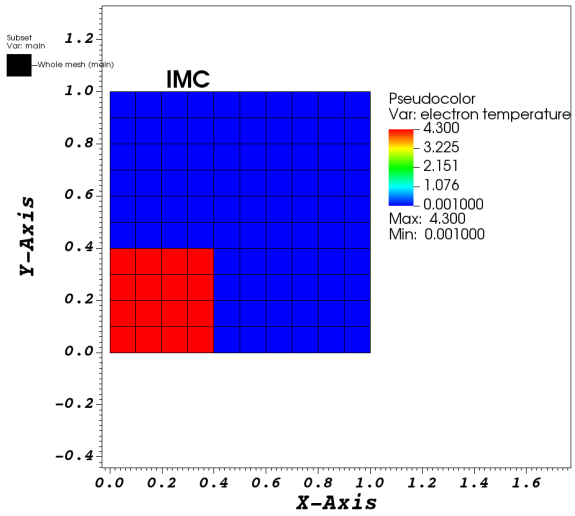

Figure 4.35: The initial IMC material temperatures.

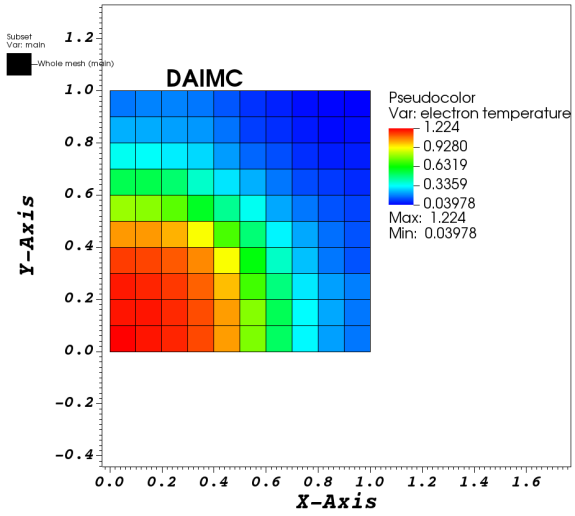

Figure 4.36: The DAIMC material temperatures after 50 time steps.

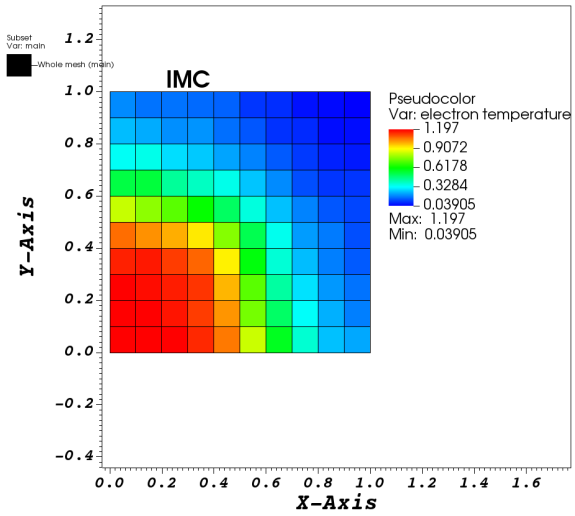

Figure 4.37: The IMC material temperatures after 50 time steps.

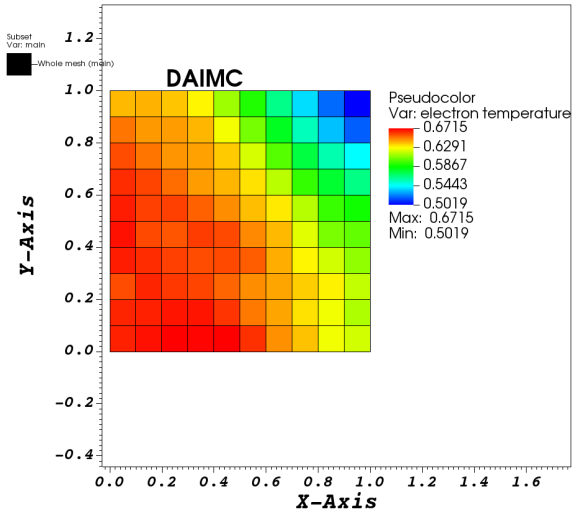

Figure 4.38: The DAIMC material temperatures after 400 time steps.

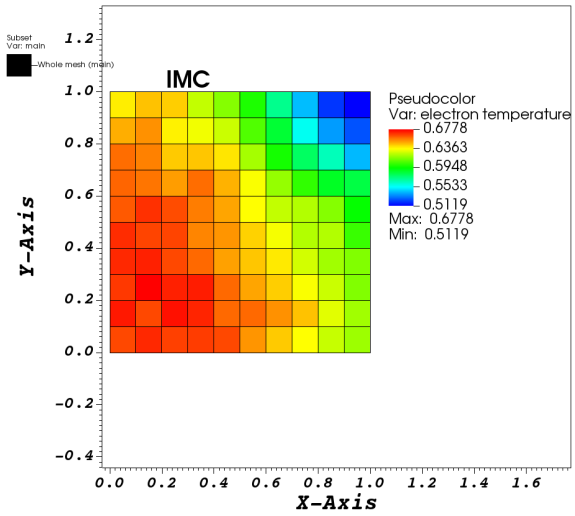

Figure 4.39: The IMC material temperatures after 400 time steps.

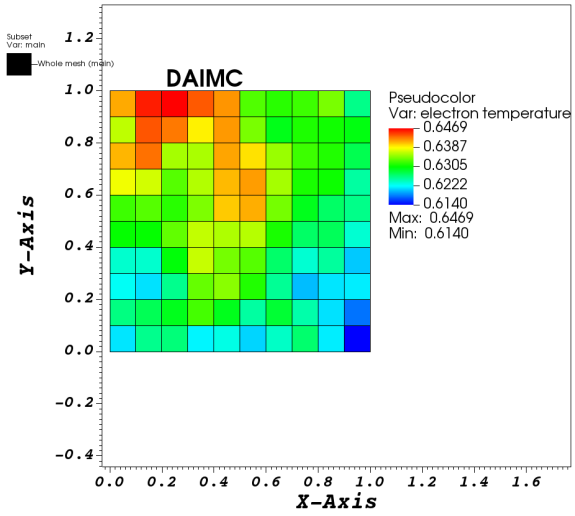

Figure 4.40: The final DAIMC material temperatures.

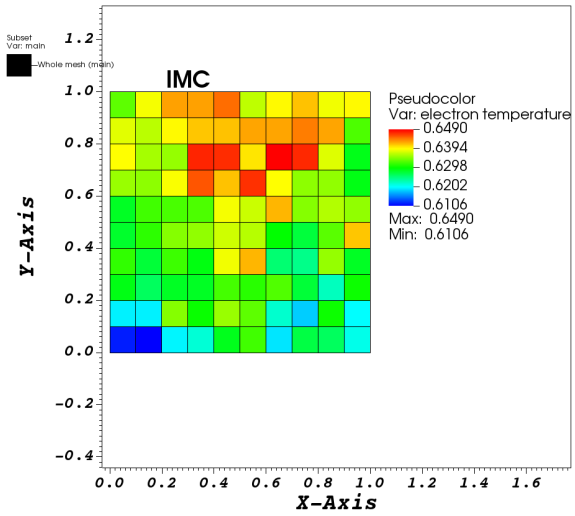

Figure 4.41: The final IMC material temperatures.

The analytic temperature obtained from Eq. (4.9) is $T = 0.633$ keV. Figures 4.34 and 4.35 shows the initial material temperatures for DAIMC and IMC, respectively. Temperatures after 50 and 400 time steps for both methods are shown in Figures 4.36 - 4.39. After 400 time steps, both methods reach the equilibrium temperature as shown in Figures 4.40 and 4.41.

4.3.5 Crooked Pipe

In this section, results for a modified crooked pipe problem are shown. This problem illustrates the radiation flow in a crooked pipe for an optically thick and optically thin material. The optically thick material has a density of $\rho = 10.0$ and the optically thin material has a density of $\rho = 0.01$. The opacity in the thick material region is $\sigma = 200.0$ and the opacity for the thin region is $\sigma = 0.2$. The time step size is $\Delta t = 1.0 \cdot 10^{-4}$ sh and a total of 1000 time steps were simulated. The DAIMC used 1 inner and 1 outer iteration. The pipe is modeled with a portion of the zones starting at a 'hot' temperature of $T = 3.0$ keV and the cold zones have a temperature of $T = 0.05$ keV. A total of 2520 zones were used to model the crooked pipe.

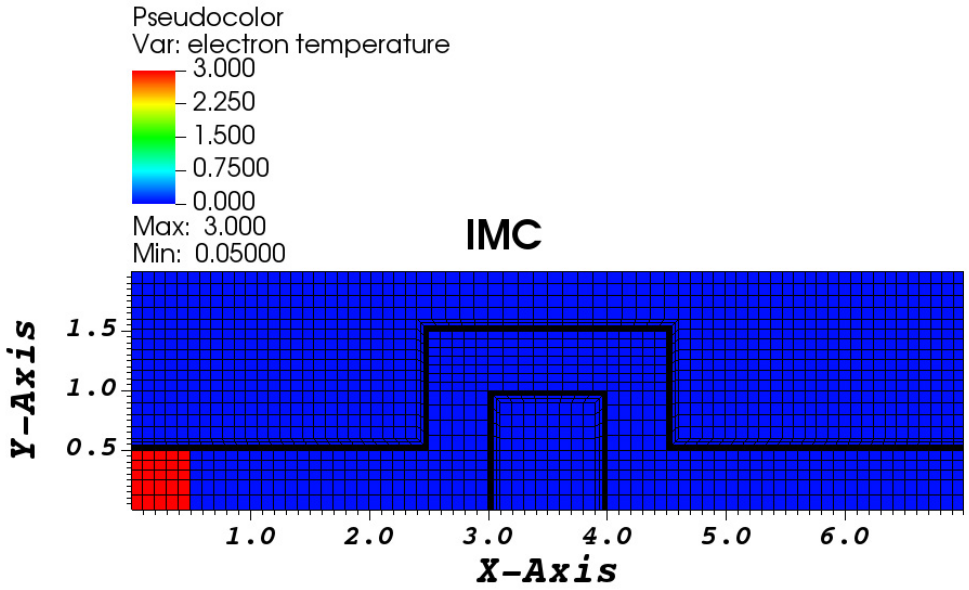

Figure 4.42: The initial IMC material temperatures for the crooked pipe problem.

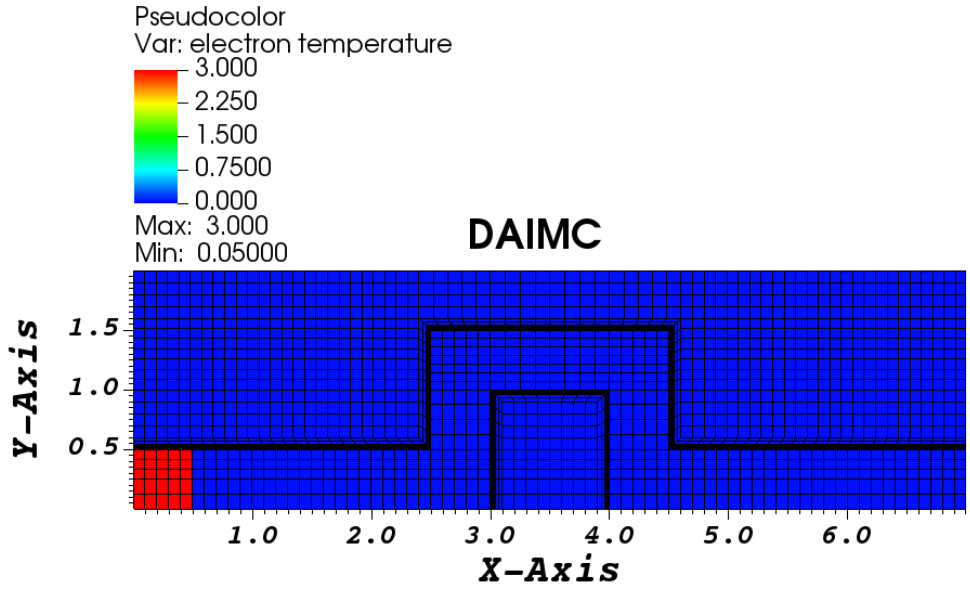

Figure 4.43: The initial DAIMC material temperatures for the crooked pipe problem.

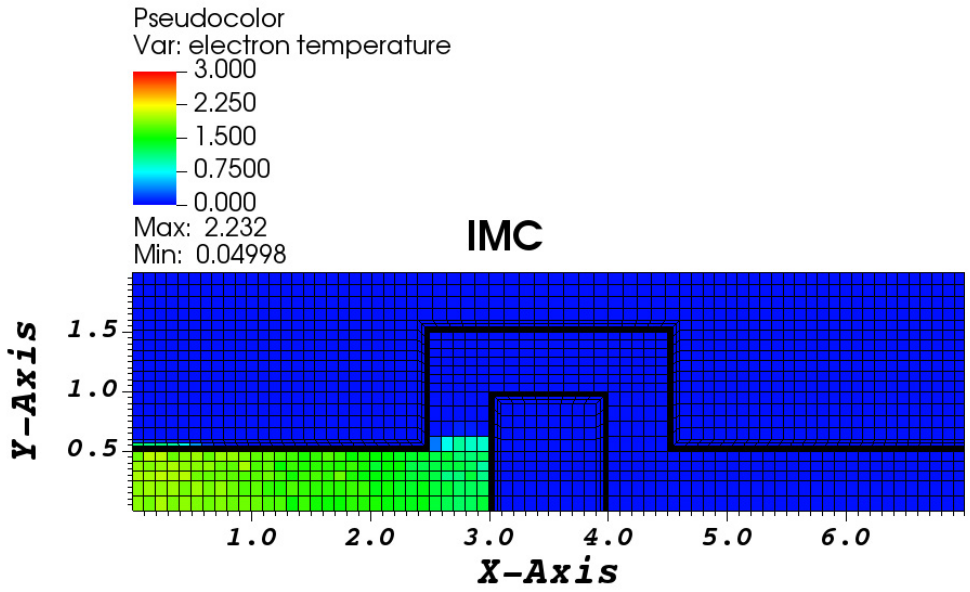

Figure 4.44: The IMC material temperatures after 100 time steps for the crooked pipe problem.

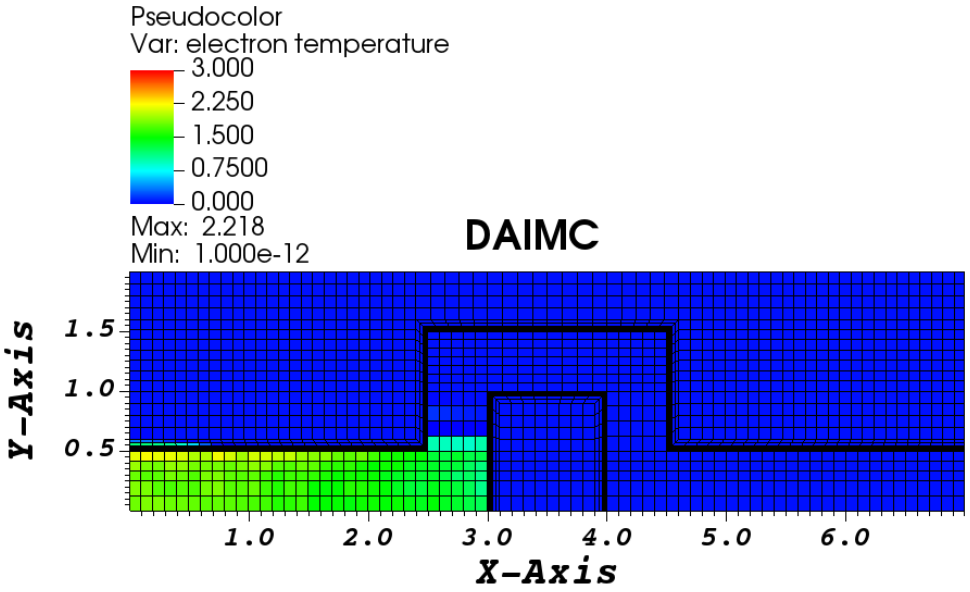

Figure 4.45: The DAIMC material temperatures after 100 time steps for the crooked pipe problem.

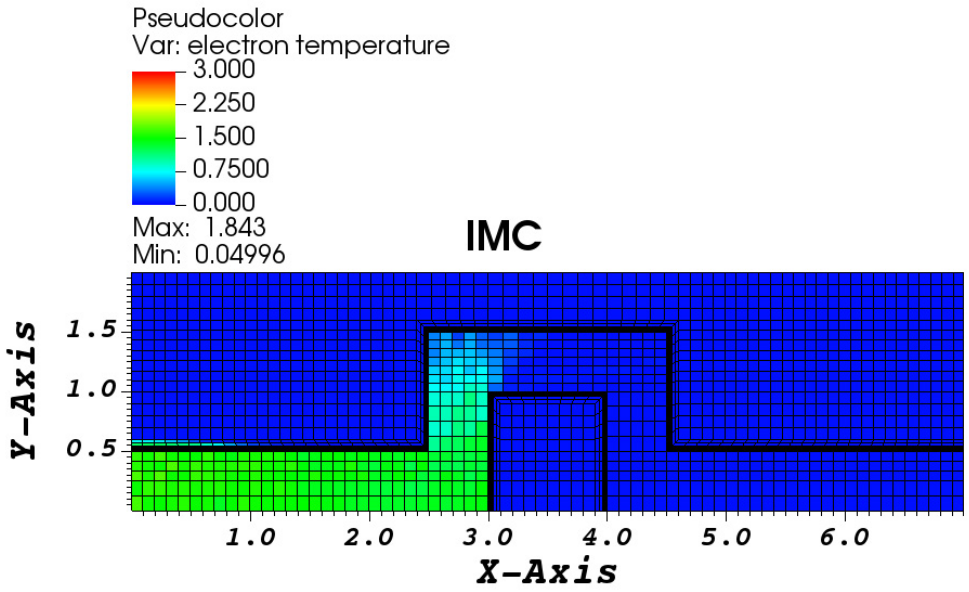

Figure 4.46: The IMC material temperatures after 200 time steps for the crooked pipe problem.

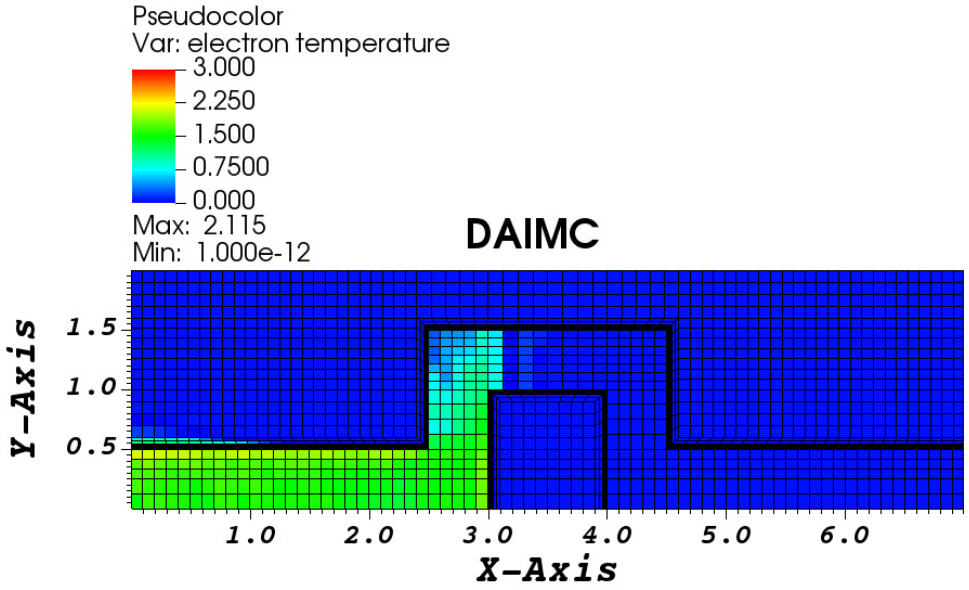

Figure 4.47: The DAIMC material temperatures after 200 time steps for the crooked pipe problem.

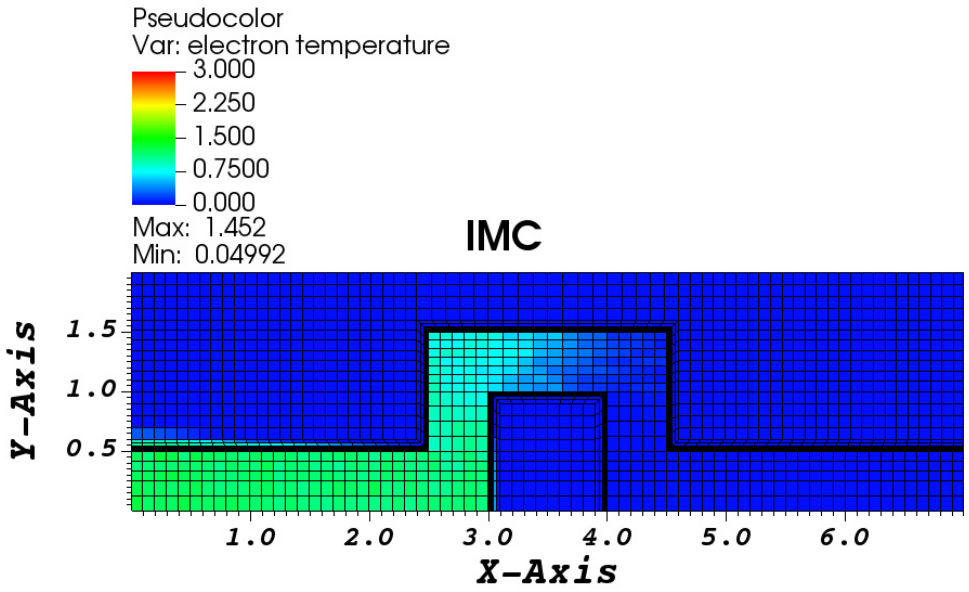

Figure 4.48: The IMC material temperatures after 500 time steps for the crooked pipe problem.

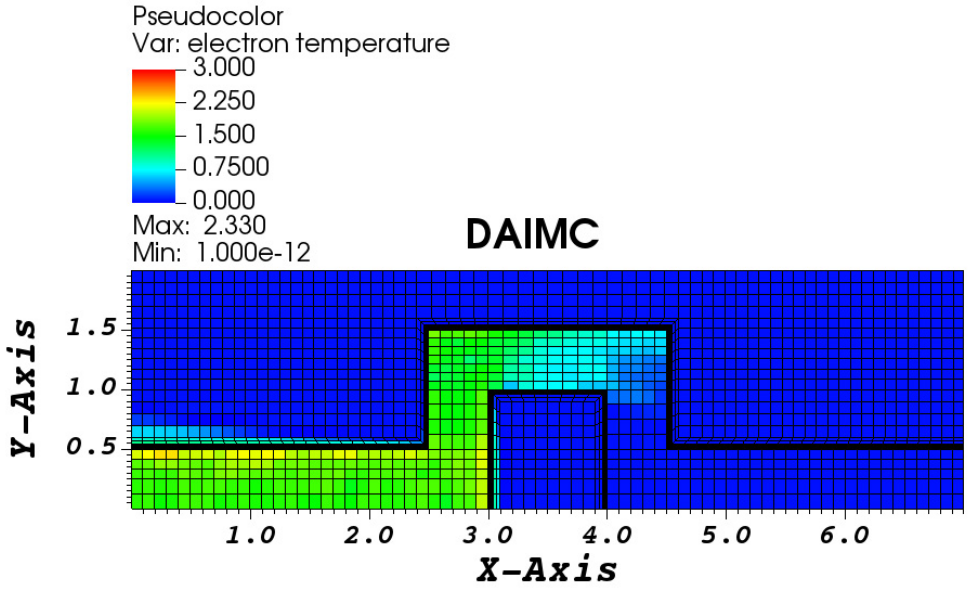

Figure 4.49: The DAIMC material temperatures after 500 time steps for the crooked pipe problem.

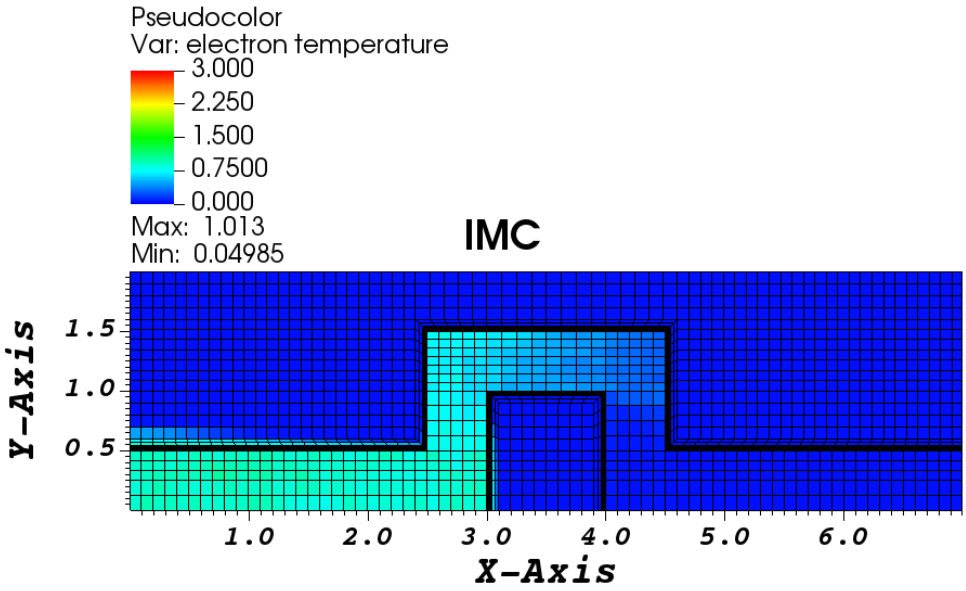

Figure 4.50: The IMC material temperatures after 1000 time steps for the crooked pipe problem.

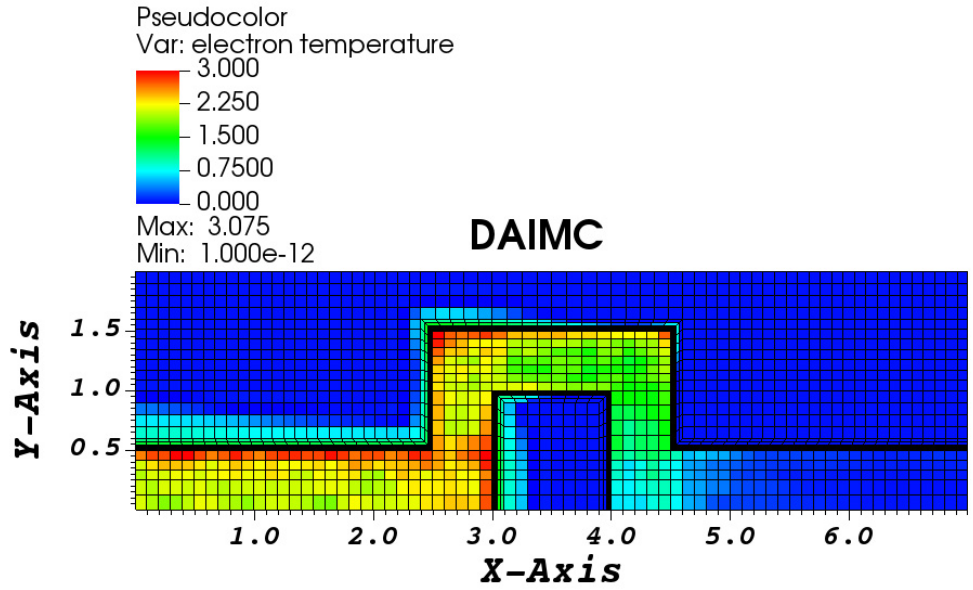

Figure 4.51: The DAIMC material temperatures after 1000 time steps for the crooked pipe problem.

Figures 4.42 and 4.43 show the initial material temperatures for this problem. The radiation travels along the pipe in the thin material and the material temperatures after 100 time steps are shown in Figures 4.44 and 4.45 for the DAIMC and IMC method, respectively. After 500 time steps, the radiation has made it farther along the pipe for DAIMC than IMC, as shown in Figures 4.48 and 4.49. The temperatures after 1000 time steps are shown in Figures 4.50 and 4.51.

4.3.5.1 Crooked Pipe Mesh Refinement

This section provides results for the crooked pipe problem using the same problem specifications as the previous section except the pipe is divided into 9904 zones instead of the 2520 used previously.

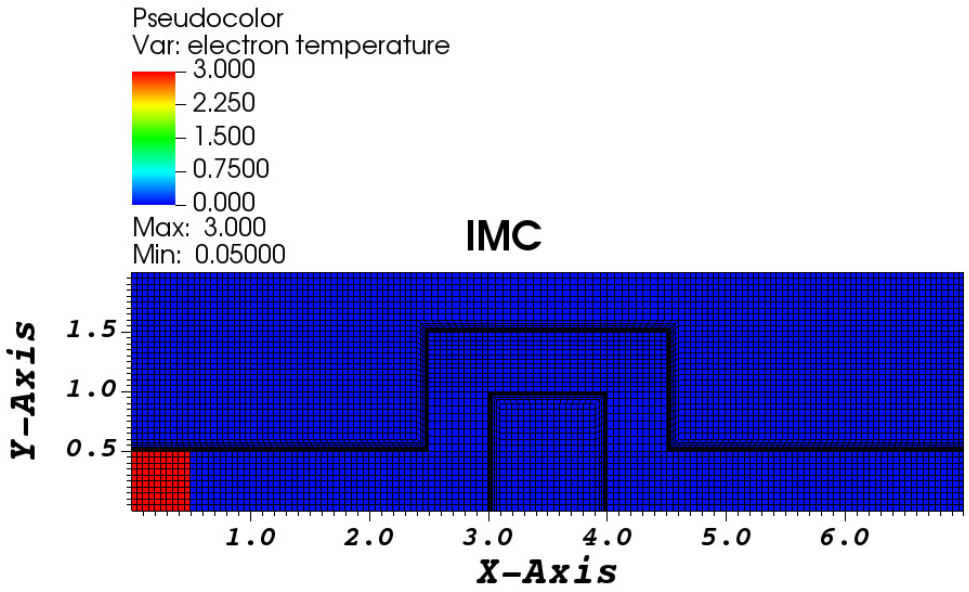

Figure 4.52: The initial IMC material temperatures for the refined crooked pipe problem.

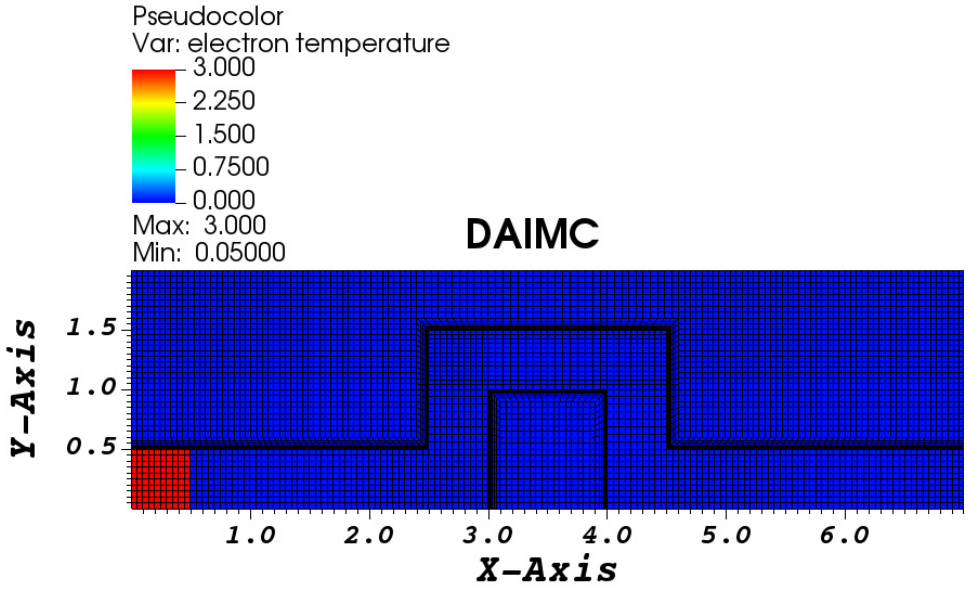

Figure 4.53: The initial DAIMC material temperatures for the refined crooked pipe problem.

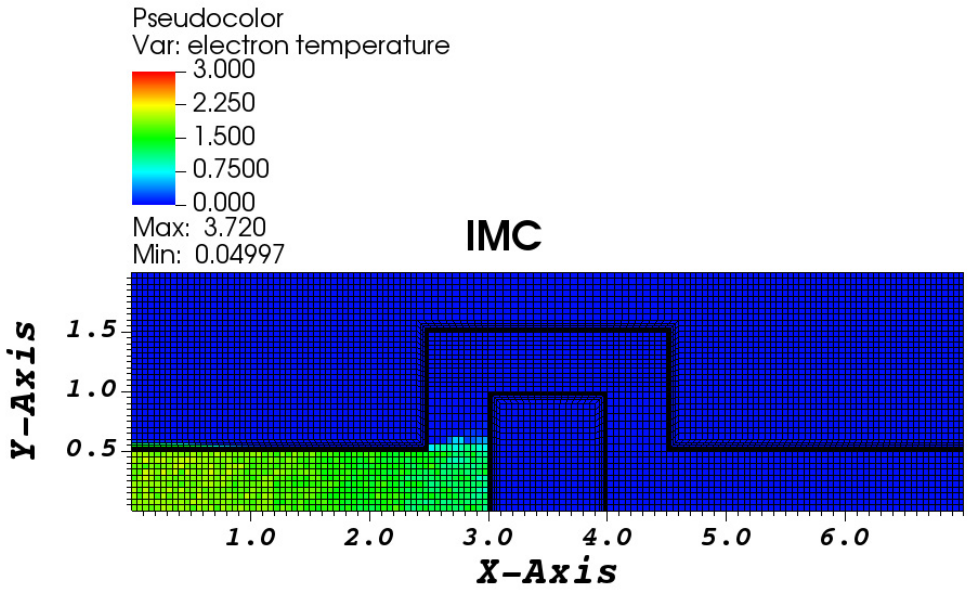

Figure 4.54: The IMC material temperatures after 100 time steps for the refined crooked pipe problem.

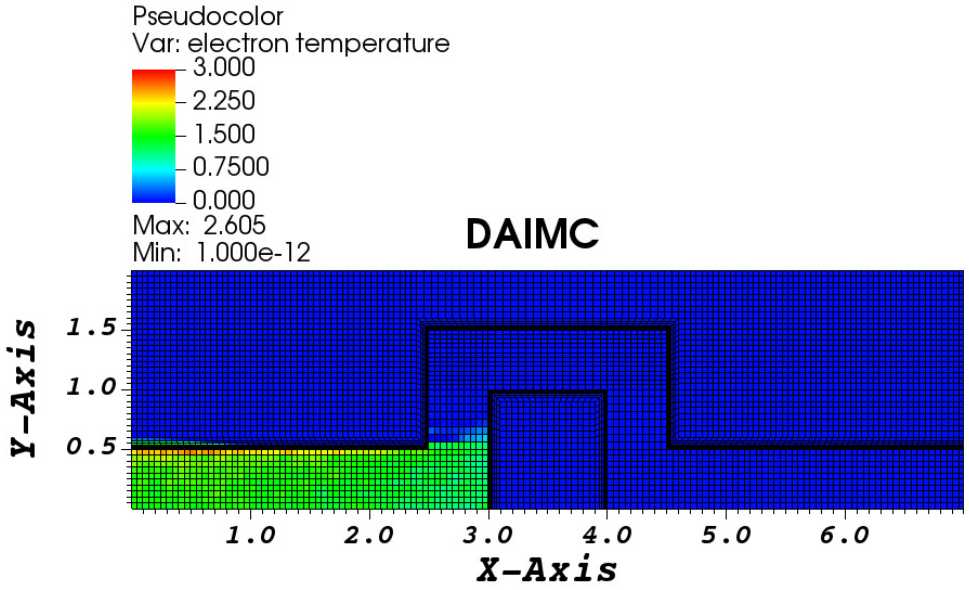

Figure 4.55: The DAIMC material temperatures after 100 time steps for the refined crooked pipe problem.

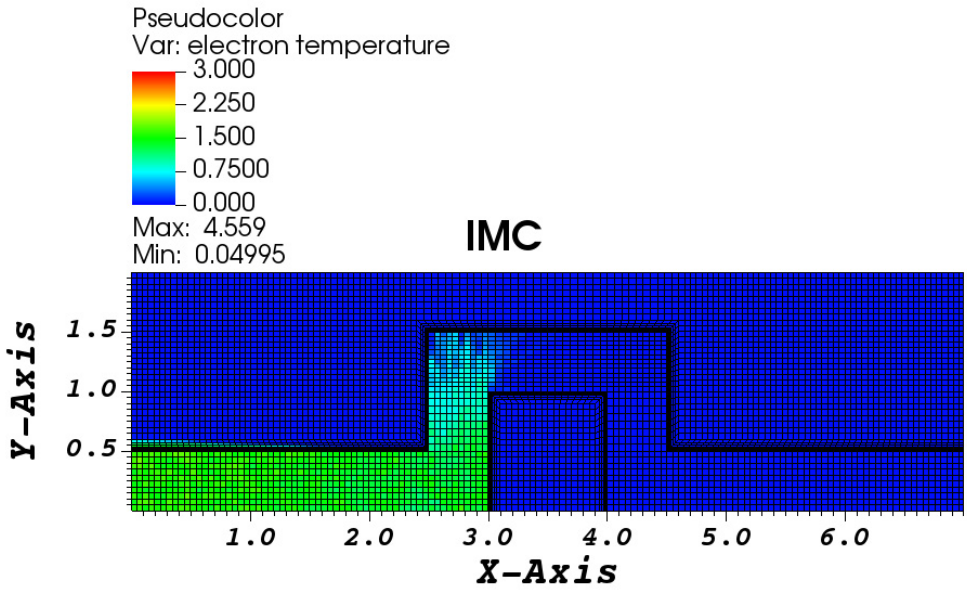

Figure 4.56: The IMC material temperatures after 200 time steps for the refined crooked pipe problem.

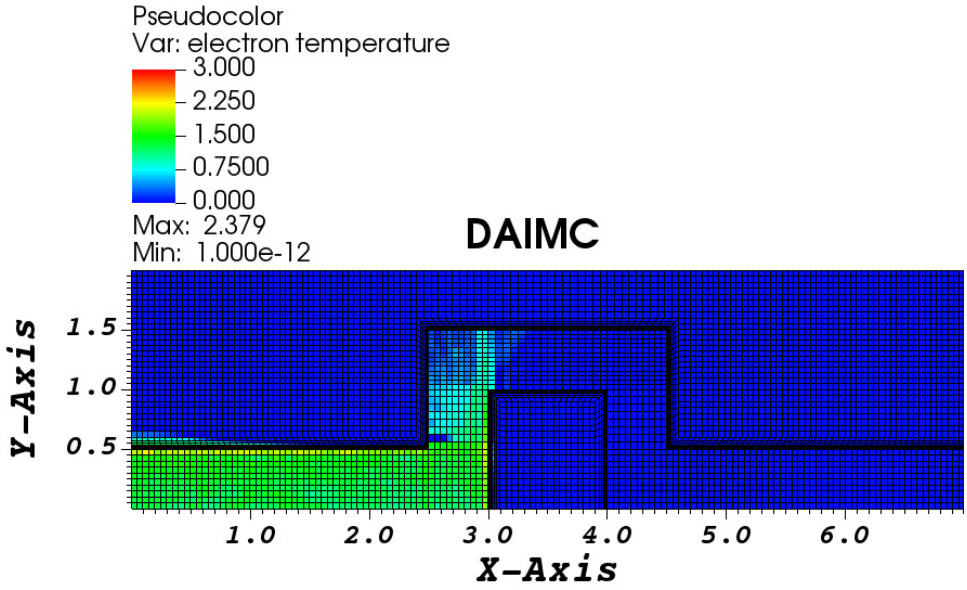

Figure 4.57: The DAIMC material temperatures after 200 time steps for the refined crooked pipe problem.

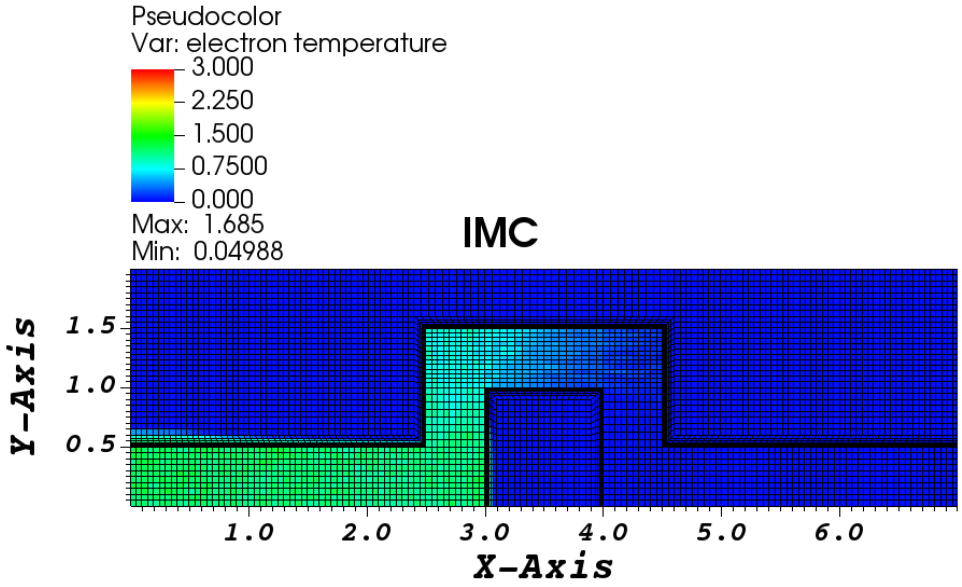

Figure 4.58: The IMC material temperatures after 500 time steps for the refined crooked pipe problem.

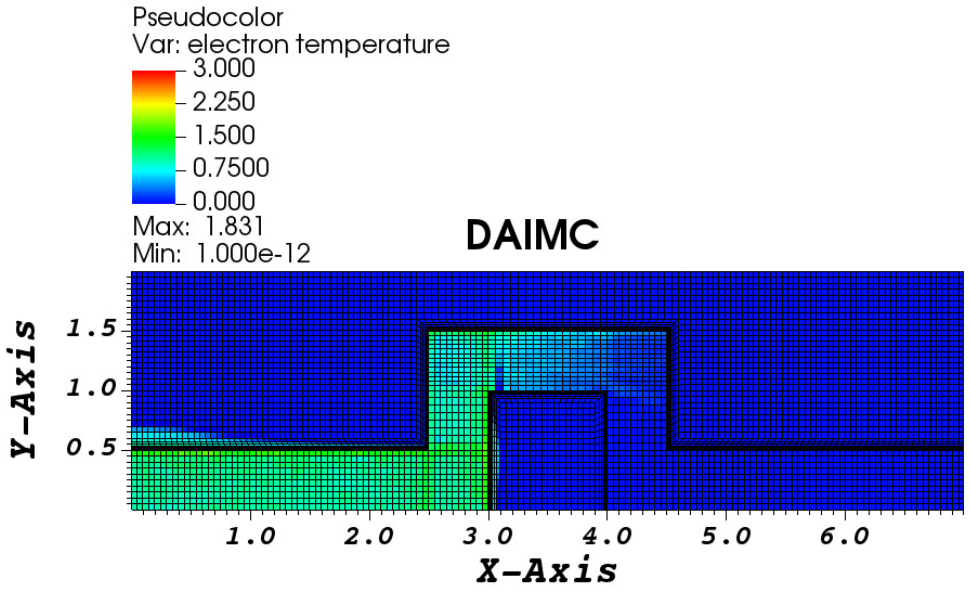

Figure 4.59: The DAIMC material temperatures after 500 time steps for the refined crooked pipe problem.

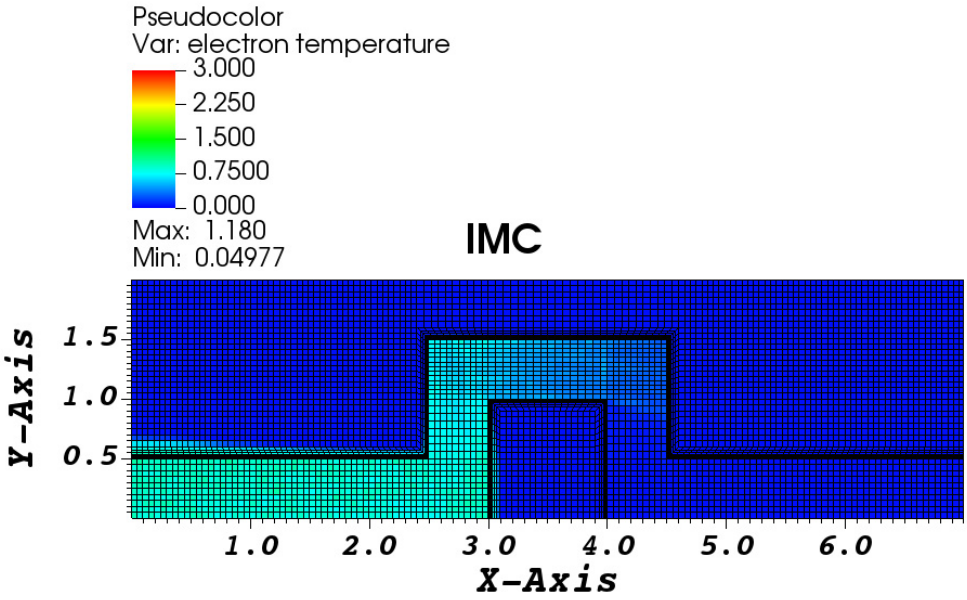

Figure 4.60: The IMC material temperatures after 1000 time steps for the refined crooked pipe problem.

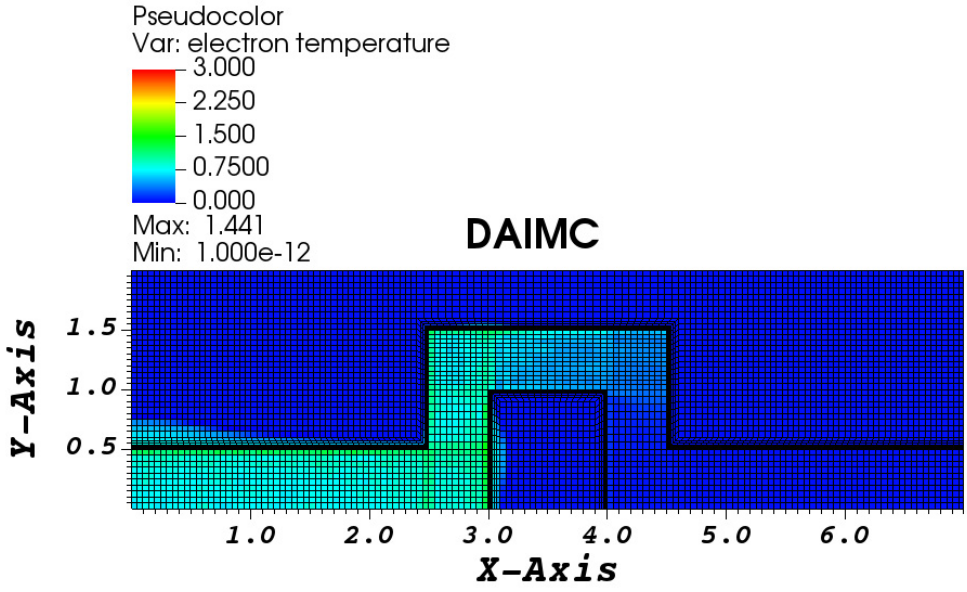

Figure 4.61: The DAIMC material temperatures after 1000 time steps for the refined crooked pipe problem.

Figures 4.52 and 4.53 show the initial material temperatures for the crooked pipe problem with mesh refinement. The radiation travels along the pipe in the thin material and the material temperatures after 100 time steps are shown in Figures 4.54 and 4.55 for the DAIMC and IMC method, respectively. After 500 time steps, the temperatures are given in Figures 4.58 and 4.59. The temperatures after 1000 time steps are shown in Figures 4.60 and 4.61.

4.3.6 Temperature Dependent Opacity

The previous section highlights test cases for multiple zones in 2D-XY geometry using a constant opacity treatment. We now provide a study for the behavior of DAIMC when the opacity is modeled by

$$\sigma = \rho\kappa T^{-n}, \quad n = 1, 2, \tag{4.11}$$

where T is the temperature of the material. The following test problems use $\rho = 0.005$, $\kappa = 10.0$, $c_v = 0.1$. The material has an initial temperature of $T_m = 0.001$ and the radiation field has an initial temperature of $T_r = 0.3$. The analytic solution is modeled by

$$\frac{\mathrm{d}E}{\mathrm{d}t} = c\sigma(aT^4 - E), \tag{4.12}$$

and

$$\frac{\mathrm{d}T_m}{\mathrm{d}t} = \frac{-c\sigma}{\rho c_v}(aT^4 - E), \tag{4.13}$$

with the opacity prescribed by Eq. (4.11).

4.3.6.1 T^{-1}

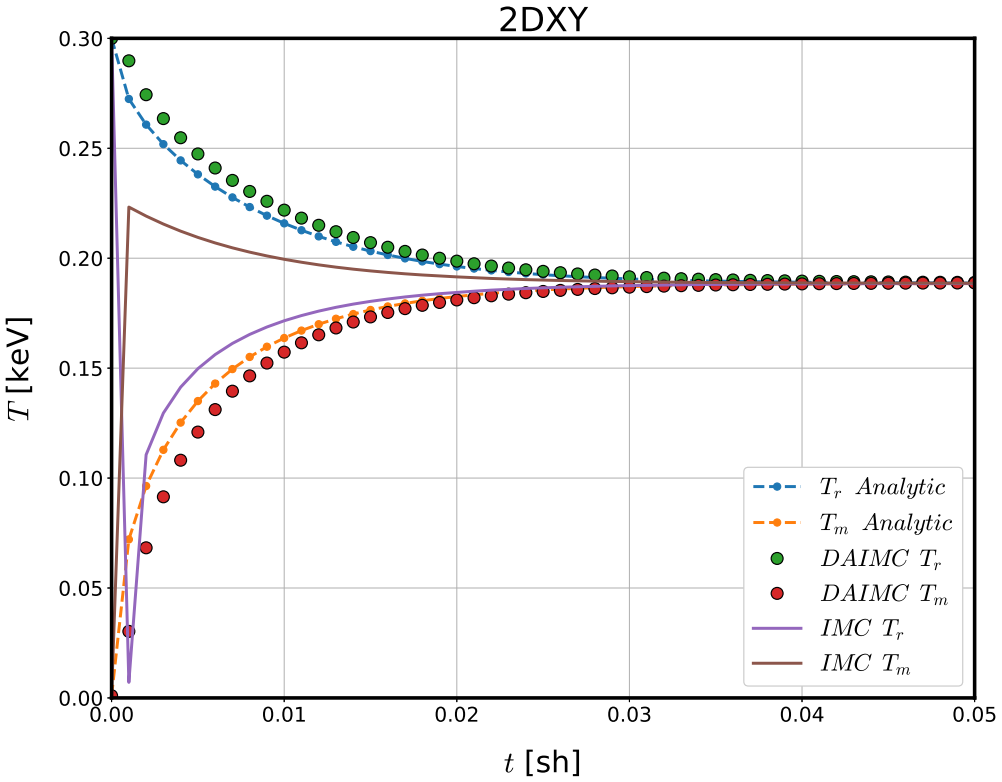

Figure 4.62: DAIMC and IMC temperatures for a single zone in 2D with T^{-1} opacity using $\Delta t = 1.0 \cdot 10^{-3}$ sh.

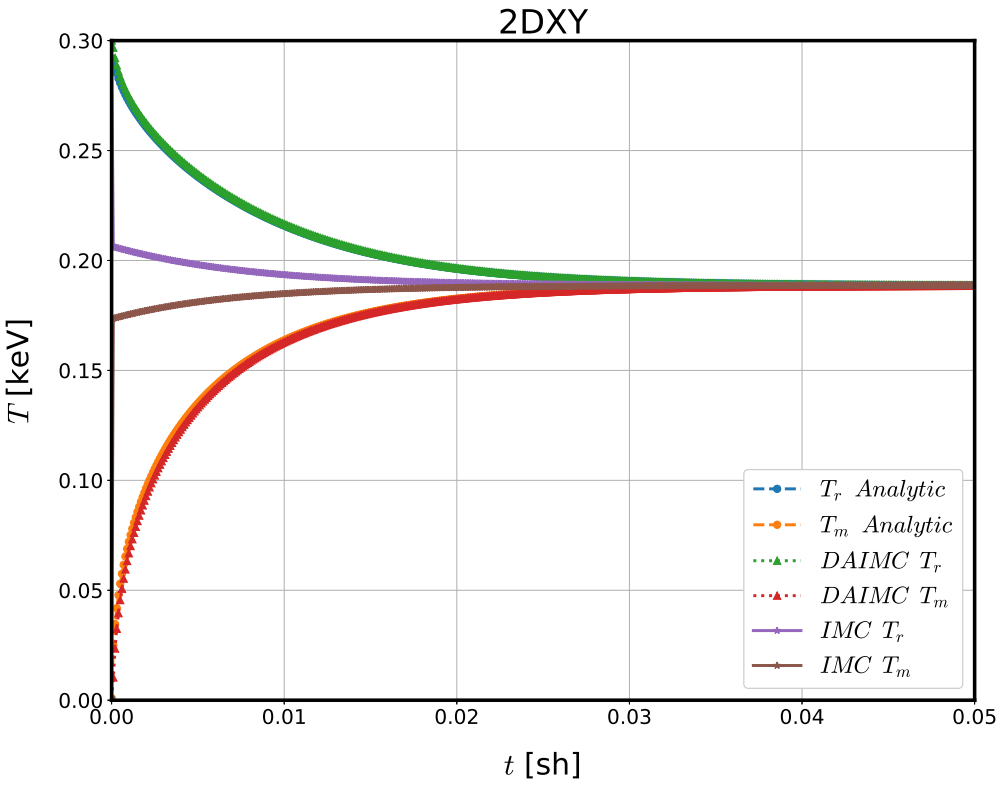

Figure 4.63: DAIMC and IMC temperatures for a single zone in 2D with T^{-1} opacity using $\Delta t = 1.0 \cdot 10^{-4}$ sh.

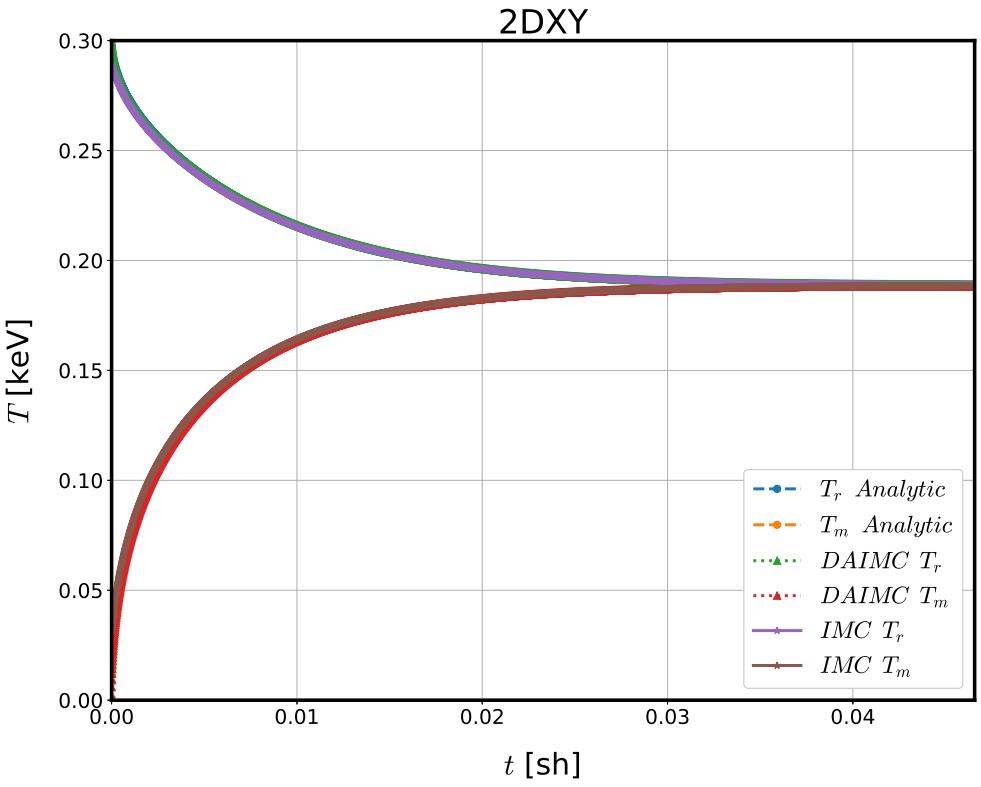

Figure 4.64: DAIMC and IMC temperatures for a single zone in 2D with T^{-1} opacity using $\Delta t = 1.0 \cdot 10^{-5}$ sh.

Δt [sh]	Method	Variable	ℓ_2-error	ℓ_∞-error
$1.0 \cdot 10^{-3}$	DAIMC	Material temp.	$6.222 \cdot 10^{-4}$	$4.182 \cdot 10^{-2}$
		Radiation temp.	$3.484 \cdot 10^{-4}$	$1.733 \cdot 10^{-2}$
	IMC	Material temp.	$2.737 \cdot 10^{-3}$	$1.511 \cdot 10^{-1}$
		Radiation temp.	$3.809 \cdot 10^{-3}$	$2.653 \cdot 10^{-1}$
$1.0 \cdot 10^{-4}$	DAIMC	Material temp.	$6.870 \cdot 10^{-5}$	$1.456 \cdot 10^{-2}$
		Radiation temp.	$3.344 \cdot 10^{-5}$	$5.209 \cdot 10^{-3}$
	IMC	Material temp.	$1.280 \cdot 10^{-3}$	$1.487 \cdot 10^{-1}$
		Radiation temp.	$9.638 \cdot 10^{-4}$	$8.534 \cdot 10^{-2}$
$1.0 \cdot 10^{-5}$	DAIMC	Material temp.	$2.424 \cdot 10^{-6}$	$2.177 \cdot 10^{-3}$
		Radiation temp.	$1.163 \cdot 10^{-6}$	$7.503 \cdot 10^{-4}$
	IMC	Material temp.	$2.366 \cdot 10^{-5}$	$2.380 \cdot 10^{-2}$
		Radiation temp.	$1.087 \cdot 10^{-5}$	$8.595 \cdot 10^{-3}$

Table 4.5: The norms for IMC and DAIMC using a single zone in 2D with T^{-1} opacity for different Δt sizes.

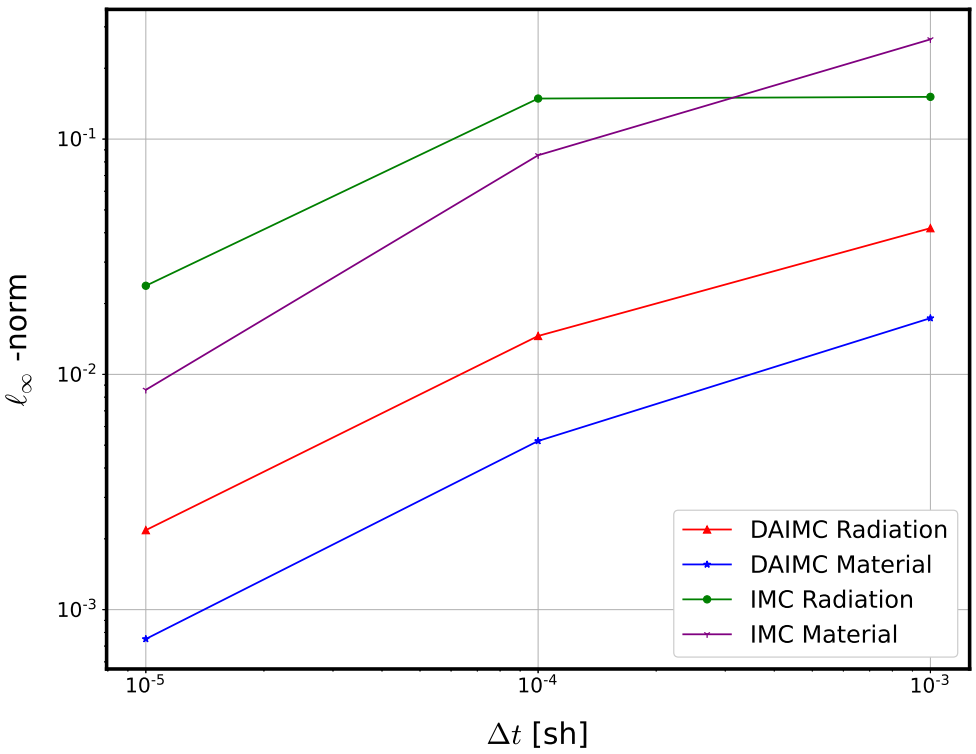

Figure 4.65: The ℓ_∞-norm of the error for a single zone in 2D with T^{-1} opacity.

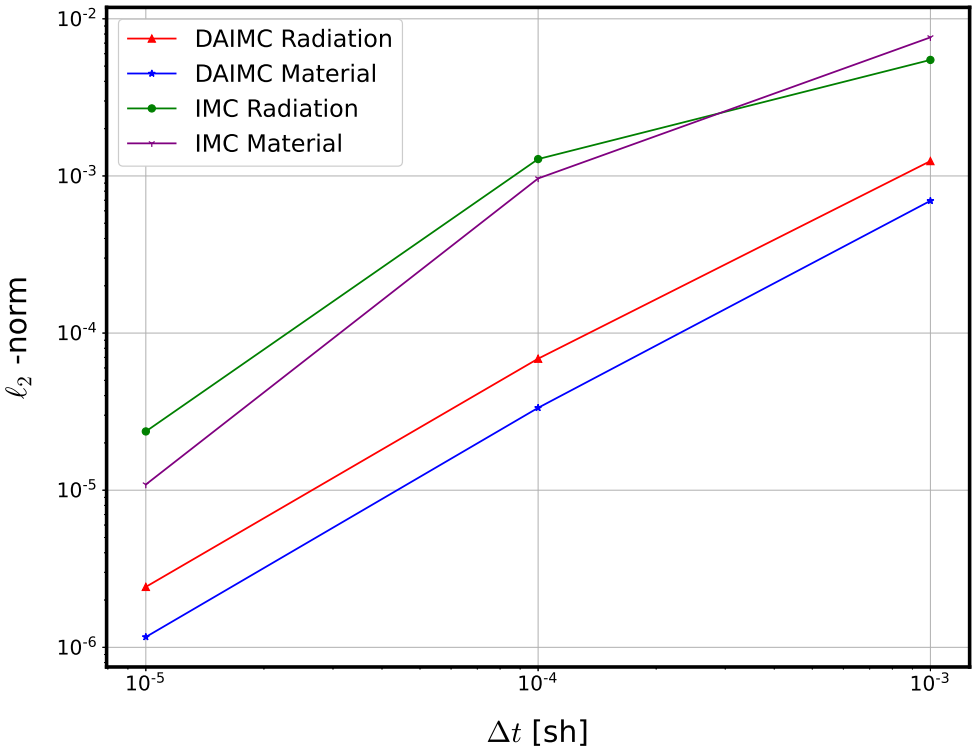

Figure 4.66: The ℓ_2-norm of the error for a single zone in 2D with T^{-1} opacity.

When the opacity varies as T^{-1}, DAIMC converges to the correct equilibrium solution, as shown in Figures 4.62, 4.63, and 4.64. In Figures 4.62 and 4.63, the IMC method exhibits an overheating behavior where the material temperature exceeds the driving temperature of the radiation field. The overheating of the material can be resolved using a $\Delta t = 1.0 \cdot 10^{-5}$ sh or smaller, as illustrated in Figure 4.64. DAIMC does not exhibit the overheating behavior since more Newton steps are taken within a single time step as opposed to IMC's single Newton step.

As the time step size decreases, it is expected that the results from DAIMC and IMC converges to the analytic solution. This can be confirmed by the decreasing l_2-norm and infinity-norm in Table 4.6.

4.3.6.2 T^{-2}

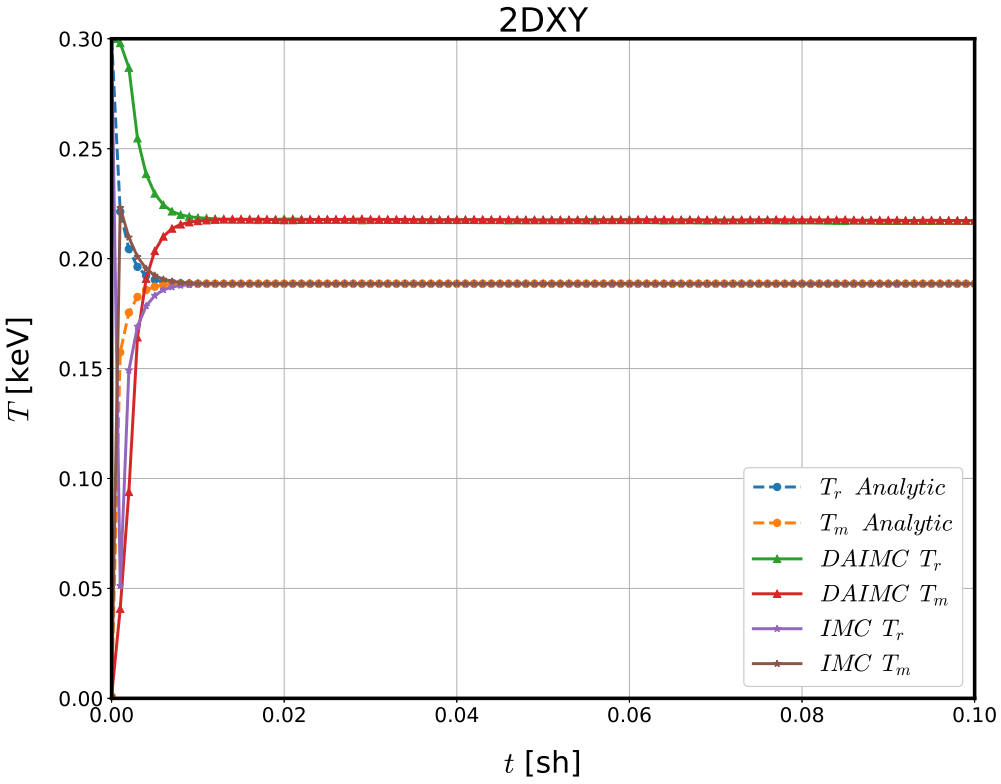

Figure 4.67: The time evolution of the temperatures using DAIMC and IMC for a single zone in 2D with T^{-2} temperature dependent opacity with $\Delta t = 1.0 \cdot 10^{-3}$ sh.

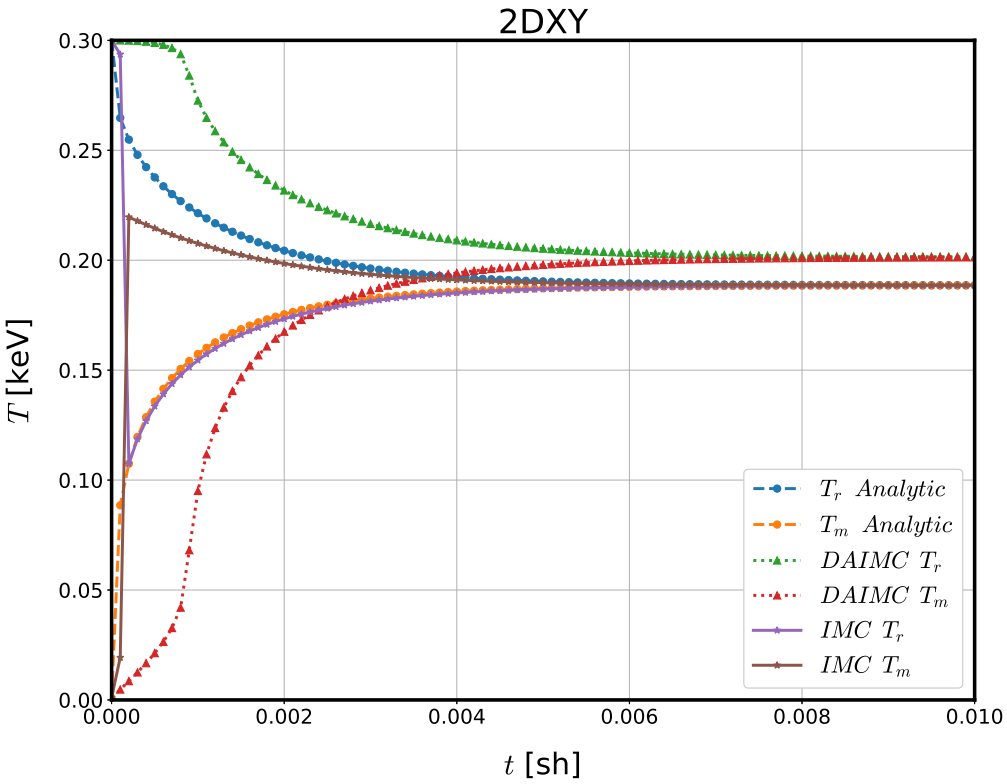

Figure 4.68: The time evolution of the temperatures using DAIMC and IMC for a single zone in 2D with T^{-2} temperature dependent opacity with $\Delta t = 1.0 \cdot 10^{-4}$ sh.

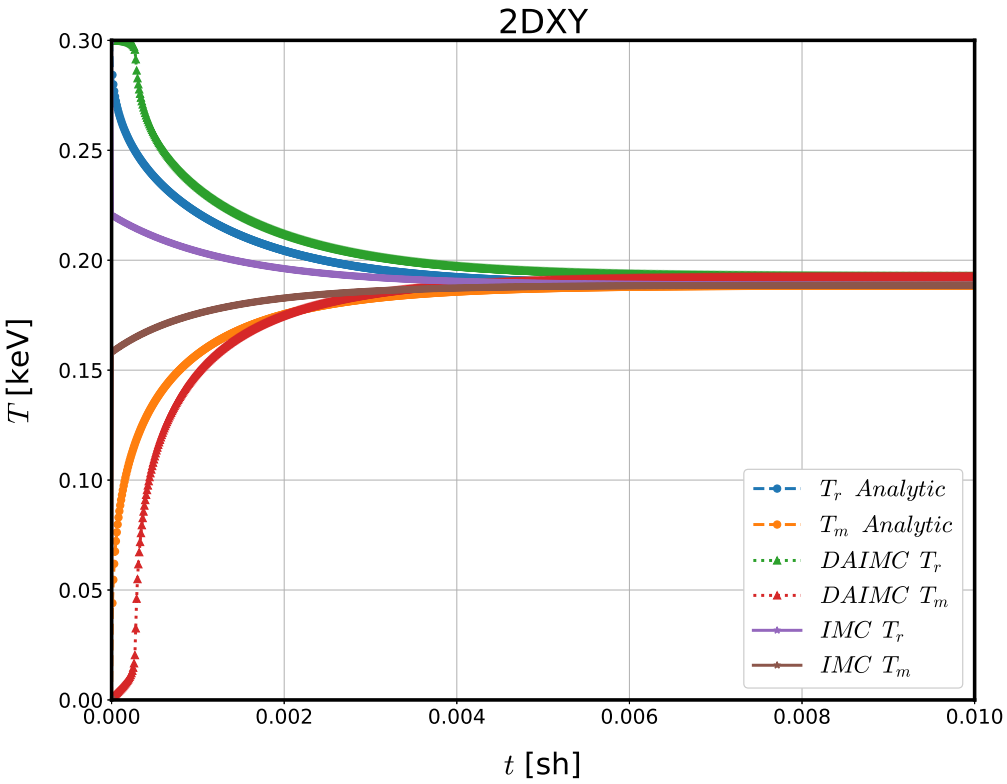

Figure 4.69: The time evolution of the temperatures using DAIMC and IMC for a single zone in 2D with T^{-2} temperature dependent opacity with $\Delta t = 1.0 \cdot 10^{-5}$ sh.

Δt [sh]	Method	Variable	ℓ_2-error	ℓ_∞-error
$1.0 \cdot 10^{-3}$	DAIMC	Material temp.	$3.134 \cdot 10^{-3}$	$1.165 \cdot 10^{-1}$
		Radiation temp.	$3.133 \cdot 10^{-3}$	$8.251 \cdot 10^{-2}$
	IMC	Material temp.	$7.642 \cdot 10^{-4}$	$6.573 \cdot 10^{-2}$
		Radiation temp.	$1.798 \cdot 10^{-3}$	$1.701 \cdot 10^{-1}$
$1.0 \cdot 10^{-4}$	DAIMC	Material temp.	$3.416 \cdot 10^{-3}$	$1.150 \cdot 10^{-1}$
		Radiation temp.	$2.518 \cdot 10^{-3}$	$6.684 \cdot 10^{-2}$
	IMC	Material temp.	$2.699 \cdot 10^{-3}$	$1.121 \cdot 10^{-1}$
		Radiation temp.	$3.469 \cdot 10^{-3}$	$1.474 \cdot 10^{-1}$
$1.0 \cdot 10^{-5}$	DAIMC	Material temp.	$5.191 \cdot 10^{-4}$	$9.956 \cdot 10^{-2}$
		Radiation temp.	$3.058 \cdot 10^{-4}$	$4.659 \cdot 10^{-2}$
	IMC	Material temp.	$4.726 \cdot 10^{-4}$	$1.145 \cdot 10^{-1}$
		Radiation temp.	$3.471 \cdot 10^{-4}$	$6.390 \cdot 10^{-2}$

Table 4.6: The norms for IMC and DAIMC using a single zone in 2D with T^{-2} temperature dependent opacity with various Δt sizes.

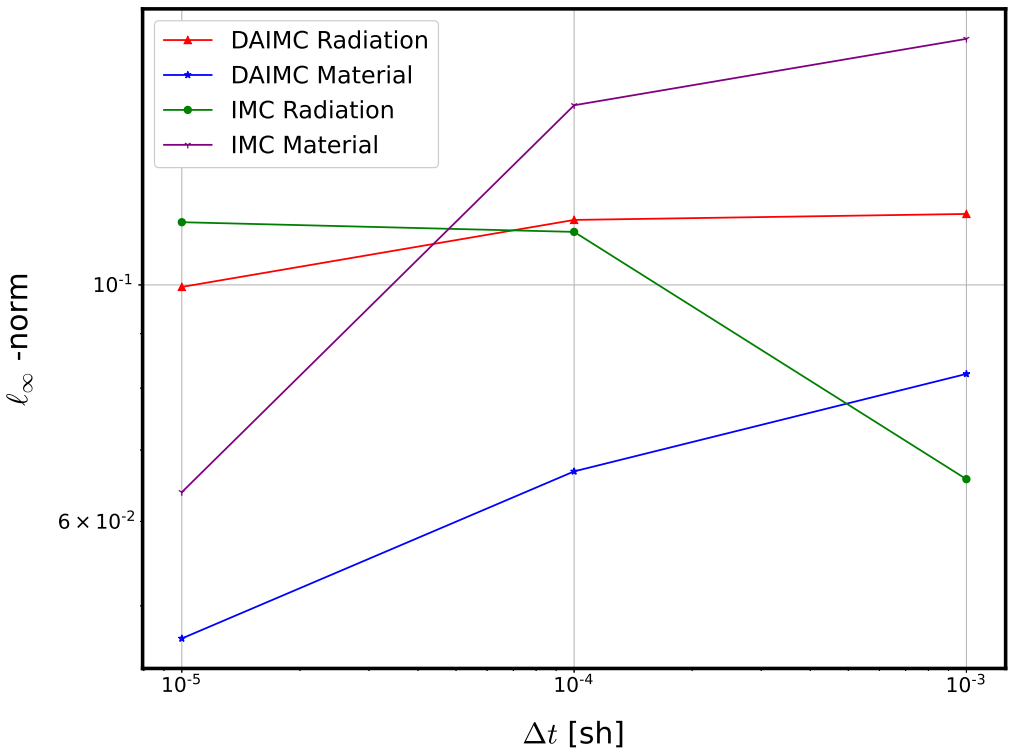

Figure 4.70: The ℓ_∞-norm of the error for a single zone in 2D with T^{-2} opacity.

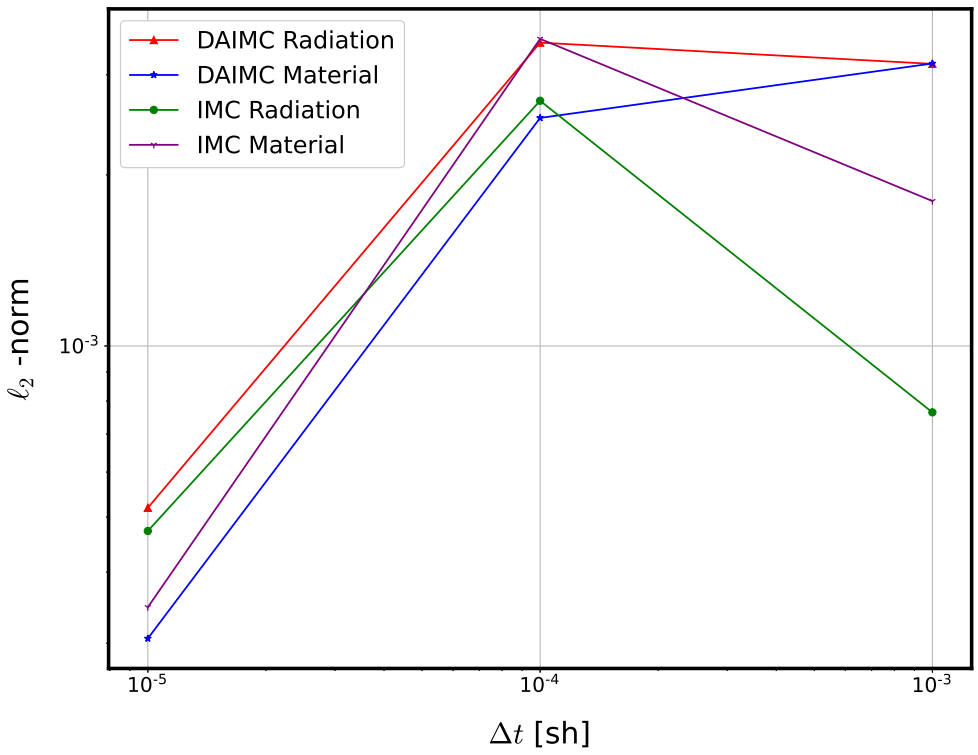

Figure 4.71: The ℓ_2-norm of the error for a single zone in 2D with T^{-2} opacity.

The results in Figure 4.67 shows the convergence of DAIMC and IMC for a given time step size of $\Delta t = 1.0 \cdot 10^{-3}$. DAIMC is observed to not converge to the expected analytic solution. While IMC converges to the analytic solution, overheating of the material can be observed. The converged equilibrium temperatures of DAIMC approaches the expected analytic value as the size of Δt decreases. This is observed in Figures 4.67-4.69. Table 4.6 shows the norms of both DAIMC and IMC for several different time step sizes.

4.4 Summary

In this chapter, results from DAIMC for a series of test problems in 1D and 2D-XY geometry were given. In 1D, QMC was introduced to the DAIMC method by sampling from the Sobol sequence rather than traditional pseudo-random numbers. The 1D and 2D-XY geometry results verify that DAIMC has been implemented correctly since the analytic solutions were recovered. Chapter 5 gives a discussion of these results and highlights the significance of the spatial discretizations used in DAIMC.

Chapter 5: Discussion

In this chapter, we discuss the significance of the results presented in Chapter 4. Section 5.1 gives a discussion of the results obtained from 1D calculations. Section 5.2 provides a discussion on the results from the 2D implementation of DAIMC.

5.1 1D Results

The simple test cases from Section 4.2 demonstrated the behavior of the DAIMC algorithm for problems involving constant opacity treatment in 1D slab geometry. When comparing the ℓ_2 and ℓ_∞-norms of the error, Table 4.1 shows that DAIMC yields closer results to the analytic solution than the IMC method. It was shown in Chapter 2 that the IMC method is a single Newton iteration. Since DAIMC uses several Newton steps, it is not surprising that the norms are smaller than those of IMC. However, this smaller norm comes with the trade-off of taking more Newton steps and requiring more transport solves.

Quasi-Monte Carlo (QMC) was introduced and implemented with DAIMC. Figures 4.8, 4.10, and 4.12 show that both the Monte Carlo (MC) and the QMC implementation of DAIMC converge to the correct equilibrium solution. Tables 4.2, 4.3, and 4.4 show that both the QMC and MC implementation of DAIMC yield results which have a smaller ℓ_2 and ℓ_∞-norms of the error when compared to the tradi-

tional IMC method. For optically thin problems, IMC has a faster run-time than the QMC and MC implementations of DAIMC as shown in Figure 4.9. As the opacity increases the MC implementation of DAIMC remains the slowest of the three methods as shown in Figures 4.11 and 4.13. In Figure 4.11, the QMC implementation is observed to have comparable run-time to that of the IMC method. For optically thicker problems, such as $\sigma = 13,000$, QMC has a faster run-time than IMC. On average, the QMC implementation of DAIMC requires half as many iterations as the MC implementation.

The Monte Carlo transport solver used a piecewise constant treatment for the temperature and opacity. Each zone in the Monte Carlo solver was then divided into two half-cells, as the linear discontinuous diffusion solver requires two unknowns per cell. The results show that a piecewise constant treatment for Monte Carlo transport and a linear-discontinuous discretization of the diffusion equation are compatible when using the DAIMC algorithm in 1D. For problems in which the time analytic solution can be modeled by Eq. 4.6 and Eq. 4.8, the DAIMC results yield more accurate solutions than IMC when comparing the l_2-norms of the error and infinity-norms.

5.2 2D-XY

The 2D-XY implementation of DAIMC uses a constant treatment of the opacity and temperature in the Monte Carlo transport solver. Linear-continuous representations of the radiation energy density are then tallied for use in the diffusion

solver. Section 4.3.1 shows results from a test case in which the material and radiation field start in equilibrium. The results indicate that the implementation choice made for the Monte Carlo transport solver and the diffusion solver can yield the expected behavior when starting in equilibrium.

Section 4.3.2 provides results for an equilibration test using a constant treatment of the opacity. The temperatures obtained from DAIMC for a single zone follow those of the analytic solutions modeled by Eq. (4.6) and Eq. (4.8), as illustrated in Figure 4.25. It can be verified that each of the nine zones in Figures 4.22, 4.23, and 4.24 have the same equilibrium temperatures which oscillate around this analytic solution. These three figures show that as the number of particle histories increase the interval range of the temperature decreases. This is expected since increasing the number of particles gives more resolution (noise reduction) in the temperature for a given problem. The results indicate the implementation choice of the Monte Carlo transport solver and the diffusion solver can produce solutions which follow the time evolution of Eq. (4.6) and Eq. (4.8).

Section 4.3.3 presents results from a problem in which a material has 'hot' zones and 'cold' zones. To our knowledge, an analytic solution in time is not available in literature, and therefore a time evolution comparison with a known analytic solution cannot be made. We allow the problem to equilibrate and compare the results from DAIMC to those of the analytic equilibrium solution. The problem simulated a total of 1,200 time steps. The final material and radiation temperatures from DAIMC oscillate about the analytic equilibrium temperature of 1.531 keV, as shown in Figure 4.32 and Figure 4.33. This indicates that the choice of

a piecewise constant treatment of the temperature and the linear-discontinuous treatment of the radiation energy density can produce the expected analytic equilibrium solution.

The 'hot corner' problem from Section 4.3.4 shows the temperature change and equilibration of a homogeneous material with hot and cold zones. The time evolution of the temperatures for both DAIMC and IMC are comparable, as shown in Figures 4.36 - 4.39. DAIMC and IMC both yield the correct analytic equilibrium temperature, as shown in Figures 4.40 and 4.41, respectively.

Section 4.3.5 provides results for radiation flow in a crooked pipe using 2520 zones. The problem starts with a portion of the pipe at a temperature of 3.0 keV, as shown in Figures 4.42 and 4.43. The results after 100 time steps from DAIMC and IMC are comparable as the propagation of the radiation reached the same portion of the pipe, as illustrated in Figures 4.44 and 4.45. DAIMC shows higher temperatures near the interface of the thick and thin material than the IMC method. This behavior can be observed when comparing Figures 4.46 and 4.47. After 500 time steps, the DAIMC method shows that the radiation has made farther into the pipe than the IMC method, as shown in Figures 4.48 and 4.49. The temperatures after 1000 time steps for DAIMC and IMC are shown in Figures 4.50 and 4.51. Figure 4.51 shows that the zones near the interfaces have a higher temperature than the zones that are closer to the interior of the pipe. This overheating of the zones near the interface introduces more radiation into the system and therefore causes the radiation to propagate farther into the pipe when using the DAIMC method than is observed in the IMC results.

Section 4.3.5.1 provides results for radiation flow in a crooked pipe using more zones. A total of 9904 zones were used to model the crooked pipe. The problem starts with some initial zones at a temperature of 3.0 keV, as shown in Figures 4.52 and 4.53. After 100 time steps, the temperatures for DAIMC and IMC are shown in Figures 4.54 and 4.55. A comparison of Figures 4.44, 4.45, 4.54, and 4.55 show that the radiation has reached the same portion of the pipe. A closer examination of Figures 4.45 and 4.55 show that the interface between the thick and thin material has a higher temperature using a refined mesh for DAIMC. This is also observed with the IMC method, as shown in Figures 4.44 and 4.54. After the 200 time steps, the radiation wave front computed by DAIMC and IMC reaches the same approximate location of the pipe as is evident in Figures 4.46, 4.47, 4.56, and 4.57. A nonphysical overheating of the IMC method can be observed in the refined mesh, as shown in Figure 4.56, which is not present in Figure 4.46. Figures 4.48, 4.58, and 4.59 show the radiation reaching the same approximate region into the pipe after 500 time steps. In contrast, Figure 4.49 shows that the radiation as propagated farther into the pipe. This may be caused by the nonphysical overheating at interface of the material with DAIMC, which cannot be resolved by the coarser mesh used in Section 4.3.5. The DAIMC results after 1000 time steps are provided in Figures 4.51 and 4.61. It is observed that using mesh refinement can help the nonphysical overheating at the interface, and, consequently, lead to radiation propagation that is similar to that of the IMC method. This can be observed when comparing the temperatures of DAIMC in Figures 4.51 and 4.61 to those of Figure 4.50.

The previous test problems all used a temperature independent treatment of the opacity. The test problems from Section 4.3.6 use a temperature varying opacity. Section 4.3.6.1 provides results for which the opacity varies proportionally with T^{-1}. For larger time steps, such as $\Delta t = 1.0 \cdot 10{-}3$ sh and $\Delta t = 1.0 \cdot 10{-}4$ sh, the IMC method exhibits an overheating behavior of the material. This effect is not observed with the results of DAIMC. The overheating of IMC can be remedied by using a smaller time step such as $\Delta t = 1.0 \cdot 10{-}5$ sh, as shown in Figure 4.64. Table 4.6 compares the ℓ_2 and ℓ_∞-norms of the error for DAIMC and IMC for various time steps sizes. The norms for both IMC and DAIMC decrease as the time step size decreases, as shown in Table 4.6. We observe that the DAIMC results are more accurate than the IMC results when comparing the norms.

Section 4.3.6.2 provides results for which the opacity varies proportionally with T^{-2}. When using a time step $\Delta t = 1.0 \cdot 10{-}3$ sh, DAIMC fails to converge to the correct equilibrium solution, as illustrated in Figure 4.67. By refining the time step size, the DAIMC results approach the expected analytic equilibrium solution. This can be confirmed by comparing the norms of the DAIMC results for different time step sizes in Table 4.6. The material overheating from IMC can be observed with all the time step sizes in this study, as shown in Figures 4.67, 4.68 and 4.69. When smaller time step sizes are used, such as $\Delta t = 1.0 \cdot 10{-}5$ sh and $\Delta t = 1.0 \cdot 10{-}6$ sh, DAIMC yields results that are more accurate than IMC when comparing the norms.

The piecewise constant treatment of the temperature for the Monte Carlo transport and the linear-continuous discretization of the diffusion equation can provide

accurate results when the opacity is treated as constant or varies as T^{-1}. When the opacity varies at T^{-2}, smaller time step sizes are required with the current implementation choice of DAIMC in order to obtain the correct equilibrium solution.

Chapter 6: Conclusions and Future Work

The goal of this research was to derive, implement and assess a new transport-diffusion hybrid method for thermal radiative transfer (TRT) problems. This was accomplished by rewriting the TRT equations as a Newton system; then, nonlinear elimination is applied to the TRT Newton system. This resulted in a system of equations which can be solved using an implicit capture transport Monte Carlo algorithm coupled to a diffusion approximation.

Chapter 3 detailed the mathematical framework for DAIMC. By formulating the TRT equations as a Newton system, nonlinear elimination (NLEM) can be applied to the system as a preconditioner. We then seek a solution to the equations that is a combination of a) the solution of a transport equation without scattering and b) the solution of a diffusion equation. The use of NLEM requires an additional solver for the material energy residual equation at the beginning and end of each Newton step.

Chapter 4 includes numerical results obtained from DAIMC for verification purposes. In developing the DAIMC algorithm, a series of test problems were used to verify its behavior. The 1D test problems used a constant treatment for the opacity. For problems where an analytic solution in time can be obtained, it was observed that DAIMC yields more accurate results than IMC. The QMC implementation of DAIMC maintained the accuracy of the MC implementation

while decreasing the number of required iterations and, consequently, run-time.

The 2D implementation of DAIMC used a piecewise constant treatment for the temperature and a linear-continuous discretization of the diffusion equation. In Section 4.3.1 and 4.3.2, the DAIMC results show that the implementation choices in 2D can produce the expected analytic equilibrium solutions.

The crooked pipe results from Section 4.3.5 suggest that mesh refinement is required to resolve the nonphysical overheating at the interface of the thick and thin region. On a coarser mesh, the DAIMC method propagates the radiation farther into the pipe than the IMC method. This is due to the nonphysical overheating of DAIMC. The overheating can be remedied by using a mesh refinement, as evident by the results in Section 4.3.5.1.

Several test problems were studied in which the opacity was a non-linear function of temperature to assess the behavior of several implementation choices. The results from Section 4.3.4.1 indicate that DAIMC can produce the equilibrium solution and provide more accurate results than IMC when comparing the l_2-norms and infinity-norms, in instances where the opacity varies as T^{-1}. In Section 4.3.4.2, problems in which the opacity varies as T^{-2} indicate that the implementation of DAIMC requires small time steps in order to produce the correct equilibrium solution. However, once a sufficiently small step size is used to produce the correct equilibrium solution, DAIMC provides more accurate results than the IMC results. This can be observed when comparing the norms, as discussed in Chapter 5.

6.1 Future Work

Since DAIMC is a novel method, there are several improvements which will be explored. The 1D and 2D implementation of DAIMC did not consider efficiency. The current implementation requires the diffusion matrix to be built after each transport iteration. There may be an increase in efficiency if the diffusion matrix is built once at the beginning of each time step and only the right hand side of the diffusion equation is updated after each transport iteration. Another improvement can be made by solving the material energy residual in parallel since this is done locally in each zone.

The implementation of QMC in higher dimensions can be useful in providing convergence and efficiency studies. Results from implementing QMC with DAIMC in 1D suggests that more efficient and accurate solutions can be obtained than the traditional IMC method.

Bibliography

[1] G. C. Pomraning, "Radiation hydrodynamics," Los Alamos National Lab., NM (United States), Tech. Rep., 1982.

[2] J. Howell, M. Menguc, and R. Siegel, *Thermal Radiation Heat Transfer*. CRC Press, 2015, ISBN: 9781498757744. [Online]. Available: https://books.google.com/books?id=aeSYCgAAQBAJ.

[3] H. Harde, "Radiation and heat transfer in the atmosphere: A comprehensive approach on a molecular basis," *International Journal of Atmospheric Sciences*, vol. 2013, Oct. 2013. DOI: 10.1155/2013/503727.

[4] A. F. Bielajew, "Fundamentals of the Monte Carlo method for neutral and charged particle transport," *The University of Michigan*, vol. 1, 2001.

[5] A. B. Wollaber, "Four decades of Implicit Monte Carlo," *Journal of Computational and Theoretical Transport*, vol. 45, no. 1-2, pp. 1–70, 2016.

[6] J. Fleck Jr and J. Cummings Jr, "An implicit Monte Carlo scheme for calculating time and frequency dependent nonlinear radiation transport," *Journal of Computational Physics*, vol. 8, no. 3, pp. 313–342, 1971.

[7] T. A. BRUNNER, "Forms of approximate radiation transport," Sandia National Labs., Albuquerque, NM (US); Sandia National Labs ..., Tech. Rep., 2002.

[8] A. B. Wollaber, *Advanced Monte Carlo methods for thermal radiation transport*. University of Michigan, 2008.

[9] J. I. Castor, *Radiation hydrodynamics*. 2004.

[10] E. E. Lewis and W. F. Miller, "Computational methods of neutron transport," 1984.

[11] W. Miller Jr and W. H. Reed, "Ray-effect mitigation methods for two-dimensional neutron transport theory," *Nuclear Science and Engineering*, vol. 62, no. 3, pp. 391–411, 1977.

[12] T. A. Brunner, "Mulard: A multigroup thermal radiation diffusion mini-application," 2012.

[13] J. Howell, M. P. Mengüç, and R. Siegel, *Thermal radiation heat transfer, sixth edition*. Jan. 2015, pp. 1–971.

[14] J. Morel, "Diffusion-limit asymptotics of the transport equation, the p1/3 equations, and two flux-limited diffusion theories," *Journal of Quantitative Spectroscopy and Radiative Transfer*, vol. 65, no. 5, pp. 769–778, 2000.

[15] G. L. Olson, L. H. Auer, and M. L. Hall, "Diffusion, p_1, and other approximate forms of radiation transport," *Journal of Quantitative Spectroscopy and Radiative Transfer*, vol. 64, no. 6, pp. 619–634, 2000.

[16] C. D. Levermore and G. C. Pomraning, "A flux-limited diffusion theory," *The Astrophysical Journal*, vol. 248, pp. 321–334, Aug. 1981. DOI: 10.1086/159157.

[17] T. Haut, C. Ahrens, A. Jonko, R. Lowrie, and A. Till, "A new multigroup method for cross-sections that vary rapidly in energy," *Journal of Quantitative Spectroscopy and Radiative Transfer*, vol. 187, pp. 461–471, Jan. 2017, ISSN: 0022-4073. DOI: 10.1016/j.jqsrt.2016.10.019. [Online]. Available: http://dx.doi.org/10.1016/j.jqsrt.2016.10.019.

[18] D. Mihalas and B. W. Mihalas, *Foundations of radiation hydrodynamics*. Courier Corporation, 2013.

[19] F. GrazianI, "Radiation diffusion: An overview of physical and numerical concepts," in *Open Issues in Core Collapse Supernova Theory*, World Scientific, 2005, pp. 29–66.

[20] S. R. Bolding, M. A. Cleveland, and J. E. Morel, "A high-order low-order algorithm with exponentially convergent Monte Carlo for thermal radiative transfer," *Nuclear Science and Engineering*, vol. 185, no. 1, Feb. 2017. DOI: 10.13182/nse16-36.

[21] J. Fleck and E. Canfield, "A random walk procedure for improving the computational efficiency of the Implicit Monte Carlo method for nonlinear radiation transport," *Journal of Computational Physics*, vol. 54, no. 3, pp. 508–523, 1984, ISSN: 0021-9991. DOI: https://doi.org/10.1016/0021-9991(84)90130-X. [Online]. Available: https://www.sciencedirect.com/science/article/pii/002199918490130X.

[22] N. Gentile, "Implicit Monte Carlo diffusion—an acceleration method for Monte Carlo time-dependent radiative transfer simulations," *Journal of Computational Physics*, vol. 172, no. 2, pp. 543–571, 2001.

[23] M. A. Cleveland, N. A. Gentile, and T. S. Palmer, "An extension of Implicit Monte Carlo diffusion: Multigroup and the difference formulation," *J. Comput. Phys.*, vol. 229, no. 16, pp. 5707–5723, 2010. DOI: 10.1016/j.jcp.2010.04.004. [Online]. Available: https://doi.org/10.1016/j.jcp.2010.04.004.

[24] J. D. Densmore, T. J. Urbatsch, T. M. Evans, and M. W. Buksas, "A hybrid transport-diffusion method for Monte Carlo radiative-transfer simulations," *Journal of Computational Physics*, vol. 222, no. 2, pp. 485–503, 2007, ISSN: 0021-9991. DOI: https://doi.org/10.1016/j.jcp.2006.07.031. [Online]. Available: https://www.sciencedirect.com/science/article/pii/S0021999106003639.

[25] E. W. Larsen and B. Mercer, "Analysis of a Monte Carlo method for nonlinear radiative transfer," *Journal of Computational Physics*, vol. 71, no. 1, pp. 50–64, 1987.

[26] M. A. Cleveland and A. B. Wollaber, "Corrected Implicit Monte Carlo," *Journal of Computational Physics*, vol. 359, pp. 20–44, 2018.

[27] N. Gentile and B. C. Yee, "Iterative Implicit Monte Carlo," *Journal of Computational and Theoretical Transport*, vol. 45, no. 1-2, pp. 71–98, 2016.

[28] A. Long, N. A. Gentile, and T. S. Palmer, "The iterative thermal emission method: A more implicit modification of imc," *Journal of Computational Physics*, vol. 277, pp. 228–247, 2014.

[29] A. B. Wollaber, E. W. Larsen, and J. D. Densmore, "A discrete maximum principle for the Implicit Monte Carlo equations," *Nuclear Science and Engineering*, vol. 173, no. 3, pp. 259–275, 2013.

[30] R. Vega and T. Brunner, "Nuen-618 class project: Actually implicit Monte Carlo," Lawrence Livermore National Lab.(LLNL), Livermore, CA (United States), Tech. Rep., 2017.

[31] D. Kershaw, "Flux limiting nature's own way – a new method for numerical solution of the transport equation," 1976.

[32] J. Lou, J. E. Morel, and N. Gentile, "A Variable Eddington Factor method for the 1-d grey radiative transfer equations with discontinuous galerkin and mixed finite-element spatial differencing," *Journal of Computational Physics*, vol. 393, pp. 258–277, 2019, ISSN: 0021-9991. DOI: https://doi.org/10.1016/j.jcp.2019.05.012.

[33] S. S. Olivier and J. E. Morel, "Variable Eddington Factor Method for the s_n equations with lumped discontinuous galerkin spatial discretization coupled to a drift-diffusion acceleration equation with mixed finite-element discretization," *Journal of Computational and Theoretical Transport*, vol. 46, no. 6-7, pp. 480–496, 2017. DOI: 10.1080/23324309.2017.1418378. eprint:

https://doi.org/10.1080/23324309.2017.1418378. [Online]. Available: https://doi.org/10.1080/23324309.2017.1418378.

[34] T. A. Brunner and P. F. Nowak, "Nonlinear elimination applied to radiation transport," Lawrence Livermore National Lab.(LLNL), Livermore, CA (United States), Tech. Rep., 2019.

[35] P. J. Lanzkron, D. J. Rose, and J. T. Wilkes, "An analysis of approximate nonlinear elimination," *SIAM J. Sci. Comput.*, vol. 17, no. 2, pp. 538–559, Mar. 1996, ISSN: 1064-8275. DOI: 10.1137/S106482759325154X. [Online]. Available: https://doi.org/10.1137/S106482759325154X.

[36] J. D. Densmore and E. W. Larsen, "Asymptotic equilibrium diffusion analysis of time-dependent Monte Carlo methods for grey radiative transfer," *Journal of Computational Physics*, vol. 199, no. 1, pp. 175–204, 2004.

[37] J. E. Morel, T. .-Y. Brian Yang, and J. S. Warsa, "Linear multifrequency-grey acceleration recast for preconditioned Krylov iterations," *Journal of Computational Physics*, vol. 227, no. 1, Nov. 2007, ISSN: 0021-9991. DOI: 10.1016/j.jcp.2007.07.033. [Online]. Available: https://www.osti.gov/biblio/21028289.

[38] J. Morel, E. Larsen, and M. Matzen, "A synthetic acceleration scheme for radiative diffusion calculations," *Journal of Quantitative Spectroscopy and Radiative Transfer*, vol. 34, no. 3, pp. 243–261, 1985, ISSN: 0022-4073. DOI: https://doi.org/10.1016/0022-4073(85)90005-6. [Online]. Available: https://www.sciencedirect.com/science/article/pii/0022407385900056.

[39] S. W. Mosher, "Exact solution of a nonlinear, time-dependent, infinite-medium, grey radiative transfer problem," *Transactions*, vol. 95, no. 1, pp. 744–747, 2006.

[40] A. B. Owen, "Monte Carlo, Quasi-Monte Carlo, and randomized Quasi-Monte Carlo," *Monte-Carlo and Quasi-Monte Carlo Methods 1998*, pp. 86–97, 2000.

[41] S. Joe and F. Y. Kuo, "Constructing Sobol sequences with better two-dimensional projections," *SIAM Journal on Scientific Computing*, vol. 30, no. 5, pp. 2635–2654, 2008.

[42] R. E. Caflisch, "Monte Carlo and Quasi-Monte Carlo methods," *Acta numerica*, vol. 7, pp. 1–49, 1998.

[43] A. B. Owen, "Scrambling Sobol' and Niederreiter-Xing points," *Journal of complexity*, vol. 14, no. 4, pp. 466–489, 1998.

[44] H. Chi, M. Mascagni, and T. Warnock, "On the optimal Halton sequence," *Mathematics and computers in simulation*, vol. 70, no. 1, pp. 9–21, 2005.

[45] E. I. Atanassov, "A new efficient algorithm for generating the scrambled Sobol' sequence," in *International Conference on Numerical Methods and Applications*, Springer, 2002, pp. 83–90.

[46] R. Anderson, J. Andrej, A. Barker, J. Bramwell, J.-S. Camier, J. C. V. Dobrev, Y. Dudouit, A. Fisher, T. Kolev, W. Pazner, M. Stowell, V. Tomov, I. Akkerman, J. Dahm, D. Medina, and S. Zampini, "MFEM: A modular fi-

nite element methods library," *Computers & Mathematics with Applications*, vol. 81, pp. 42–74, 2021. DOI: 10.1016/j.camwa.2020.06.009.

[47] MFEM, *Mfem: Modular finite elements method [software]*, 2021. DOI: 10.11578/dc.20171025.1248.

[48] C. T. Kelley, *Iterative methods for linear and nonlinear equations*. SIAM, 1995.

[49] S. Boyd, S. P. Boyd, and L. Vandenberghe, *Convex optimization*. Cambridge university press, 2004.

[50] M. L. Adams, "A new transport discretization scheme for arbitrary spatial meshes in xy geometry," Lawrence Livermore National Lab., CA (USA), Tech. Rep., 1991.

[51] K. Salari and P. Knupp, "Code verification by the method of manufactured solutions," Sandia National Labs., Albuquerque, NM (US); Sandia National Labs ..., Tech. Rep., 2000.

[52] J. J. Duderstadt and L. J. Hamilton, *Nuclear Reactor Analysis*. Wiley, 1976.

APPENDICES

Appendix A: Newton's Method for Nonlinear Systems

The general form of Newton's method for nonlinear systems of equations is

$$\mathbf{f}(\mathbf{x}) = 0, \tag{A.1}$$

where

$$\mathbf{x} = \begin{bmatrix} x_1 \\ x_2 \\ \vdots \\ x_n \end{bmatrix}, \tag{A.2}$$

and

$$\mathbf{f}(\mathbf{x}) = \begin{bmatrix} f_1(x_1, x_2, ..., x_n) \\ f_2(x_1, x_2, ..., x_n) \\ \vdots \\ f_n(x_1, x_2, ..., x_n) \end{bmatrix} = 0. \tag{A.3}$$

Newton's method has the form of

$$\mathbf{x}_{n+1} = \mathbf{x}_n - \frac{\mathbf{f}(\mathbf{x}_n)}{\mathbf{f}'(\mathbf{x}_n)}, \tag{A.4}$$

where

$$\mathbf{f}'(\mathbf{x}_n) = \mathbf{J}(\mathbf{x}_n) \tag{A.5}$$

is known as the Jacobian and

$$\frac{1}{\mathbf{f}'(\mathbf{x}_n)} = \mathbf{J}^{-1}(\mathbf{x}_n) \tag{A.6}$$

the inverse of the Jacobian.

The Jacobian is defined as

$$\mathbf{J}_{i,j} = \begin{bmatrix} \frac{\partial f_1}{\partial x_1} & \frac{\partial f_1}{\partial x_2} & \cdots & \frac{\partial f_1}{\partial x_n} \\ \frac{\partial f_2}{\partial x_1} & \frac{\partial f_2}{\partial x_2} & \cdots & \frac{\partial f_2}{\partial x_n} \\ \cdots & \cdots & \cdots & \cdots \\ \frac{\partial f_n}{\partial x_1} & \frac{\partial f_n}{\partial x_2} & \cdots & \frac{\partial f_n}{\partial x_n} \end{bmatrix}$$

and using the Jacobian, Eq. (A.4) can be written as

$$\mathbf{x}_{n+1} = \mathbf{x}_n - \mathbf{J}^{-1}_{i,j}(\mathbf{x}_n)\mathbf{f}(\mathbf{x}_n). \tag{A.7}$$

The above equation can be rearranged to

$$\mathbf{x}_{n+1} - \mathbf{x}_n = -\mathbf{J}^{-1}_{i,j}(\mathbf{x}_n)\mathbf{f}(\mathbf{x}_n) \tag{A.8}$$

and define

$$\delta\mathbf{x_n} = \mathbf{x}_{n+1} - \mathbf{x}_n, \tag{A.9}$$

to obtain

$$\delta \mathbf{x_n} = -\mathbf{J}_{i,j}^{-1}(\mathbf{x}_n)\mathbf{f}(\mathbf{x}_n). \tag{A.10}$$

Typically, the inverse of the Jacobian is difficult to compute, or it does not exist, so

$$\mathbf{J}_{i,j}(\mathbf{x}_n)\delta \mathbf{x_n} = -\mathbf{f}(\mathbf{x}_n) \tag{A.11}$$

is used instead [48].

Using 2 variables e and ϕ (i.e., $\mathbf{J}_{i,j} \rightarrow \mathbf{J}_{e,\phi}$, $\delta \mathbf{x_n} \rightarrow \delta \mathbf{x_{e,\phi}}$, $f(\mathbf{x}_n) \rightarrow f(e,\phi)$), Eq. (A.11) becomes

$$\mathbf{J}_{e,\phi}\delta \mathbf{x_{e,\phi}} = -f(e,\phi). \tag{A.12}$$

For convenience, define

$$\delta \mathbf{x_{e,\phi}} = \begin{bmatrix} \delta_e \\ \delta_\phi \end{bmatrix}, \tag{A.13}$$

$$f(e,\phi) = \begin{bmatrix} m(e^l,\phi^l) \\ r(e^l,\phi^l) \end{bmatrix}, \tag{A.14}$$

$$\mathbf{J}_{e,\phi} = \begin{bmatrix} J_{e,e} & J_{e,\phi} \\ J_{\phi,e} & J_{\phi,\phi} \end{bmatrix} = \begin{bmatrix} \mathbf{A} & \mathbf{B} \\ \mathbf{C} & \mathbf{D} \end{bmatrix}, \tag{A.15}$$

and substituting back into equation (A.12) to get

$$\begin{bmatrix} \mathbf{A} & \mathbf{B} \\ \mathbf{C} & \mathbf{D} \end{bmatrix} \begin{bmatrix} \delta_e \\ \delta_\phi \end{bmatrix} = - \begin{bmatrix} m(e^l, \phi^l) \\ r(e^l, \phi^l) \end{bmatrix}. \tag{A.16}$$

A.1 Schur Complement

A generic matrix

$$\mathbf{M} = \begin{bmatrix} \mathbf{A} & \mathbf{B} \\ \mathbf{C} & \mathbf{D} \end{bmatrix}, \tag{A.17}$$

has certain properties when A is invertible. Write Eq. (A.16) as

$$\begin{bmatrix} \mathbf{A} & \mathbf{B} \\ \mathbf{C} & \mathbf{D} \end{bmatrix} \begin{bmatrix} \delta_e \\ \delta_\phi \end{bmatrix} = - \begin{bmatrix} m(e^l, \phi^l) \\ r(e^l, \phi^l) \end{bmatrix}. \tag{A.18}$$

For clarity, it will be useful to change $\delta_e \to x$ and $\delta_\phi \to y$, and rewrite Eq. (A.18) as

$$\begin{bmatrix} \mathbf{A} & \mathbf{B} \\ \mathbf{C} & \mathbf{D} \end{bmatrix} \begin{bmatrix} x \\ y \end{bmatrix} = - \begin{bmatrix} m(e^l, \phi^l) \\ r(e^l, \phi^l) \end{bmatrix}. \tag{A.19}$$

The system in Eq. (A.19) is

$$\mathbf{A}x + \mathbf{B}y = -m(e^l, \phi^l), \tag{A.20a}$$

$$\mathbf{C}x + \mathbf{D}y = -r(e^l, \phi^l). \tag{A.20b}$$

If A is invertible, then multiplying Eq. (54a) by CA^{-1} (Step 1) and subtracting from Eq. (54b) (Step 2) we have

Step 1:

$$\mathbf{C}\mathbf{A}^{-1}(\mathbf{A}x + \mathbf{B}y) = -\mathbf{C}\mathbf{A}^{-1}(m(e^l, \phi^l)) \tag{A.21a}$$

$$\mathbf{C}\mathbf{A}^{-1}\mathbf{A}x + \mathbf{C}\mathbf{A}^{-1}\mathbf{B}y = -\mathbf{C}\mathbf{A}^{-1}(m(e^l, \phi^l)) \tag{A.21b}$$

$$\mathbf{C}x + \mathbf{C}\mathbf{A}^{-1}\mathbf{B}y = -\mathbf{C}\mathbf{A}^{-1}(m(e^l, \phi^l)) \tag{A.21c}$$

Step 2:

$$\begin{aligned} &\mathbf{C}x + \mathbf{D}y && = -r(e^l, \phi^l) \\ &- \\ &\mathbf{C}x + \mathbf{C}\mathbf{A}^{-1}\mathbf{B}y && = -\mathbf{C}\mathbf{A}^{-1}(m(e^l, \phi^l)) \\ &\hline \\ &0 + (\mathbf{D} - \mathbf{C}\mathbf{A}^{-1}\mathbf{B})y && = -r(e^l, \phi^l) + \mathbf{C}\mathbf{A}^{-1}(m(e^l, \phi^l)). \end{aligned}$$

The final result is

$$(\mathbf{D} - \mathbf{CA^{-1}B})y = -r(e^l, \phi^l) + \mathbf{CA}^{-1}(m(e^l, \phi^l)). \tag{A.22}$$

and the term $(\mathbf{D} - \mathbf{CA^{-1}B})$ is called the Schur complement of $\mathbf{A}$ in $\mathbf{M}$ and only exist if $\mathbf{A}$ is invertible [49].

Appendix B: Diffusion Verification

B.1 1D Verification

Recall and focus on the left-hand side while inserting a place holder, Q, for the right-hand side. We have

$$-\nabla \cdot D\nabla E + \sigma_a E = Q. \tag{B.1}$$

Using a discontinuous, corner balance scheme in 1-d [50], we have

$$-\frac{\partial}{\partial x} D(x) \frac{\partial E}{\partial x} + \sigma(x) E(x) = Q(x). \tag{B.2}$$

Integrate Eq. (B.2) over half-cells:

$$\int_{x_{i-1/2}}^{x_i} Eq.\ (\text{B.2}) = -\ D(x) \frac{\partial E}{\partial x}\bigg|_{x_{i-1/2}}^{x_i} + \sigma_i E_{i,L}(\frac{\Delta x}{2}) = Q_{i,L}(\frac{\Delta x}{2}) \tag{B.3}$$

$$\int_{x_i}^{x_{i+1/2}} Eq.\ (\text{B.2}) = -\ D(x) \frac{\partial E}{\partial x}\bigg|_{x_i}^{x_{i+1/2}} + \sigma_i E_{i,R}(\frac{\Delta x}{2}) = Q_{i,R}(\frac{\Delta x}{2}) \tag{B.4}$$

Now, approximate the following:

$$-D(x)\frac{\partial E}{\partial x}\bigg|_{x_i} \approx -D_i\left(\frac{E_{i,R}-E_{i,L}}{\Delta x_i}\right) \tag{B.5}$$

$$\begin{aligned}-D(x)\frac{\partial E}{\partial x}\bigg|_{x_{i-1/2}} &\approx J_{i-1/2} = J^+_{i-1/2} - J^-_{i-1/2} = J^+_{i-1,R} - J^-_{i,L} \\ &= \left(\frac{E_{i-1,R}}{4} - \frac{D_{i-1}}{2}\left[\frac{E_{i-1,R}-E_{i-1,L}}{\Delta x_{i-1}}\right]\right) - \left(\frac{E_{i,L}}{4} + \frac{D_i}{2}\left[\frac{E_{i,R}-E_{i,L}}{\Delta x_i}\right]\right)\end{aligned} \tag{B.6}$$

$$\begin{aligned}-D(x)\frac{\partial E}{\partial x}\bigg|_{x_{i+1/2}} &= \\ &\left(\frac{E_{i,R}}{4} - \frac{D_i}{2}\left[\frac{E_{i,R}-E_{i,L}}{\Delta x_i}\right]\right) - \left(\frac{E_{i+1,L}}{4} + \frac{D_{i+1}}{2}\left[\frac{E_{i+1,R}-E_{i+1,L}}{\Delta x_{i+1}}\right]\right).\end{aligned} \tag{B.7}$$

Left Equation:

We combine Eq. (B.3),(B.5) and (B.6) to get the left half-cell averaged equation,

$$\begin{aligned}-\left(\frac{E_{i-1,R}-E_{i,L}}{4}\right) - \frac{D_i}{2}\left(\frac{E_{i,R}-E_{i,L}}{\Delta x_i}\right) + \frac{D_{i-1}}{2}\left(\frac{E_{i-1,R}-E_{i-1,L}}{\Delta x_{i-1}}\right) \\ + \sigma_i E_{i,L}(\frac{\Delta x_i}{2}) = Q_{i,L}(\frac{\Delta x_i}{2}).\end{aligned} \tag{B.8}$$

We collect like terms to obtain the system for the left half-cell

$$E_{i-1,L} \Longrightarrow -\left(\frac{D_{i-1}}{2\Delta x_{i-1}}\right) E_{i-1,L} \tag{B.9a}$$

$$E_{i-1,R} \Longrightarrow \left(\frac{D_{i-1}}{2\Delta x_{i-1}} - \frac{1}{4}\right) E_{i-1,R} \tag{B.9b}$$

$$E_{i,L} \Longrightarrow \left(\frac{1}{4} + \frac{D_i}{2\Delta x_i} + \frac{\sigma_{a,i}\Delta x_i}{2}\right) E_{i,L} \tag{B.9c}$$

$$E_{i,R} \Longrightarrow -\left(\frac{D_i}{2\Delta x_i}\right) E_{i,R}. \tag{B.9d}$$

Right Equation:

To obtain the right half-cell averaged equation, we combine Eq. (B.4),(B.5) and (B.7) to get

$$\left(\frac{E_{i,R} - E_{i+1,L}}{4}\right) + \frac{D_i}{2}\left(\frac{E_{i,R} - E_{i,L}}{\Delta x_i}\right) - \frac{D_{i+1}}{2}\left(\frac{E_{i+1,R} - E_{i+1,L}}{\Delta x_{i+1}}\right) + \sigma_{a,i} E_{i,R}(\frac{\Delta x_i}{2}) = Q_{i,R}(\frac{\Delta x_i}{2}). \tag{B.10}$$

We collect like terms to obtain the system for the right half-cell

$$E_{i,L} \Longrightarrow -\left(\frac{D_i}{2\Delta x_i}\right) E_{i,L} \tag{B.11a}$$

$$E_{i,R} \Longrightarrow \left(\frac{1}{4} + \frac{D_i}{2\Delta x_i} + \frac{\tilde{\sigma_{a,i}}\Delta x_i}{2}\right) E_{i,R} \tag{B.11b}$$

$$E_{i+1,L} \Longrightarrow \left(\frac{D_{i+1}}{2\Delta x_{i+1}} - \frac{1}{4}\right) E_{i+1,L} \tag{B.11c}$$

$$E_{i+1,R} \Longrightarrow -\left(\frac{D_{i+1}}{2\Delta x_{i+1}}\right) E_{i+1,R}. \tag{B.11d}$$

B.1.1 Method of Manufactured Solutions (MMS)

To verify the diffusion solver, we use the Method of Manufactured Solutions [51]. Assume the solution is

$$E = e^{-ax}, \tag{B.12a}$$

$$\frac{\partial E}{\partial x} = -ae^{-ax}, \tag{B.12b}$$

$$-D\frac{\partial}{\partial x}\frac{\partial E}{\partial x} = -Da^2 e^{-ax}. \tag{B.12c}$$

Equation (B.2) becomes

$$(-Da^2 + \tilde{\sigma_a})e^{-ax} = Q(x). \tag{B.13}$$

The parameters for this verification are as follows: $D = 1.9$, $a = 1.1$, $\tilde{\sigma_a} = 11.7$. For this test problem, the following incoming partial currents are imposed at the left and right boundaries [52]:

$$\text{Left BC: } J^+ = \frac{E}{4} - \frac{D}{2}\left.\frac{dE}{dx}\right|_0 \tag{B.14a}$$

$$\text{Right BC: } J^- = \frac{E}{4} + \frac{D}{2}\left.\frac{dE}{dx}\right|_{x_L} \tag{B.14b}$$

Results obtained from MMS for varying mesh sizes are given below.

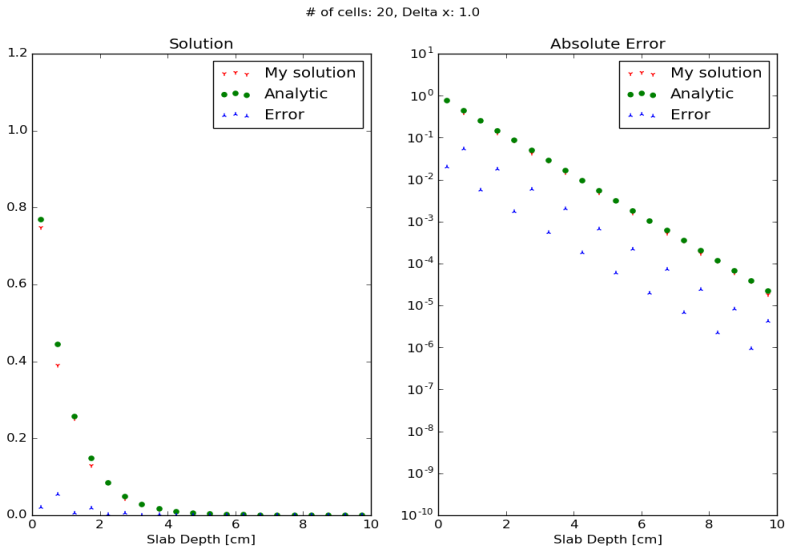

Figure B.1: The absolute error using a mesh size of 1.0 cm.

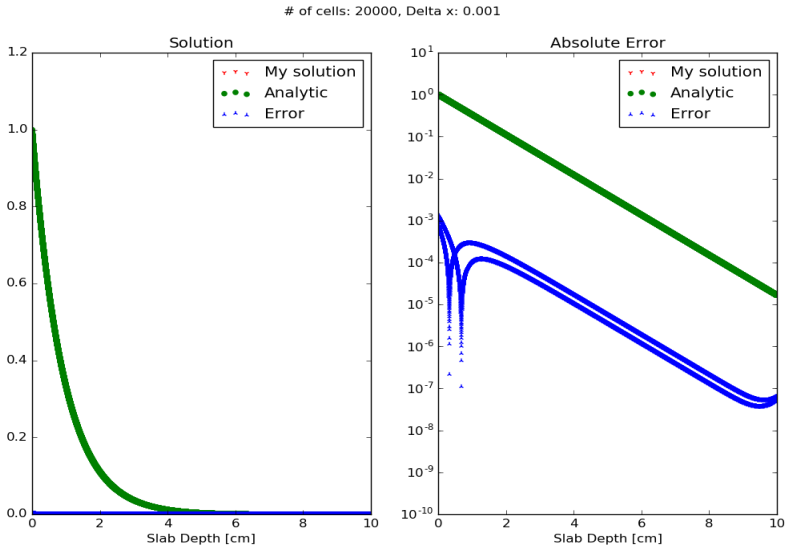

Figure B.2: The absolute error using a mesh size of 0.001 cm.

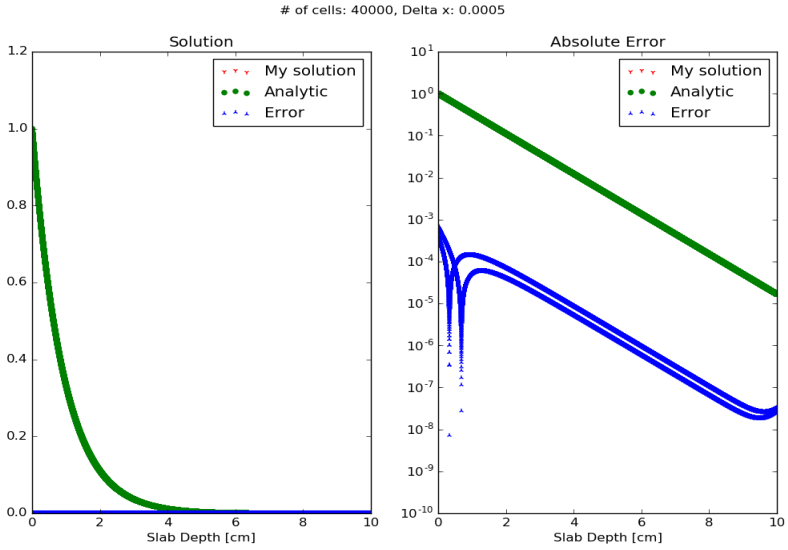

Figure B.3: The absolute error using a mesh size of 0.0005 cm.

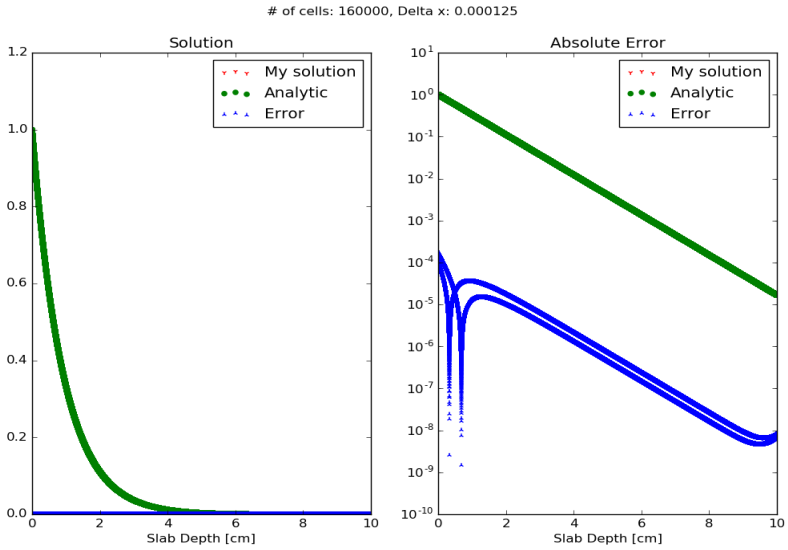

Figure B.4: The absolute error using a mesh size of 0.000125 cm.

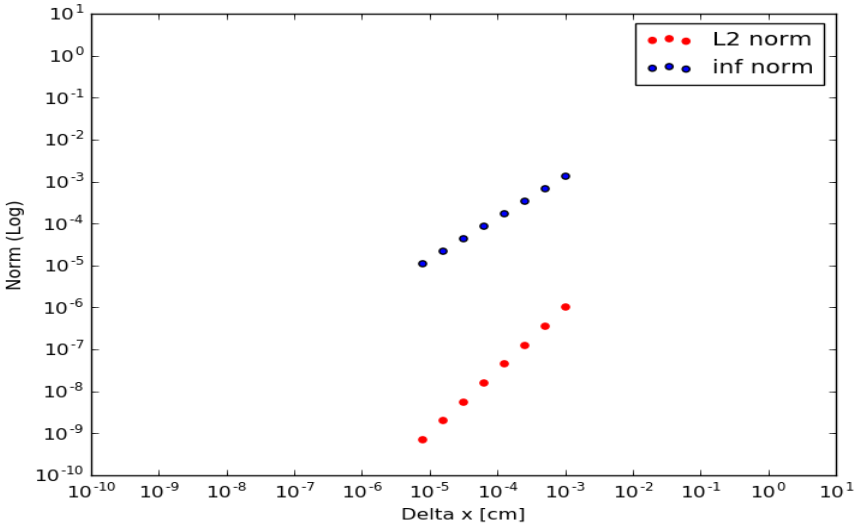

Figure B.5: The norm of the error vs mesh size.

Figure B.1 shows the solution of the diffusion solver using the discontinuous, corner-balance approach. As seen in the figure, the numerical solution labeled 'My solution' is visibly different from the analytic solution. This behavior is minimized as the mesh size is decreased, as illustrated is Figures B.2-B.4. The ∞-norm and the l_2-norm are used to measure the rate of convergence. Figure B.5 shows the two norms vs. mesh size. To measure the slope, we use

$$\text{slope}_n = \frac{\log(\text{error}(h_n)) - \log(\text{error}(h_{n+1}))}{\log(h_n) - \log(h_{n+1})}. \tag{B.15}$$

The l_2-norm has a slope of 1.5 and the ∞-norm has a slope of 1.0. The observed convergence behavior indicates the discontinuous, simple corner-balance discretization of Eq. (B.1) has implemented correctly.

B.2 2D Verification

For 2D-XY geometry, the diffusion equation

$$-\nabla \cdot D(x,y)\nabla E(x,y) + \sigma(x,y)E(x,y) = Q(x,y) \tag{B.16}$$

is solved using library for finite element methods called Modular Finite Element Method (MFEM) [46], [47]. MFEM is a free, lightweight, scalable C++ code developed by Lawrence Livermore National Laboratory (LLNL). The diffusion acceleration of DAIMC in 2D-XY (and consequently 3D-XYZ) uses the continuous diffusion-reaction solver from MFEM. Results for the verification of this diffusion

solver are given in the subsequent sections.

B.2.1 Square Mesh

The following figures show the results of Eq. (B.16) with constant data of $Q = 8.0, \sigma = 4.0, D = \frac{1}{3\sigma} = 1/12$ on a 2D-XY square mesh. The results aim to demonstrate the correct behavior on the boundaries.

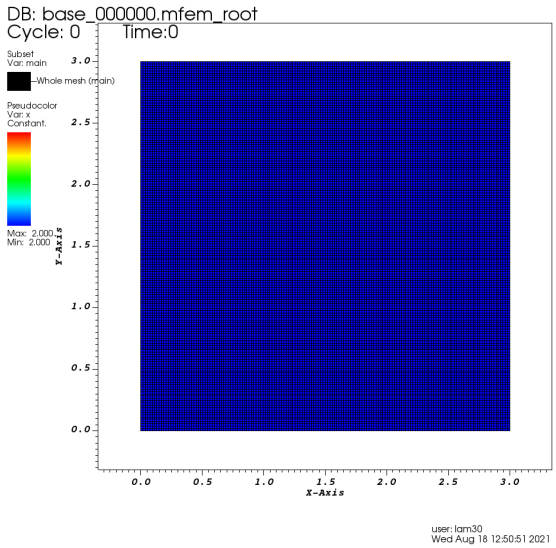

Figure B.6: 2D diffusion solution using reflecting boundary conditions on a square mesh..

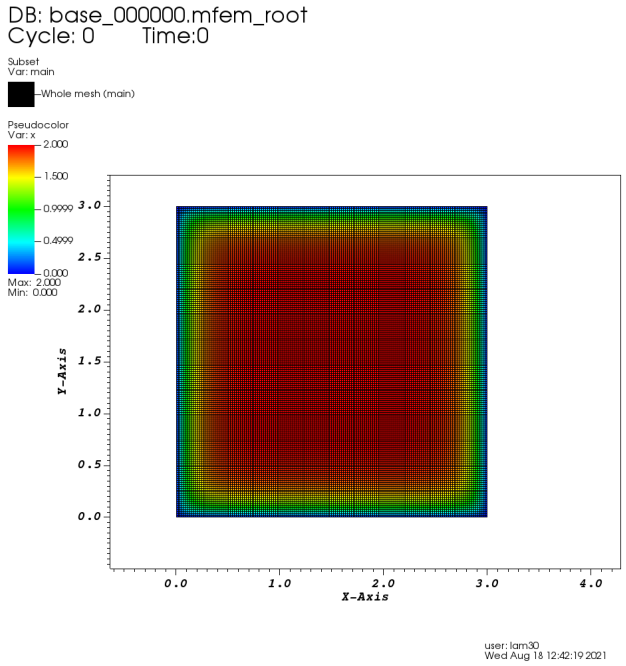

Figure B.7: 2D diffusion solution using homogenous Dirichlet boundary conditions on a square mesh.

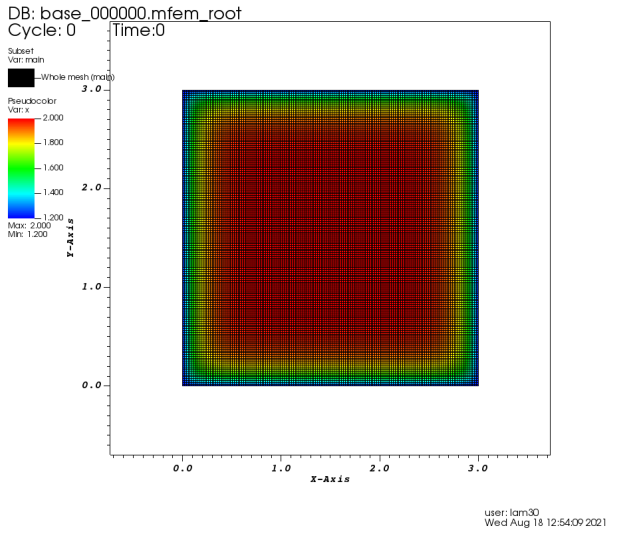

Figure B.8: 2D diffusion solution using non-homogenous Dirichlet boundary on a square mesh.

The analytic solution for an infinite-medium, with the data above is given by

$$E = \frac{Q}{\sigma} = 2.0. \tag{B.17}$$

Figure B.6 shows that the numerical solution agrees with Eq. (B.17) for the reflecting boundary case. For problems which the Dirichlet boundary conditions are specified, the solution at the center of the mesh should be

$$E \approx \frac{Q}{\sigma} = 2.0. \tag{B.18}$$

Figure B.7 preserves the value of Eq. (B.18) at the center while also taking the homogenous boundary conditions, as expected. Figure B.8 also follows the same behavior as Figure B.8 with the exception of taking on the prescribed, nonhomegenous Dirichlet boundary conditions of 1.2.

B.2.2 Star Mesh

We repeat the same set of tests but on a more complex star mesh. The results follow that of the square mesh results from the previous subsections.

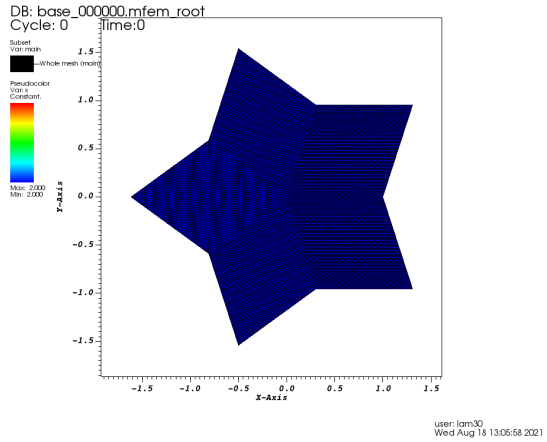

Figure B.9: 2D diffusion solution using reflecting boundary conditions on a star mesh.

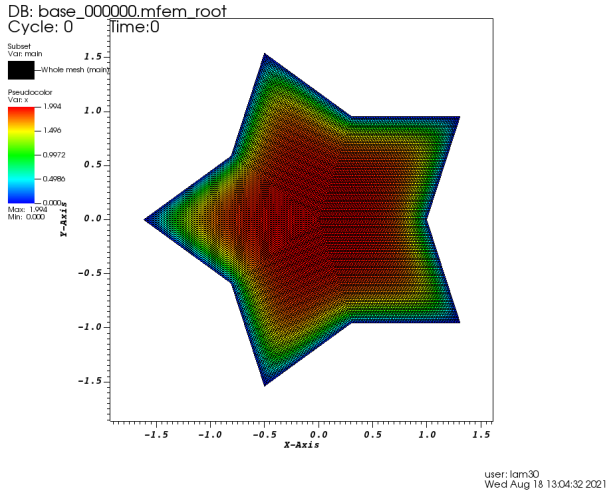

Figure B.10: 2D diffusion solution using homogenous Dirichlet boundary conditions on a star mesh.

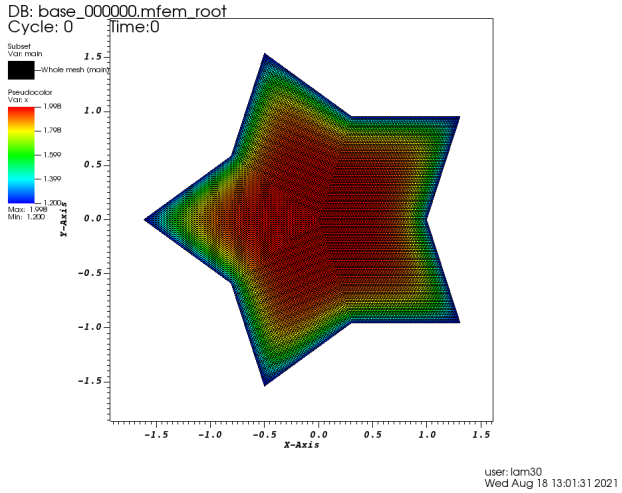

Figure B.11: 2D diffusion solution using non-homogenous Dirichlet boundary conditions on a star mesh.

Figure B.9 shows that the numerical solution agrees with Eq. (B.17) for the reflecting boundary case. Figure B.7 preserves the value of Eq. (B.18) at the center while also taking the homogenous boundary conditions, as expected. Figure B.8 also follows the same behavior as Figure B.8 with the exception of taking on the prescribed, nonhomegenous Dirichlet boundary conditions of 1.2.

B.2.3 Method of Manufactured Solution (MMS)

We now use MMS to verify our implementation of MFEM's diffusion solver to the equation

$$-\nabla \cdot D(x,y)\nabla E(x,y) + \sigma E(x,y) = Q(x,y). \tag{B.19}$$

The manufactured solution chosen is of the form

$$E(x,y) = sin(\pi x)sin(\pi y), \tag{B.20}$$

and the opacity data consists of

$$\sigma(x,y) = \frac{1}{e^x e^y}, \tag{B.21}$$

and consequently,

$$D(x,y) = \frac{1}{3\sigma(x,y)} = \frac{1}{3}e^x e^y. \tag{B.22}$$

Inserting these definitions into Eq. (B.19) and the source term is

$$-\left(\frac{\pi}{3}e^x e^y cos(\pi x)sin(\pi x) + \frac{\pi}{3}e^x e^y sin(\pi x)cos(\pi x) - \frac{2\pi^2}{3}e^x e^y sin(\pi x)sin(\pi y)\right) + \frac{1}{e^x e^y}sin(\pi x)sin(\pi y) = Q(x,y). \tag{B.23}$$

The results model a square with length x from (0.0,1.0) and y from (0.0, 1.0) with different mesh sizes.

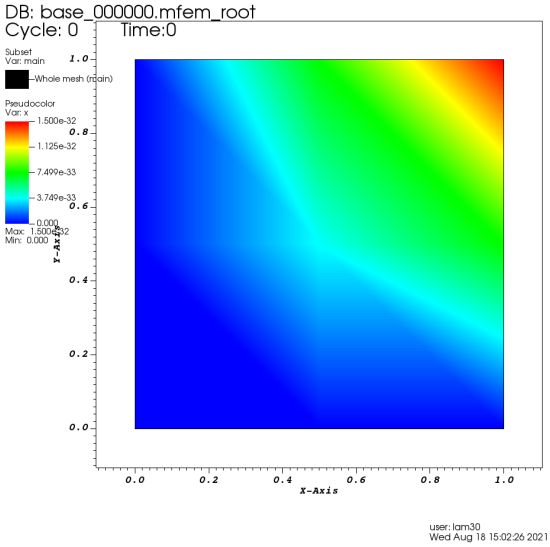

Figure B.12: The MMS solution for a single zone mesh.

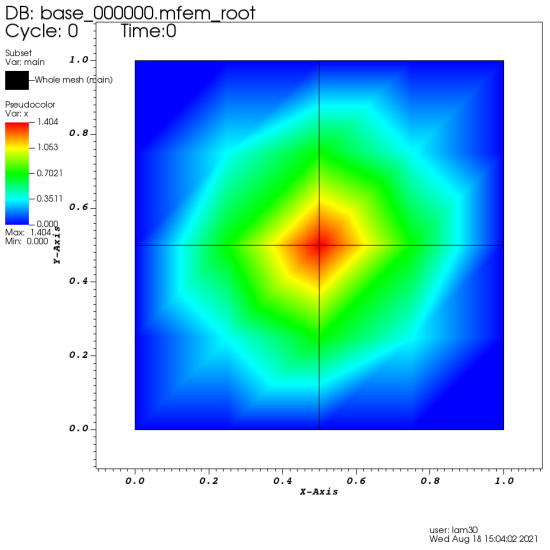

Figure B.13: The MMS solution for a 2x2 mesh.

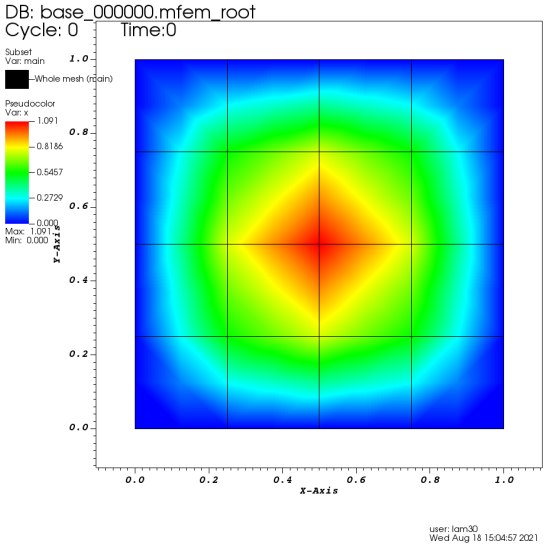

Figure B.14: The MMS solution for a 4x4 mesh.

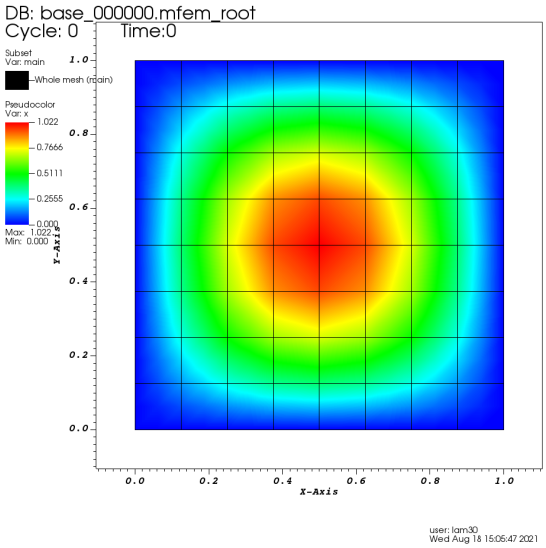

Figure B.15: The MMS solution for a 8x8 mesh.

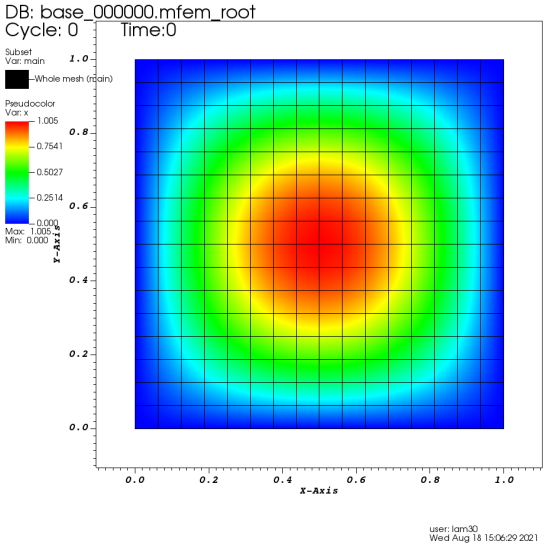

Figure B.16: The MMS solution for a 16x16 mesh.

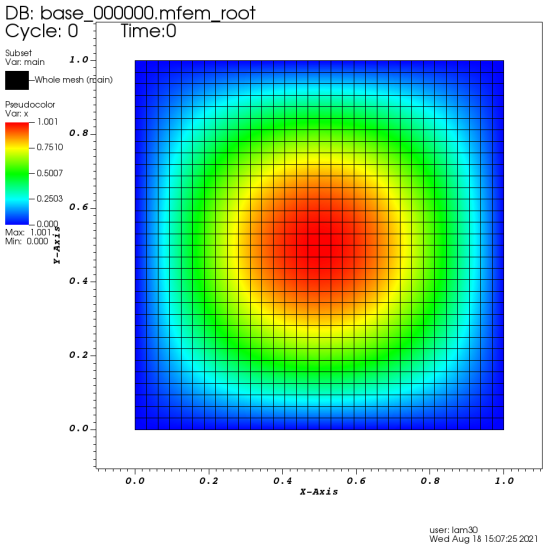

Figure B.17: The MMS solution for a 32x32 mesh.

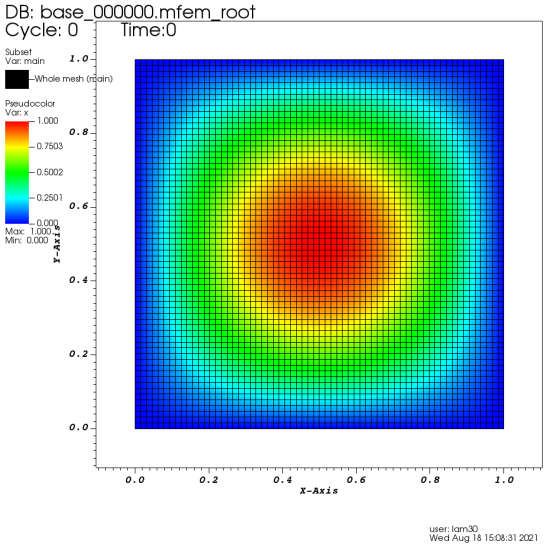

Figure B.18: The MMS solution for a 64x64 mesh.

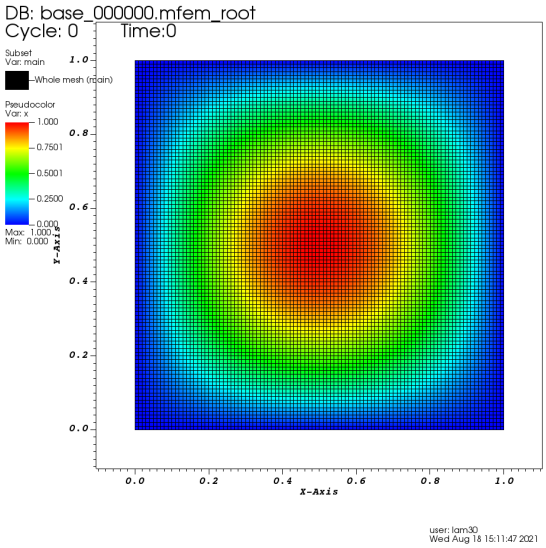

Figure B.19: The MMS solution for a 100x100 mesh.

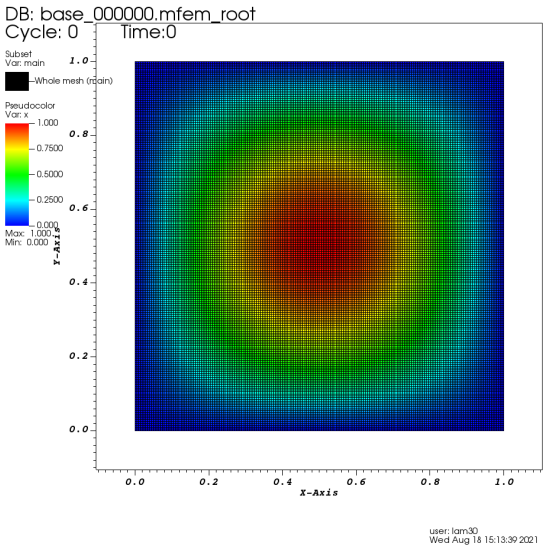

Figure B.20: The MMS solution for a 200x200 mesh.

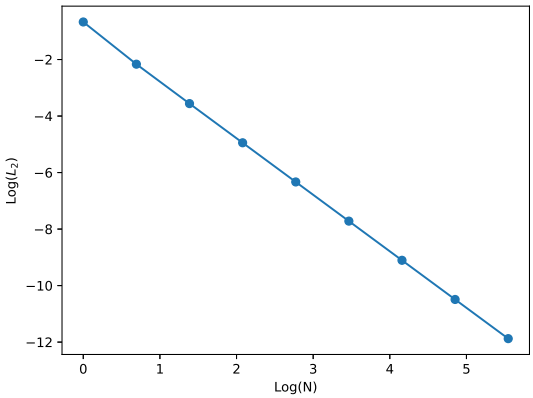

Figure B.21: The l_2 -norm of the error for the 2D MMS problem.

The l_2-norm of the error vs the mesh size are plotted below. Using the same formula as before, the slope of the plot is

$$m = -\frac{log(l_2(x_1)) - log(l_2(x_2))}{log(x_1) - log(x_2)} \approx 2.02 \tag{B.24}$$

The observed convergence behavior indicates the 2-d discretization of Eq. (B.16) has implemented correctly in MFEM.